AN EXPERIMENTAL STUDY OF SUPERCRITICAL CO_2 FLOW IN PIPES AND POROUS MICRO-MODELS FOR CARBON SEQUESTRATION APPLICATIONS

BY

FARZAN KAZEMIFAR

DISSERTATION

Submitted in partial fulfillment of the requirements
for the degree of Doctor of Philosophy in Mechanical Engineering
in the Graduate College of the
University of Illinois at Urbana-Champaign, 2014

Urbana, Illinois

Doctoral Committee:

Associate Professor Dimitrios C. Kyritsis, Chair
Professor Kenneth T. Christensen, Co-Director of Research
Assistant Professor Randy H. Ewoldt
Professor Albert J. Valocchi

Abstract

The flow of high-pressure, near-critical CO_2 in configurations relevant to CO_2 sequestration was investigated. The first configuration was CO_2 flow in pipes and orifices at pressures and temperatures close to the critical point of CO_2 (74 bar, 31°C). A 60-cm-long stainless steel pipe with 2.1 mm inner diameter was used in order to study near-critical CO_2 pipe flow. In terms of raw flow data, the results indicated high sensitivity of pressure drop to mass flow rate as well as to inlet conditions; i.e. pressure and temperature. Remarkably though, when friction factor and Reynolds number were defined in terms of the inlet conditions, it was established that the classical Moody chart described the flow with satisfactory accuracy. This was rationalized using shadowgraphs that visualized the process of transition from a supercritical state to a two-phase subcritical state. During this transition, the two phases were separated due to density mismatch and an interface was established that traveled in the direction of the flow. This interface separated the flow in two regions of essentially single-phase flow, which explained the effective validity of the classical Moody chart. Also, Joule-Thomson throttling was studied using a 0.36-mm-diameter orifice. For conditions relevant to carbon capture and sequestration, the fluid underwent Joule-Thompson cooling of approximately 0.5°C/bar. The temperature difference during the cooling increased with increasing inlet enthalpy. Discrepancies with previous computed and experimentally measured values of Joule-Thompson throttling were discussed in detail. In a second configuration, liquid/supercritical CO_2 was injected into two-dimensional porous micro-models saturated with water, which mimicked the process of injection and flow into saline aquifers. This flow configuration was studied using fluorescent microscopy and micro-PIV by seeding the water phase with fluorescent tracer particles, and dyeing CO_2 with a fluorescent dye. This technique allowed for

measurement of the velocity field in the water phase, and tracking the CO_2 phase in the porous medium. The results revealed the nature of the flow field during the initial invasion and migration of the CO_2 front. In particular, it was established that the front developed growing dendritic features called fingers. During that growth process, velocities 20–25 times the bulk velocity were measured, which occurred in both the flow direction and opposite to it. These velocity jumps support the notion of pressure bursts and Haines jump during pore drainage events. In addition, the variations of the interfacial curvature with time and their connection with water flow field during the growth of fingers were studied. The results revealed the existence of high-momentum pathways in water ahead of growing CO_2 fingers. After the passage of the CO_2 front, shear-induced flow was detected in the trapped water ganglia in the form of circulation zones near the CO_2-water interfaces. The shear from CO_2 flow also induced motion in the thin water films covering the surfaces of the micro-model.

Acknowledgements

The work presented here would not have come to fruition without the support of many people. First and foremost, I would like to express my deepest gratitude to my advisors, Dimitrios Kyritsis and Kenneth Christensen. Their optimism, enthusiasm, and patience gave me extra motivation for hard work and allowed me to remain hopeful even when the completion of this work seemed like a dream. My gratitude also goes to my doctoral committee members Randy Ewoldt and Albert Vaocchi for providing constructive feedback on my dissertation. Furthermore, I would like to thank Gianluca Blois and Julio Barros for sharing their invaluable experience in experimentation and PIV data processing.

I must also thank the people who helped me with the micro-fabrication in the cleanroom. Kyle Michelson patiently taught me the techniques and tricks that he had mastered over the years in the cleanroom. This made my micro-fabrication work much more productive and enjoyable. Glennys Mensing was always there for me to answer the questions that I had about the different fabrication processes. The MNMS cleanroom staff, particularly Miki Takagi, did a great job running the facility and troubleshooting the equipment, thus allowing me to finish this work without unexpected delays.

I also owe thanks to the members of the Combustion Physics Group, Anna Oldani, David Tse, Dino Mitsingas, Jihyung Kim, Mike Pennisi, Nick Traina, Rajavasanth Rajasegar, Tom Connelly, and the Laboratory of Turbulence and Complex Flow, Gianluca Blois, Julio Barros, Gokul Pathikonda, and Taehoon Kim. Thank you for making the lab and office a fun (and safe) place for work.

I also appreciate all of the support from my friends and family. I am lucky to have such wonderful people in my life. To Talisa, thank you for being a constant source of motivation in my life. To my aunt and uncle, Azam and Mohsen, thank you for being my second parents and supporting me through the difficult times.

Last but not least, I would like to express my gratitude to my parents whose sacrifices are the reason I am where I am. To my father, thank you for being such a great role model and an exemplar of perseverance. To my mother, thank you for your unconditional love and being such a positive influence in my life.

Table of Contents

List of Tables

List of Figures

1. Introduction

1.1 Motivation

The increased level of greenhouse gases (GHG) in the atmosphere has recently been a cause for concern due to their role in global warming and climate change. Among the greenhouse gases, CO_2 has received the greatest attention since it is the most abundant GHG (second to water vapor) and accounts for 77% of anthropogenic GHG emissions [1]. The rise in atmospheric CO_2 concentration in the past two centuries has been well documented from ice-core measurements for historic data and air-sampling measurements for more recent data [2], [3]. The global average CO_2 level in the atmosphere has reached 398.7 parts per million (ppm) in March 2014 [3] from about 280 ppm at the beginning of the industrial age in the mid-18th century [2], with an average rise rate of 2.0 ppm/year since 2000 [3]. In order to mitigate this rise rate and eventually stabilize and reduce the atmospheric CO_2 concentration, action must be taken to reduce CO_2 emissions. In 2004, Pacala and Socolow [4] proposed numerous strategies for reducing carbon emissions some of which have been widely implemented ever since. These strategies range from reducing CO_2 production (e.g. improved fuel efficiency for cars and power plants, and increased use of renewable energy sources such as wind, solar, biomass, etc.) to actively preventing produced CO_2 from entering the atmosphere through carbon capture and storage (CCS).

The CCS approach is an ideal candidate for CO_2 emission reduction in large stationary CO_2-emitting sources such as refineries, cement plants, and fossil fuel thermal power plants that have very high CO_2 production rates. This technique consists of two main phases: capture and sequestration. Capture refers to the sequence of processes by which CO_2 is separated from the flue gas stream, purified,

and compressed, while sequestration refers to sequestering of CO_2 either permanently or for geologically significant time periods (more than 10^5 years) [5]–[7] . Storage in porous geological media in general, and specifically in sedimentary basins, is the most viable option for long-term CO_2 sequestration [8]. Potential storage sites include depleted hydrocarbon reservoirs, coal beds, and deep saline aquifers. Saline aquifers are the most attractive based on high capacity, economics, minimum environmental impact, and availability of technologies required for undertaking the task [5], [9], [10]. Saline aquifers are porous formations saturated with liquid (water/brine; termed the resident fluid). An important stage in the CCS process is the injection of CO_2 into these formations during which CO_2 must displace the resident fluid. As explained in detail below, the solubility of CO_2 in water and water in CO_2 under typical deep reservoir pressure and temperature is on the order of 3% and 0.3% (mole basis), respectively. This solubility varies greatly with the chemical composition of the formation water and rocks. For instance, 30% total dissolved salt by weight can reduce solubility of CO_2 by 80% relative to pure water [11]. Once the solute concentration in each phase reaches the saturation level, the aqueous phase and the CO_2-rich phase can be treated as two immiscible fluid phases. We believe that dissolution processes do not affect the flow of either fluid phase through the permeable reservoir in a significant manner. Thus, from a fluid mechanics point of view, the underlying physics in this process is that of the flow of immiscible fluids in porous media, which will be one of the focus areas of this work. In particular, a deep understanding of these flow processes is essential for accurately predicting the migration of injected CO_2 within storage reservoirs. Such a predictive capability is necessary both for *a priori* viability assessment of potential storage sites and for *a posteriori* prediction of CO_2 migration in space and time once it is injected into the formation rock. Given the extreme range of spatial scales involved in this scenario (from km at the reservoir scale to μm at the pore scale), subgrid-scale modeling of pore-scale processes must be utilized in reservoir-scale predictions. Thus, the flow of CO_2 and water at the pore scale must be understood in order to develop accurate models of this physics.

Another important facet of the CCS process is the transport of CO_2 in pipelines from the place of capture to the disposal site that are not necessarily close to each other [5]. Typically, transport and storage processes take place at pressures and temperatures close to the critical point of CO_2 at approximately 74 bar and 31°C [12], [13]. Fluid flow in the vicinity of its critical point is of particular interest because of the increased sensitivity of thermophysical and transport properties to the changes in pressure and temperature. Even small fluctuations in pressure and temperature can affect the fluid properties, and hence the flow behavior. Thus, another focus area of this work is the flow of CO_2 in pipes near its critical point and the investigation of the effects of changes in fluid properties on flow behavior. The objectives of this thesis are:

- Address technological issues associated with the transport of CO_2 by studying the flow of CO_2 near its critical point in pipes. This requires investigating the effects of changes in fluid properties on flow behavior;
- Address fundamental problems related to CCS efficiency by investigating the dynamics of near-critical CO_2 flow through water-saturated porous media at the pore scale and the interaction between the two fluids at the interface experimentally using microscopic particle image velocimetry (Micro-PIV).

1.2 Problem physics

In the following sub-sections the physical properties of CO_2 as well as the characteristics of binary CO_2–water systems will be reviewed, in addition to the basic underlying physics of multi-phase flow in porous media and its relevance to CCS.

1.2.1 Physical properties of CO_2

First thermophysical properties of CO_2 are reviewed. These are presented in Fig. 1.1 using data that were obtained from the NIST Chemistry WebBook database [14]. In this database, a number of empirical relations developed specifically for CO_2 have been used for calculating various properties of CO_2 [15]–[18]. Several features that relate to fluid flow need to be highlighted. Near the critical point, few degrees change in temperature cause density and dynamic viscosity to transition from liquid-like large values to gas-like small values. Isobaric heat capacity increases by about two orders of magnitude and reaches a maximum near the critical point, while the kinematic viscosity reaches a minimum. The changes in viscosity may influence the flow in pipes and in porous geological formations [19].

1.2.2 Properties of CO_2–water binary system

1.2.2.1 Solubility

A property that is important in the context of sequestration of CO_2 in deep saline formations is the solubility of CO_2 in water and vice versa under reservoir conditions. The solubility is a function of pressure, temperature, and chemistry of the formation water (i.e. salinity). Figure 1.2 presents representative pressure vs. composition diagrams for CO_2–water system at constant subcritical and supercritical temperatures in panels (a) and (b), respectively. Solubility of CO_2 in pure water at constant temperature increases sharply with pressure until it levels at approximately 2.7% by mole (~6.5% by mass) beyond 7 MPa. On the other hand, solubility of water in liquid/supercritical CO_2 for the range of pressures and temperatures studied in this work, is approximately one order of magnitude less than solubility of CO_2 in water, and it is 0.3–0.4% by mole (~0.15% by mass). The effect of temperature on mutual solubilities of water with liquid/supercritical CO_2 is opposite to each other. Increased temperature reduces solubility of CO_2 in water while it increases the water content of the CO_2-rich phase.

Also, the solubility decreases with increased salinity of water [5], [11], [20]. Enick & Klara [11] reported an 80% reduction in solubility of CO_2 in brine with 30% by weight total dissolved solids relative to pure water, over pressure and temperature range of 3–85 MPa and 298–523 K. It is worth noting that despite the seemingly low solubility of CO_2 in water, dissolution of CO_2 in water is a major trapping mechanism for geological sequestration of CO_2 in deep saline formations [21]. This process will be discussed in more detail in section 1.3.

In addition to the overall solubility, the kinetics of the dissolution process is of importance as well. There are few studies in the literature with relevant kinetics data for the dissolution process of CO_2 in water. Fujioka et al. [22] measured the shrinkage rate of single CO_2 droplets, with an initial diameter of larger than 10 mm, in water at 3°C temperature and 28 MPa and 35 MPa pressure. Their results indicate a diameter reduction of rate 0.5 μm/s over 5-6 hours. Shindo et al. [23] used the data reported in [22] to model the kinetics of the dissolution process; however, their findings are not readily applicable to the problem being studied here. That is because at pressures greater than 4.45 MPa and temperatures lower than 10.2°C, hydrate films form at the two-fluid interface [22], [24] which does not take place under typical reservoir conditions. Despite the lack of data on the process kinetics, scaling analysis has shown that the dissolution process is transport–and not kinetically–limited [25].

1.2.2.2 **Interfacial tension (IFT)**

Security and efficiency of CO_2 storage in deep saline aquifers is greatly influenced by the fluid-fluid and fluid-rock interfacial interactions where interfacial tension (IFT) plays a crucial role [26]. The interfacial tension is a function of pressure, temperature and salinity of the formation water and has been measured over a wide range of these parameters using the pendant (or rising) drop method [26], [27]. Figure 1.3 presents IFT data in a CO_2–pure water system measured by Bachu & Bennion [27]. It is observed that for subcritical temperatures, IFT does not vary with temperature at constant pressure.

However for CO_2 supercritical temperatures it increases with temperature at constant pressure. Also, at each temperature, IFT decreases sharply with pressure up to ~10 MPa beyond which it plateaus to a constant value. Increased salinity at constant pressure and temperature, for both sub- and supercritical temperatures, results in increased interfacial tension [26].

The significance of interfacial tension in multi-phase immiscible flows lies in its effect on capillary pressure. In pore network models, capillary pressure based on throat diameter is the pressure threshold that dictates whether the non-wetting fluid can enter the pore or not. Based on the Young-Laplace equation [28]:

$$P_c = 2\gamma K \tag{1.1}$$

In this equation, P_c is the capillary pressure, γ is the interfacial tension, and K is mean curvature of the interface.

1.3 Relevance to CCS applications

In this section, the most relevant topics encountered in CCS applications are reviewed. First, the basic models for multi-phase immiscible flow in porous media are addressed. Next, trapping mechanisms relevant to geological CO_2 sequestration are reviewed. Finally, the physics of immiscible multi-phase flow in porous media is reviewed.

1.3.1 Basic approaches to multi-phase flow modeling in porous media

Flow in geological porous media is typically treated using Darcy's law. For a single-phase flow:

$$q = -\frac{\kappa A}{\mu}\nabla p \tag{1.2}$$

In this equation, q is the volumetric flow rate, A is cross-sectional area, κ is permeability (also referred to as absolute or intrinsic permeability) of the porous medium, μ is fluid viscosity, and p is pressure. The quantity q/A has the units of velocity and is referred to as Darcy velocity.

In multi-phase flow, the relative permeability for each fluid is used. For fluid component i:

$$q_i = -\frac{\kappa_i A}{\mu_i}\nabla p \tag{1.3}$$

In this equation, κ_i is effective permeability of the i^{th} component. Relative permeability of the i^{th} component, $\kappa_{r,i}$, is defined as the ratio of its effective permeability to the absolute permeability of the medium:

$$\kappa_{r,i} = \frac{\kappa_i}{\kappa} \tag{1.4}$$

Relative permeability is found to be a path-dependent property and shows hysteresis, in the sense that it is different for drainage and imbibition processes central to geological CO_2 sequestration. In other words, the relative permeability will generally depend on whether the porous medium is initially saturated by the wetting phase (drainage) or the non-wetting phase (imbibition). For a rock sample, for example, relative permeability of each fluid component is expressed as a function of saturation and process (drainage or imbibition). Figure 1.4 presents a sample relative permeability vs. saturation curve from Bennion & Bachu [29] data obtained for sandstone core samples from the Cardium Formation.

Another measurement performed on rock samples for characterization purposes is the capillary pressure. Capillary pressure is inherently a pore-scale phenomenon and is a function of interfacial tension (surface tension) and interfacial curvature at the two-fluid interface (Eq. 1.1). However, in reservoir engineering terminology, capillary pressure is instead thought of, defined and measured differently. In this context, the capillary pressure is a macro-scale (as opposed to pore/micro-scale) quantity and for a given representative elementary volume is defined as:

$$P^{nw} - P^{w} = P^{c}(S^{w}) \tag{1.5}$$

In this equation P is pressure and S is saturation, with the superscripts c, w, and nw denoting capillary, wetting and non-wetting, respectively and $P^c(S^w)$ is given by an empirical correlation obtained as a step in characterizing reservoir rocks. Figure 1.5 presents a sample capillary pressure vs. saturation curve from the data presented in Bennion & Bachu [29]. Despite the simplistic approach towards capillary pressure measurement, for the data presented in this figure, it is observed that, in accordance with Eq. 1.1, capillary pressure increases as the interfacial tension increases.

Empirical relations such as those shown in Figs. 1.4 and 1.5 form the basis for modeling these flows at the scale of a sequestration reservoir wherein pore-scale processes are not resolved. In the simplified models of propagation, P^w and P^{nw} are both assumed hydrostatic and their difference gives the capillary pressure. Using this value of capillary pressure, the local saturation can be obtained using the empirical capillary pressure vs. saturation relationship for the given type of porous medium (Fig. 1.5, for example). Knowing the local saturation, the relative permeability of each phase can be determined from empirical data relating relative permeability to saturation (Fig. 1.4). Propagation of the phases is then determined from Darcy's law using the relative permeability values obtained in the previous step [30]. In this approach, it is assumed that capillary pressure is only a function of saturation, thus lumping all pore-scale effects (contact angle, rock properties, geometry, etc.) into S^w. As a result of this over-simplification of the problem physics, multiple values are obtained for P^c [28]. In fact, the hysteretic effect in relative permeability vs. saturation curves mentioned earlier also stems from this over-simplification. It has been proposed that in order to remove the hysteretic effects, variables such as specific interfacial area, contact angle (wetting properties), and dynamic effects must be included in the P^c function [28], [31]–[33].

1.3.2 Trapping mechanisms

Under typical geologic storage conditions in saline aquifers, CO_2 is lighter than the resident fluid and will rise due to buoyancy forces. Secure storage of CO_2 necessitates a trap that can ensure safe and

effective storage of CO_2 for extended time periods and prevent it from leaking to the surface and the atmosphere. The ideal storage site should incorporate closed stratigraphic or structural traps that are the most secure form of traps. Hydrocarbons have been safely stored in reservoirs with such structural traps for millions of years. Thus, they are natural candidates as storage sites for geological sequestration of CO_2. However, the hydrocarbon reservoirs must be depleted in order to be available for CO_2 storage, and this significantly limits the total number and capacity of potential storage sites for CO_2 [21], [34]. It is worth noting that CO_2 injection into mature –not depleted– hydrocarbon reservoirs for enhanced oil recovery can be considered as a storage option; however the residence time of CO_2 in this situation is relatively small (months to several years) because a significant part of injected CO_2 will leave the reservoir along with the produced hydrocarbon [5]. Furthermore, while stratigraphic features and structural traps at the reservoir scale can immobilize vertical migration of CO_2, migration of the CO_2 in directions normal to gravity must be countered by other mechanisms for trapping it in the formation rock. Eventual permanent storage of CO_2 may occur through mineral trapping where the injected CO_2 precipitates as carbonate minerals. However since this process may take over thousands of years to complete, other trapping mechanisms must be in place to prevent CO_2 migration during this time. These mechanisms are physical and/or chemical processes, typically at the pore scale, that result in immobilization of CO_2 in a geological formation and thus guarantee its safe storage for extended periods of time [21], [34]. These mechanisms can be categorized into primary and secondary, which are governed by drastically different time scales. Primary mechanisms are those that trap CO_2 during the injection period (typically 30–50 years). Structural and stratigraphic traps, and hydrodynamic trapping are examples of primary mechanisms. On the other hand, secondary mechanisms are those that take effect over time (hundreds to thousands of years) in a gradual manner and increase the security of the storage after injection has stopped. The main secondary mechanisms are: residual trapping, solubility trapping, and mineral trapping. The four main mechanisms relevant to CO_2 sequestration in saline aquifers are

explained below. The numbers given in parentheses in front of each mechanism indicates the operating timeframe of that mechanism adopted from IPCC 2005 report [35].

i. Hydrodynamic trapping (30–50 years)

Hydrodynamic trapping stems from the extremely low flow rates of the resident fluid of the aquifer and the resulting geologically significant residence times for the injected CO_2 [21]. Bachu et al. [34] studied the deep saline aquifers in the Alberta basin in Canada. They showed that although deep aquifers are open-structure (i.e. they do not incorporate any closed stratigraphic trap) they could be safely used for CO_2 storage. That is because the estimated velocity of formation waters in the aquifer is on the order of 1–10 cm/year, and this low velocity combined with the extent of the aquifer, means the injected CO_2 will have a residence time on the order of 1 million years in the aquifer before it can reach the surface. The operating time frame of this mechanism is the same as the injection period, meaning that during the injection phase, CO_2 is confined within the aquifer by this mechanism, before other mechanisms have started operating [10], [34], [36].

ii. Residual (capillary) trapping (~10^2 years)

Residual trapping is a mechanism by which disconnected bubbles of CO_2 are immobilized within the pore spaces by the interfacial tension (capillary forces) between CO_2 and formation water. These bubbles are left in the wake of a stream/plume of CO_2 when formation water invades the pore space after being initially displaced by the injected/migrating CO_2 [36]. Residual trapping occurs almost entirely after the injection has stopped [36], [37].

The importance of this trapping mechanism lies in the fact that solubility and mineral trapping are slow processes relative to residual trapping. Dissolution of water in CO_2 is thought to be rate-limited by the diffusion of the dissolved CO_2 away from the two-fluid interface [21]. Once injected CO_2 has dissolved in the formation water, mineral trapping would *at least* require time on the order of tens to

hundreds of years [10]. In the absence of hydrodynamic trapping, dissolution and mineral trapping time scales may be too large relative to the time scales associated with CO_2 plumes migration rates. This may allow for the migration of CO_2 with potential leakage risk. However, amid the slow progress of solubility and mineral trapping, capillary trapping immobilizes small disconnected bubbles of CO_2, thus minimizing the risk of potential leaks while the slow geochemical reactions are taking place. In addition, distribution of CO_2 in a large number of disconnected bubbles (as opposed to few large blobs) results in high overall surface area to volume ratio that can enhance the transport and dissolution processes between the two phases [38]–[40].

Another instance where capillary trapping is dominant is in the case of exsolution of CO_2 from formation water during depressurization, which can be caused by fracture or upward movement of CO_2-saturated fluids through faults or leaking boreholes. In this scenario, capillary forces immobilize the exsolved CO_2 bubbles. These bubbles also significantly reduce the mobility of both the aqueous phase and the CO_2-rich phase thus creating a barrier to flow and further decreasing the risk of leakage [38].

iii. Solubility trapping (10^2–10^3 years)

Dissolution of CO_2 in formation water takes place by the following chemical reactions [21][36]:

$$\mathrm{CO_{2(gaseous)}} \rightarrow \mathrm{CO_{2(aqueous)}} \quad 1.6$$

$$\mathrm{CO_{2(aqueous)}} + \mathrm{H_2O} \rightarrow \mathrm{H_2CO_{3(aqueous)}} \quad 1.7$$

The above reactions result in an aqueous phase that is heavier than the resident fluid and will thus tend to subside towards the bottom of the formation by gravity [41]. Also, formation of weakly acidic $\mathrm{H_2CO_{3(aq)}}$ is a precursor to the geochemical reactions for the mineral trapping mechanism discussed below. Recall that solubility of CO_2 in pure water increases sharply with pressure until it levels at approximately 2% molar (~5% by mass) beyond 7 MPa. On the other hand, it decreases with increasing temperature under constant pressure and with increasing salinity for given conditions of pressure and

temperature [5], [11]. Numerical simulations indicate that, depending on reservoir conditions (salinity, temperature, depth, etc.), 20–60 kgCO_2 can dissolve in 1 m^3 of formation fluid [42], [43]. The time-scale however depends on flow rate of water in the aquifer and is predicted to be on the order of centuries [44], [45].

iv. Mineral trapping (>10^4 years)

Eventual permanent storage of CO_2 may occur through mineral trapping where the injected CO_2 precipitates as carbonate minerals. This is the slowest yet most secure trapping mechanism. Through this mechanism, over thousands of years, up to 90% of the injected CO_2 can be trapped by reactions with the basic minerals in the aquifer [10]. The chemistry of the formation rocks and the formation water, in terms of mineral compounds and ions, as well as the composition of the injected gas (potential impurities), are controlling factors and can affect the reservoir's potential for storing CO_2 through geochemical reactions [21], [34]. For example, high salinity reduces the solubility of CO_2 in water [11], while the chemistry of the formation water and the rocks may increase or decrease the storage potential of the aquifer. The presence of mineral ions such as calcium and magnesium, in water or in the rocks, can enhance the mineral trapping of CO_2 through precipitation of carbonate minerals [34]. In terms of reaction rates, the reaction of dissolved CO_2 with carbonate minerals is much faster than its reaction with silicate minerals (days vs. hundreds of years) [10], [21]. Regardless of the chemistry, the residence time on the order of 10^6 years associated with hydrodynamic trapping can enhance the potential for mineral trapping by providing the times needed for completion of the slow geochemical reactions [10], [34].

1.3.3 Physics of multi-phase fluid flow in porous media

As stated earlier, saline aquifers are considered as one of the most promising options for geological sequestration of CO_2. The relevant physical flow phenomenon in this application is the flow of

immiscible fluids (liquid/supercritical CO_2 and formation water) in porous media. Thus, the flow characteristics and the underlying physics at the pore scale must be deciphered in order to understand reservoir-scale storage phenomena.

The competition between viscous and capillary forces typically determines the stability of the travelling interface and the displacement mechanism at the pore scale. The governing dimensionless parameters in such systems are the capillary number (Ca) and viscosity ratio (M), defined as:

$$\mathrm{Ca} = \frac{\mu_2 V_2}{\gamma \cos\theta} \tag{1.8}$$

$$\mathrm{M} = \frac{\mu_2}{\mu_1} \tag{1.9}$$

In these equations, μ is the dynamic viscosity, V is the bulk velocity, γ is the interfacial tension between the two fluids, and θ is the contact angle between the two fluids and the surface. The indices 1 and 2 refer to the resident phase and the advancing phase, respectively.

Three distinct displacement regimes for multi-phase flow in porous media have been identified: stable displacement, viscous fingering, and capillary fingering. Flow conditions under which each of these regimes prevail can be presented in log M – log Ca diagrams, such as the one shown in Fig. 1.6. In the stable displacement regime, the dominant force is due to the viscosity of the invading fluid and the moving fluid-fluid interface is flat with some irregularities at the scale of a few pores. In the viscous fingering regime, the controlling quantity is the viscosity of the displaced fluid. In this regime, the interface between the two liquids develops instabilities in the form of dendritic fingers that grow mostly in the direction of the flow and towards the exit (Fig. 1.7, panels (a) and (b)). Lastly, in the capillary fingering regime, the capillary forces (at the interface) are dominant. Under such conditions, instability occurs again but, unlike that of viscous fingering, capillary fingers grow in all directions, even backwards, at all scales (Fig. 1.7, panels (c) and (d)). Clearly, the final degree of saturation of the formation by the advancing fluid is smaller for viscous fingering than for capillary fingering [46].

Due to the small viscosity ratio of CO_2 and water ($\mu_{CO_2}/\mu_{water} \approx 10^{-2}$) for the conditions relevant to CO_2 injection into deep saline aquifers, the displacement front (interface) will be unstable. For small *Ca*, the dominant regime will be capillary fingering, and for large *Ca* it will be viscous fingering. Also, over some intermediate range of *Ca*, crossover occurs, where both fingering modes exist simultaneously in different parts of the domain [47]. Thus, the final degree of saturation in geological CO2 sequestration will be highly dependent upon the local thermodynamic conditions in the formation rock.

The seemingly smooth and continuous displacement of the fluid-fluid interface from macroscopic observations is in fact the product of numerous pore-scale interfacial jumps accompanied by pressure bursts [48]. Interfacial velocity measurement in a mono-layer sintered glass bead homogeneous micro-model using high-speed imaging at 1200 frames per second by Moebius & Or [48] has indicated instantaneous interfacial velocities up to 50 times the mean front velocity. The Reynolds number defined based on interfacial velocity, pore diameter, and kinematic viscosity of the wetting phase, ranged from 400 to over 1000. This Reynolds number greatly exceeds the upper limit of validity for assuming that the flow behaves in the Darcy regime and is governed by Eq. 1.2, which is approximately 10 [49]. Armstrong & Berg [50] reported interfacial velocities three orders of magnitude greater than the bulk velocity during drainage. These velocity jumps are known in the literature as Haines jumps, first documented by William Haines [51] in 1930. Such phenomena can have important implications in the flow regime where viscous, capillary, and gravitational forces are considered to be dominant, and inertial forces are neglected. While it is typically presumed that the infiltration of CO_2 into the formation rock is governed by the viscosity ratio and Capillary number (reflective of a relative balance between viscous and capillary forces, with inertial forces neglected), it is conceivable that during these jumps the inertial effects may no longer be negligible relative to viscous and capillary forces [50]. This possible role of inertial effects in CO_2 migration through porous media is a hypothesis that will be examined in this thesis.

1.4 Review of state of the art

In the following sections, a review of the state of the art of the fluid dynamics in configurations relevant to CCS applications is presented. The first section addresses the flow of CO_2 near its critical point in pipes. This configuration is relevant to the process of CO_2 transport from the source to the sequestration site. For the flow and pressure drop in valves, the throttling process through orifices is reviewed. The second section discusses the state of the art in the experimental methods used to investigate immiscible multi-phase flow in porous media.

1.4.1 Pipe flow

Studying of two-phase CO_2 flow has gained increased attention in the past two decades due to the increased popularity of CO_2 as a refrigerant [52], [53]. Heat transfer and flow of supercritical CO_2 in pipes and channels have been studied in transcritical refrigeration cycle applications where heat rejection takes place at a supercritical state [54], [55]. Similar studies have also been performed in the context of nuclear reactor cooling systems [56]–[58]. In these studies, the main focus was the determination of the heat transfer coefficient. However, an investigation of the underlying flow fundamentals is still missing.

Flow and heat transfer in supercritical and near-critical fluids have been studied analytically and computationally [59]–[61]. One key obstacle is that the critical point is a singular point where surface tension and effective mass diffusivity go to zero, and isobaric heat capacity and isentropic compressibility become infinite. As a result, the integral conservation equations may not necessarily be convertible to a differential form. The result is that the validity of the Navier–Stokes equations becomes questionable as the critical point is approached. Thus, any model for the near-critical regime must be examined to ensure there are no inconsistencies [62].

In terms of flow visualization, the only relevant previous works were conducted by Pettersen [63] and Yun et al. [64]. Pettersen studied two-phase flow patterns of CO_2 during vaporization in a horizontal glass tube at 0°C and 20°C (corresponding saturation pressure: 3.5 MPa and 5.7 MPa). Yun et al. studied the flow boiling of CO_2 in a horizontal narrow rectangular channel at 4.0 MPa (corresponding saturation temperature: 5.3°C). These pressures and temperatures are relevant to the evaporation process in air-conditioning systems. In both studies, high-speed visualization was employed to study the distribution of the two phases in the flow. Distinct flow regimes were identified and flow pattern maps were created based on quality (vapor mass fraction) and mass flux. The thermodynamic state of the fluid in these studies was relatively far from the critical point and thus may not represent the behavior of the flow of a "near-critical" fluid.

In this thesis, pipe-flow of CO_2 very close to its critical point (74-80 bar, ~20-40°C) has been studied. Knowledge on such flow conditions is currently lacking from the literature. The experiments include pressure drop per pipe unit length as a function of mass flow rate at various pressures and temperatures, as well as shadowgraph visualizations.

1.4.2 Multi-phase flow in porous media

As stated earlier, saline aquifers are considered as one of the most promising options for geological sequestration of CO_2. Thus, several studies have focused on injection of liquid/supercritical CO_2 into water/brine-saturated porous media and evaluation of the processes relevant to migration of CO_2 throughout the porous structure. In this section, the state of the art in experimental methods used to investigate immiscible multi-phase flow in porous media at the pore scale are reviewed, with particular focus on visualization techniques. Based on the type of porous media employed, the experimental work can be divided into three subcategories: studies on two-dimensional porous micro-models ([38], [47], [65],

[66]), three-dimensional glass bead columns ([28], [31], [67], [68]), and actual core samples of rock ([39], [40], [68]).

Two-dimensional micro-models can be designed and fabricated with any geometry (homogeneous or heterogeneous) and have the advantage of being optically accessible and thus allowing application of traditional visualization techniques and optical diagnostics (e.g. PIV). However, they do not fully reproduce the 3D nature of the original problem. Glass bead models are 3D and thus more accurately mimic the flow physics of natural sedimentary rocks. They can be fabricated with different sized beads to obtain desired geometry and pore size distribution. In general, despite the clarity of the solid phase and the working fluid, optical access to the pore spaces is limited due to the light refraction at the fluid-solid interface caused by refractive index mismatch. In order to use optical measurement techniques, the beads must be rendered optically transparent. This can be achieved by matching the refractive indices of the fluid and the solid phase, using an approach known as refractive index matching (RIM) [69]. However, the RIM technique can only be applied to experiments at atmospheric pressure, with proxy fluids, because RIM can only be achieved with a small subset of fluid pairs (not CO_2 and water). Also, high-pressure experiments require placing the glass bead model in a core holder which blocks optical access. In that case, the applicable visualization method is same as the one used for rock samples, which is discussed next.

The methods mentioned above involve using idealized geometries (2D micro-models and glass bead columns) as proxy for natural porous media. Such approaches allow experiments to be performed in media with controlled geometry, pore-size distribution, optical access, etc. However, in order to validate the findings obtained through such physical models, experimentation on core samples from actual reservoir rock is required. Visualization in these opaque solid structures can only be achieved using X-ray CT scanning ([39], [40], [68], [70], [71]) or magnetic resonance imaging (MRI) ([72], [73]). The process

and techniques for X-ray tomographic imaging for studying pore-scale phenomena in subsurface porous media is described in depth in Wildenschild & Sheppard [70] and Brown et al. [71].

In any of these settings, the experiments can be conducted using water/brine and liquid/supercritical CO_2 at reservoir pressures and temperatures (80+ bar, 30+°C) or proxy fluids at atmospheric pressure and room temperature. The use of proxy fluids can significantly reduce the complexity of the experimental setup; however, the controlling parameters (e.g. viscosity ratio, interfacial tension, contact angle, etc.) may no longer be representative of real conditions. In this thesis, an experimental setup and methodology are developed to study the multi-phase flow of liquid/supercritical CO_2 in porous micro-models using the micro-PIV technique.

In micro-model experiments with liquid/supercritical CO_2, fluorescent microscopy is used for visualization. Typically one of the two phases is tagged with a fluorescent dye and imaged with a camera. Zhang et al. [65] used coumarin 153 to visualize the liquid CO_2 phase. They studied displacement of water by liquid CO_2 in a 2D porous micro-model at thermodynamic conditions of 90 bar and 22°C. They stitched 48 (8×6) images obtained at 1.6 μm resolution and acquired at different times together to get an image of the entire porous section. They started recording images after CO_2 had reached the outlet of the micro-model, though they did not report the time duration that it took to image the entire porous section. Doing so is questionable because the distribution of the fluid phases may change during the cumulative imaging time to achieve the full tiled image. Thus, their stitched image may not represent a real snapshot in time of the flow field. This is especially important for the reported specific interfacial length that can change even when the overall saturation is constant. Armstrong et al. [28] reported rearrangement of the phases and their interfaces even 10-15 minutes after the pump was turned off. Furthermore, images of the fluorescence only demarcated the presence of CO_2 in the pore space, but it did not allow for identification of CO_2 flowing through the porous micro-model. Thus, regions of trapped CO_2 versus regions of continuously flowing CO_2 could not be distinguished from one-another.

Wang et al. [66] performed experiments similar to Zhang et al. [65] at 90 bar, 41°C. They were able to capture the crossover between capillary fingering and viscous fingering. The observed flow regimes in these two studies were in agreement with the phase diagrams previously reported in [47]. Unlike the procedure used in [65], they began imaging after quasi-steady state saturations were reached, meaning that the saturation of CO_2 did not change with increased injection volume. However, while the macroscopic saturation may be constant, no mention was made as to any changes observed in the spatial distribution and topology of the fluid phases and their interfaces, which can significantly alter the microscopic state of the system.

Armstrong et al. [28] used a 25.0 mm long column with 7.0 mm inside diameter packed with soda-lime glass beads (35% 0.6 mm diameter, 35% 0.8 mm diameter, and 30% 1.0–1.4 mm diameter) as their porous medium. They used water and oil as the wetting and non-wetting phases, respectively. They employed X-ray computed micro-tomography (CMT) with 13 μm/pixel resolution to study phase saturation, interfacial curvature, and geometrical configurations of the phases as being connected/disconnected. Connected and disconnected configurations can be loosely translated as occupying multiple pores vs. a single pore. They analyzed CMT images to extract the interfacial curvature, averaged them over the representative elementary volume, only including the interface of the connected fluid interfaces, and then applied Eq. 1.1 to deduce a "curvature-based" capillary pressure. They compared this value with the external pressure difference across the sample measured by a pressure transducer which they refer to as "transducer-based" capillary pressure. Their experimental procedure consisted of injection/withdrawal of a set volume of fluid, shutting off the pump and allowing the fluids to equilibrate for 10-15 minutes (or more if necessary) until no fluid movement was observed in the CMT images. They reported generally good agreement between the two capillary pressures with 10% deviation for imbibition and 20% deviation for drainage when equilibrium was reached. However, the deviation was much more significant at 50% when equilibrium was not reached. This is a clear indication that the

traditional approach of using empirical relations (as mentioned in section 1.3.1) for saturation-relative permeability, and saturation-capillary pressure (Eq. 1.5) is not applicable under dynamic/transient conditions. In fact, it is now accepted that the rate of change of saturation must be accommodated in the –macroscopic– capillary pressure function [28], [74]–[77]. These observations point to the fact that it is necessary to study the transient flow phenomena in order to understand the controlling variables of the capillary pressure function. However, there are very few studies addressing the dynamic/transient flow phenomena in these systems and one of the objectives of this thesis is to address those areas.

In two studies focused on the effect of depressurization, Zuo et al. studied exsolution of CO_2 from carbonated water in porous micro-models [38] and rock samples [40]. The exsolution occurs due to reduced solubility of CO_2 in water by decreasing pressure. In practical CO_2 storage, this can happen by leakage of CO_2-saturated water/brine through faults or leaking boreholes. In these experiments, an important parameter is the critical gas saturation, which is defined as the minimum gas saturation at which the gaseous phase becomes mobile. The mobilization can be interpreted in two different ways. One interpretation is the onset of gas production in a reservoir, which is a convenient criterion in reservoir scale studies [78]. The second interpretation is the formation of a sample-spanning cluster of the gaseous phase [79], [80].

In rock sample experiments [40], Zuo et al. used Berea sandstone samples with high permeability (266–1066 mD) and Mount Simon samples with low permeability (15.7 mD). The system was initially filled with CO_2-saturated water and then depressurized from 12.41 MPa to 2.76 MPa at a constant temperature of 50°C with two different depressurization rates. The rapid and the slow depressurization rates were ~1 MPa/min and ~20 kPa/min (1.2 MPa/hr), respectively. They employed X-ray CT scanning, taking images with 490 μm/pixel resolution and at a minimum interval of 1 mm along the sample axis. They observed that distribution of the exsolved CO_2 was uniform in homogeneous rock samples. Moreover, after exsolution, the mobility of both phases was reduced significantly, evidenced by the small

relative permeabilities ($\kappa_{r,water} < 0.1$, $\kappa_{r,CO2} \simeq 10^{-4}$). This was attributed to the high interfacial tension between the water and CO_2 phases, dispersed as small disconnected bubbles in the samples. It is worth noting that despite the sharp difference in densities of the two phases (at 2.76 MPa, 50°C: 1000 kg/m^3 for water and 51 kg/m^3 for CO_2), the results indicated minor gravity-induced redistribution of the phases, which is an indication of strong capillary trapping.

In micro-model experiments [38], the porous section of the 2D micro-model was designed based on micrographs taken from a sandstone core, thus representing the geometry of real porous media in two dimensions. Water was dyed with fluorescein in order to allow visualization of the aqueous phase and was imaged at a resolution of 1.6 μm/pixel with fluorescent microscopy. The system was depressurized at a constant temperature of 45°C, from 9 MPa to 1.8 MPa, at 1 MPa/hr rate. The first CO_2 bubbles were observed at 3.1 MPa which indicates large oversaturation of water before nucleation of the CO_2-rich phase begins. As the pressure was gradually reduced, the number of bubbles increased while their size remained unchanged. The distribution of the exsolved gaseous phase was highly correlated with the pore size distribution of the rock sample, which signifies strong capillary trapping. They recorded critical saturation values that could not be explained with neither interpretations of critical gas saturation. Based on their observation, they concluded that mobilization of the exsolved gas occurs through bubble expansion, consequent snap-off caused by capillary instability, and merging with other bubbles. This conclusion further supports the significance of the pore-scale phenomena in controlling the macro-scale behavior of the system and the necessity of studying the flow systems at the pore level.

Perrin and Benson [39] used cylindrical rock samples, and injected a mixture of CO_2 and brine at 63°C and 12.4 MPa for one case and at 12.4 MPa and 50°C for the other. Prior to data collection, the system was run for a day in order to reach steady state and ensure equilibrium between the two fluid phases. As a result, each of the two phases was at saturation concentration for the pressure and temperature of the experiment. They used X-ray CT scanning with 254 μm/pixel image resolution and

1 mm or 3 mm slice thickness along the sample axis to determine the relative permeability and 3D saturation distribution of CO_2 and brine inside the rock sample. They studied the effect of sub-core scale heterogeneities on the spatial distribution of CO_2. Their results showed that CO_2 saturation correlated with porosity in the sense that CO_2 saturation was higher in high-porosity regions and it was lower in low-porosity regions. In some instances, especially when the low porosity/permeability region is parallel to the flow direction, that region can be bypassed by CO_2 altogether. They concluded that small-scale heterogeneities can significantly affect the flow – of both phases – in the porous media. This result further substantiates the claim that the flow in the macro-scale is influenced by the geometrical features and flow phenomena at the pore scale.

Among the experimental work reviewed here, only a few of them have addressed the interface displacement and the phenomena occurring in the transient state of the flow, and the effects of transient flow (front migration) have been mostly neglected. The major works addressing such phenomena are those by Armstrong & Berg [50] and Moebius & Or [48] that were mentioned briefly in section 1.3.3 and are revisited here. Armstrong & Berg [50] measured interfacial velocities in micro-models with 60 μm pore diameters, with water and decane as the wetting and non-wetting fluids, respectively, over the capillary number range of 3.4×10^{-6} – 3.4×10^{-4}. They used high-speed imaging at 2000 fps and investigated the interfacial displacement velocities and the pore drainage dynamics. Moebius & Or [48] used water and air as the wetting and non-wetting phases, respectively, and imaged the flow at 1200 fps in a glass bead model with ~2 mm pore diameter. A major difference between Armstrong & Berg [50] and Moebius & Or [48] lies in the pore sizes of the porous media (60 μm vs. 2 mm). The difference manifests itself in dominance of capillary forces in the former and inertial forces in the latter. As a result, Armstrong & Berg [50] reported interfacial velocity independent from changes in the bulk flow rate, while Moebius & Or [48] observed that the peak velocity was directly correlated with the bulk flow rate.

Armstrong & Berg [50] reported maximum interfacial velocity up to 3 orders of magnitude greater than the mean pore velocity (calculated from bulk flow rate). Notably, the Reynolds number (defined based on interfacial velocity, pore diameter, and kinematic viscosity of the wetting phase) associated with the peak velocity is still less than 1 which indicates dominance of viscous forces over inertial forces. Moebius & Or [48] reported interfacial velocity jumps up to 50 times the mean front velocity, with associated local Reynolds number ranging from 400 to over 1000 which lies within the turbulent flow range [49] . However, it must be noted that the large Reynolds number is in part due to the large pore diameter. Even without considering the velocity jumps, the Reynolds number based on average interface displacement velocity falls in the range of 8–64, which exceeds the upper limit of validity of Darcy's law and falls within the range of transition to turbulence. Thus, the flow is mostly dominated by inertial and viscous forces, and as suggested by Armstrong & Berg [50] that is the reason for the dependence of interfacial velocity jump on bulk flow rate.

Based on the analysis of pore drainage dynamics, Armstrong & Berg [50] concluded that the drainage dynamics is a cooperative and non-local process in the sense that it affects the fluid in adjacent pores and throats. This process is controlled by capillary-viscous-inertial effects. Moreover, their results illustrate that the pore-scale phenomena do influence the macro-scale behavior of the system and thus need to be studied in more depth.

Given the observations outlined above and the state of the art in immiscible multi-phase flow in porous media, the current effort investigates the *transient* flow phenomena and interfacial displacement at the *pore scale*, in multi-phase flow of liquid/supercritical CO_2 and water in a porous micro-model. Despite the evidence of highly energetic bursts during the interface displacement process, and the potential enhancement of inertial effects, such effects have largely been neglected. A critical aspect in investigation of the inertial effects is the velocity field data. Currently no velocity data exist in the literature for these flow systems. This is due in part to the technical challenges involved in performing instantaneous pore-

scale velocity measurements using state of the art optical diagnostics. Particle image velocimetry (PIV) is the most established technique for field velocity measurement. Micro-PIV is one of its variants that uses a microscope to capture images in micro-scale configurations. Although micro-PIV is a well-established technique for canonical single phase flows, in the case of multi-phase flows tackled here, numerous challenges must be overcome, which this thesis aspires to address.

1.5 Goals and objectives

The overarching goal of this thesis is to experimentally investigate the high-pressure, near critical flows of CO_2 that are relevant to CCS technologies. One important aspect of these flow systems is that transport and storage processes for CO_2 occur in the vicinity of the critical point of CO_2 (74 bar, 31°C). Thus, the physical properties of fluids become increasingly sensitive to changes in pressure and temperature near the critical point, and such changes can potentially affect the flow. Another unique feature of these flows is that they occur, to a substantial extent in porous media, in manners that are currently not fully understood, although some initial experimental data tend to indicate that they can differ substantially from typically-assumed Darcy flow. In order to achieve the overarching goal, the following specific research objectives were pursued:

- Experimentally establish the fundamentals of near-critical CO_2 hydraulics. This involved studying flow in pipes and small orifices and measuring the pressure drop as a function of mass-flow rate and temperature. Particular importance was placed in a comparison with classical hydraulics and a powerful use of the Moody chart was established. This was established by shadowgraph data that were used in order to visualize the flow structure during transition from a supercritical to a subcritical state.

- Establish an ability to quantify fluid dynamics of multi-phase flow of supercritical/liquid CO_2 and water in porous media. The state of the art for such flow systems is focused on macroscopic measurements of saturation, capillary pressure, relative permeability, etc. More recently, pore-scale parameters such as interfacial velocities, interfacial areas and curvature have been achieved as well. Interfacial velocity measurements have indicated Haines jumps with velocities up to three orders of magnitude greater than bulk fluid velocity that point to the potentially crucial role of inertial effects in such flows. In order to quantify such inertial effects, a quantitative measurement of the spatially- and temporally-resolved fluid velocity field is required (as opposed to the aforementioned interface velocities surmised from time-delayed images of the interface displacement). Pore-scale velocity measurements in such flow systems do not currently exist. To that end, the microscopic particle image velocimetry (micro-PIV) technique was adapted for this purpose.
- Develop an experimental setup and methodology to apply the micro-PIV technique to multi-phase flow of liquid/supercritical CO_2 and water in silicon porous micro-models. Such configurations are considered unchartered territory for the micro-PIV technique.

1.6 Figures and tables

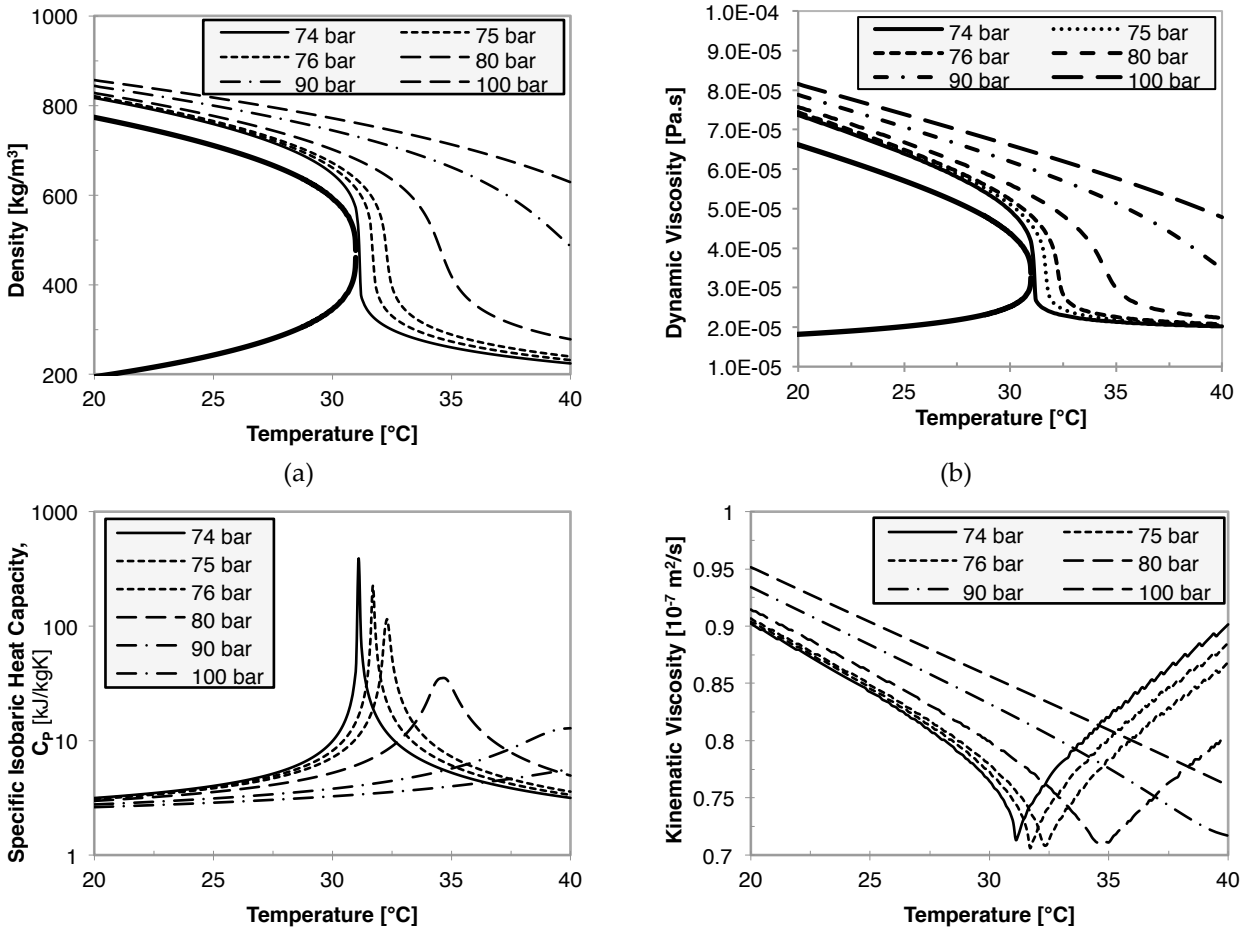

Figure 1.1 – CO_2 Properties Isobars based on the data of NIST [14]
a) *Density* **b)** *Dynamic viscosity* **c)** *Isobaric heat capacity* **d)** *Kinematic viscosity*

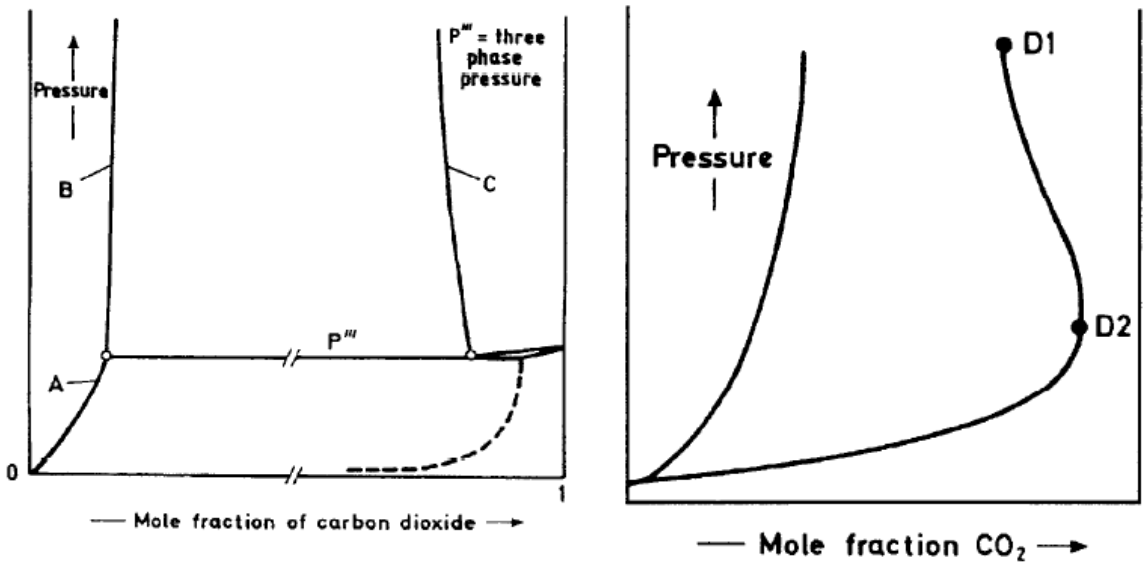

(a) (b)

Figure 1.2 – Solubility diagrams of subcritical (panel (a)) and supercritical (panel (b)) CO_2 in water. Adapted from [20].

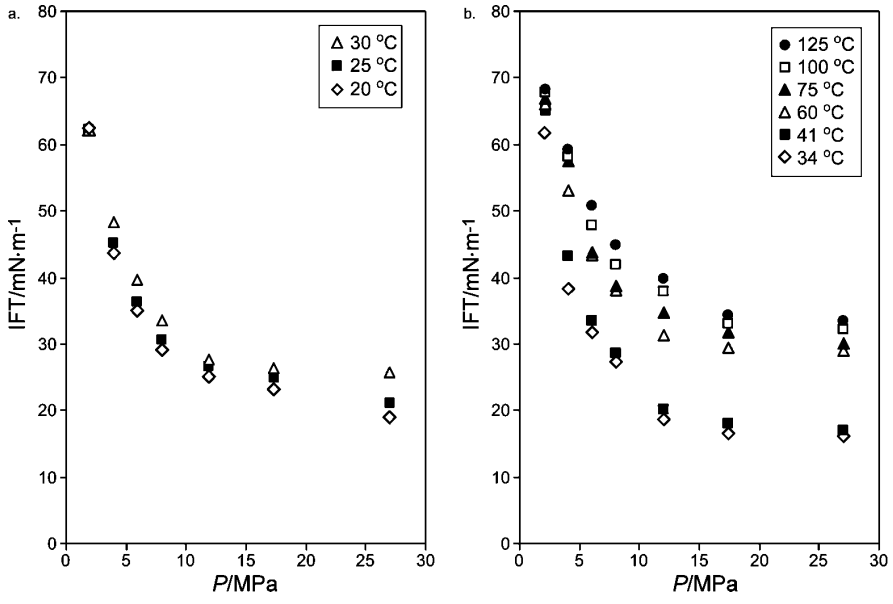

Figure 1.3 – Interfacial tension from Bachu & Bennion [27]

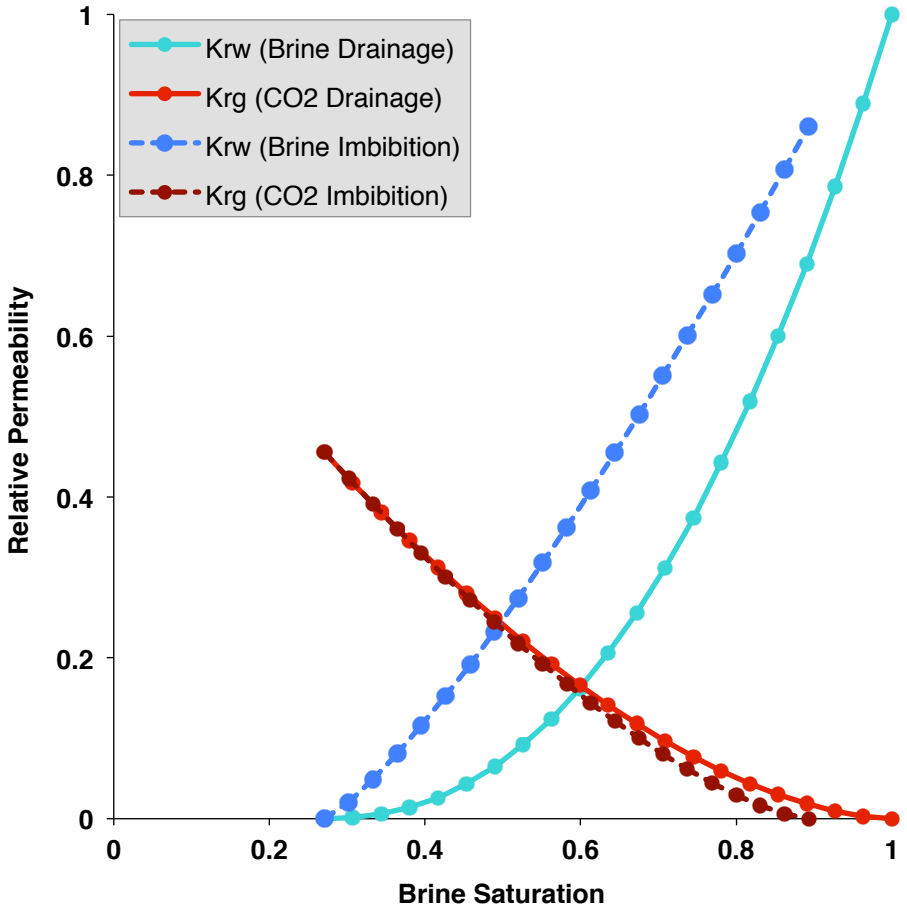

Figure 1.4 – Relative permeability vs. Brine saturation curve for a core sample from Cardium Formation for IFT of 33.5 mN/m (From Bennion & Bachu data [29]*)*

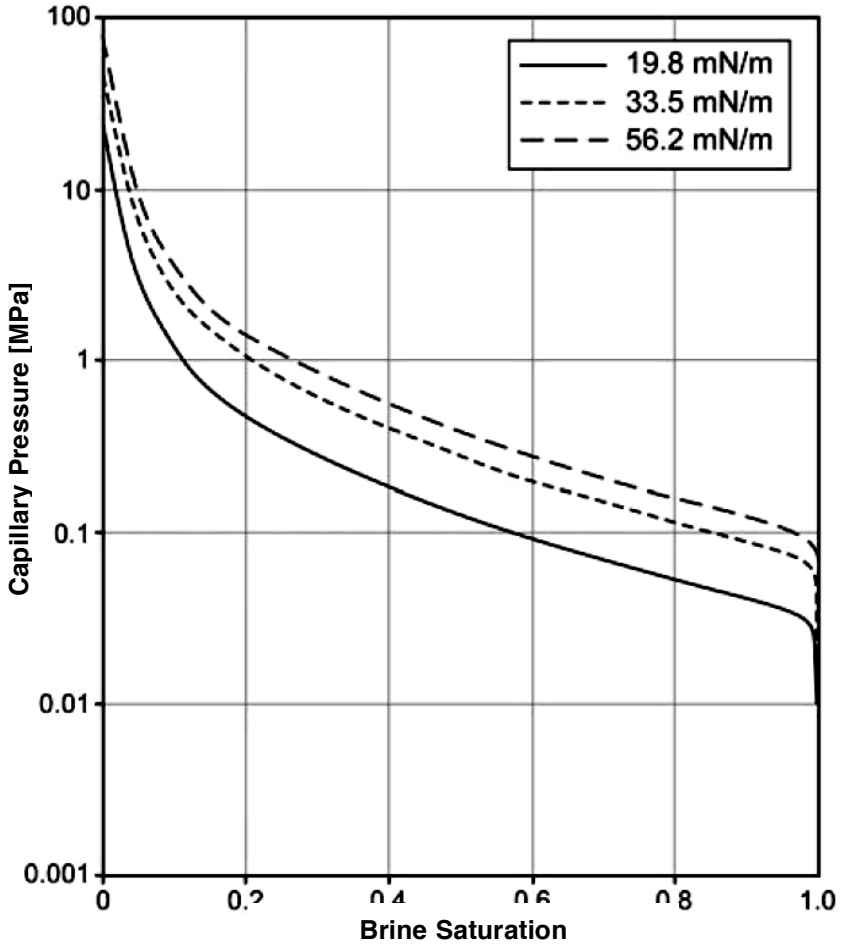

Figure 1.5 – Capillary pressure vs. Brine saturation curve for a core sample from Cardium Formation (Adapted from Bennion & Bachu data [29]*)*

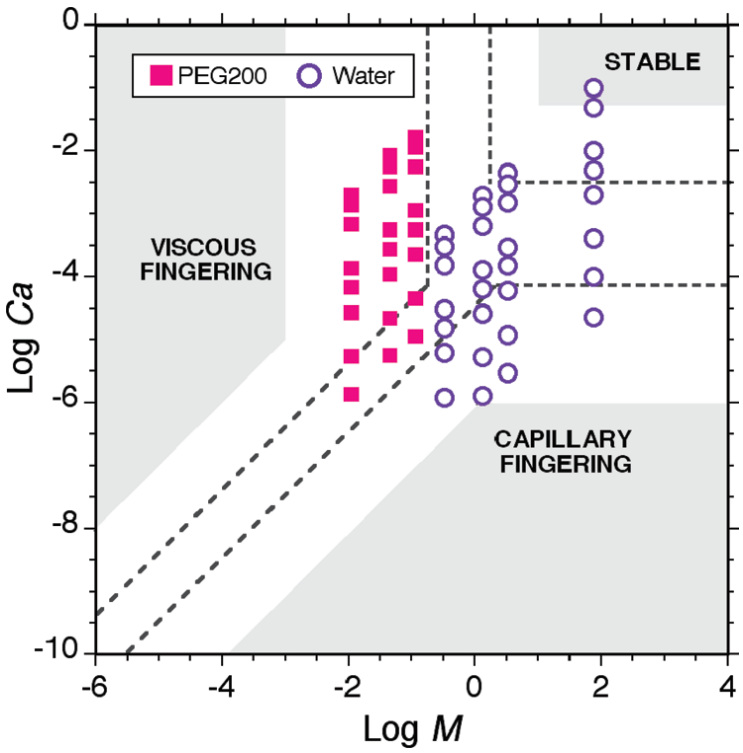

Figure 1.6 – Viscosity ratio vs. capillary number phase diagram (Adapted from [47]*)*

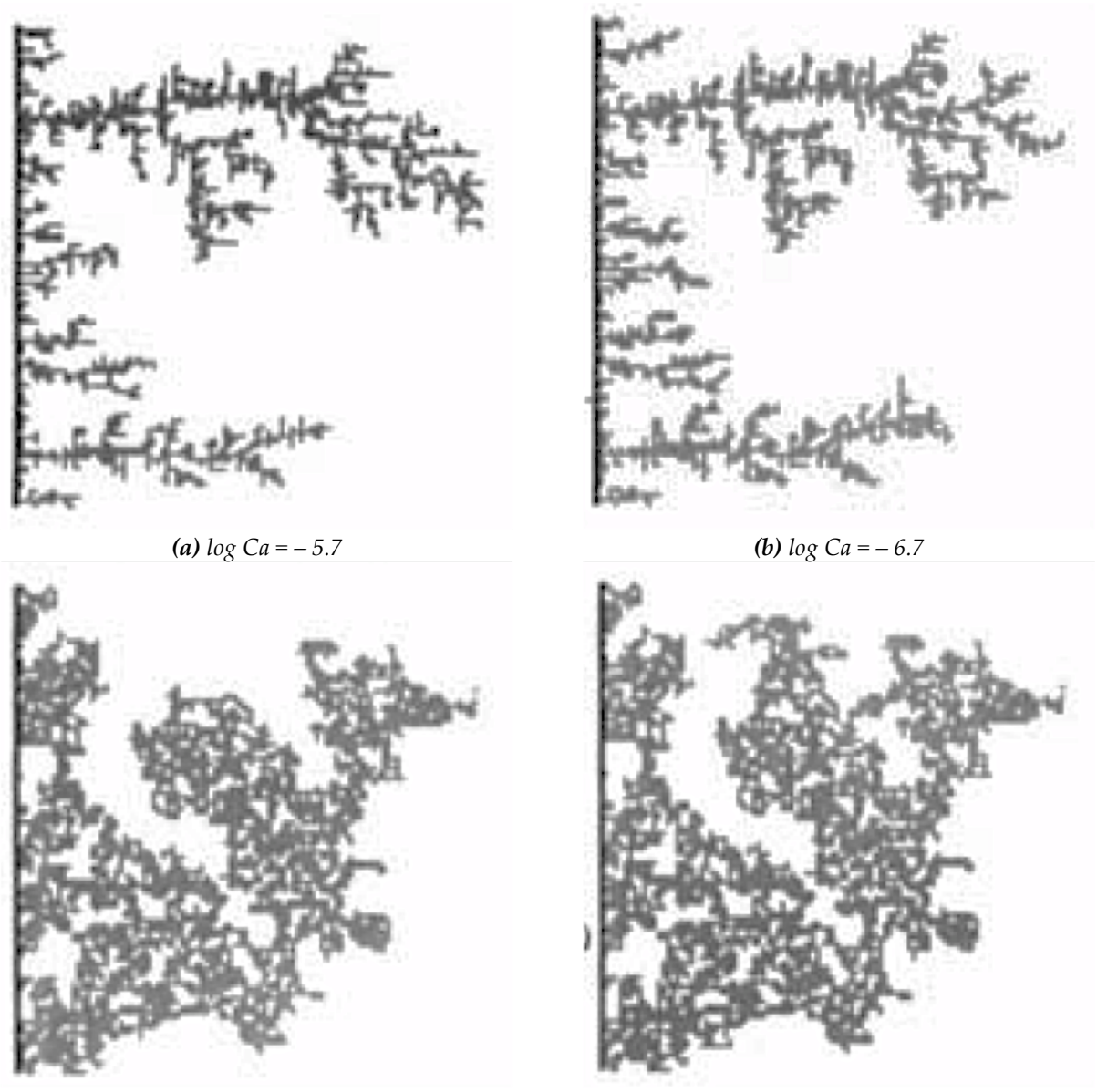

(a) *log Ca = – 5.7* ***(b)*** *log Ca = – 6.7*

(c) *log Ca = – 9.7* ***(d)*** *log Ca = – 10.7*

Figure 1.7– Fingering mechanism from the results of numerical simulation for log M = – 4.7
a, ***b***: *Viscous fingering,* ***c***, ***d***: *Capillary fingering*
Adapted from [46]

2. Experimental apparatus & measurement methods

2.1 Pipe-flow experiment

The experimental setup for the pipe-flow experiments is shown schematically in Fig. 2.1. A 1-lt Parker piston accumulator was used to compress CO_2 to the desired pressure using high-pressure nitrogen. Three different test sections were used in this setup. The first one was a stainless steel pipe, 60 cm (2 ft) long with 6.35 mm (0.25 in) outer diameter and 2.13 mm (0.084 in) inner diameter. The pipe was used to study flow of CO_2 near its critical point, which has significance in CO_2 transport in pipelines to the storage sites. The second test section was a stainless steel orifice with 0.36 mm (0.014 in) diameter (O'Keefe Controls Co., Trumbull, CT). It was used to study the Joule-Thomson throttling process and the cooling effect caused by sudden expansion of high-pressure CO_2. The third test section, which was an optically accessible high-pressure chamber (Jerguson, Strongsville, OH), incorporated two tempered borosilicate glass windows on opposite sides of the chamber and a rectangular flow cross-section approximately 16 mm × 35 mm. The inlet and outlet were located at the top and the bottom of the chamber, respectively. The chamber was approximately 12.7 cm (5 in) long with a visible range of 9.5 cm (3¾ in), rated at 138.0 bar (2000 psi) for operation at 38°C. This test section was used for visualization purposes.

Pressure and temperature at the inlet and outlet of the test section were measured using pressure transducers and T-type thermocouples, respectively. The pressure transducers (Setra 209) measured the gage pressure up to 206.8 bar (3000 psi) with ±0.25% full-scale accuracy (±0.5 bar). Pressure drop in the pipe was measured using a differential pressure transducer (Rosemount 3051C) with 0-1000 in-H_2O (0-

250 kPa) range and 0.15% accuracy. Ungrounded T-type thermocouples in a 0.062 in (1.6 mm) diameter sheath were used for temperature measurements. Cold junction compensation (CJC) was accomplished using the DAQ Assistant virtual instrument for T-type thermocouples. For the Joule-Thomson experiment, pressure drop across the orifice was obtained by subtracting individual pressure transducer readings. Mass flow rate was measured using a Coriolis mass flow meter (Micro Motion CFM010) with 0.1% accuracy. Data acquisition and monitoring of the measurement devices were performed using National Instruments LabVIEW software. The voltage signals from diagnostic instruments including the thermocouples, mass flow meter, and pressure transducers were captured by a National Instruments BNC-2110 shielded connector block, connected to a National Instruments PCI-6036E card installed in a PC.

During the experiment, with valves 1 and 3 initially closed, the system was filled with CO_2 (99.9% purity) from a tank to a pressure of approximately 50 bar and room temperature. Then, valve 2 was closed and CO_2 was compressed using high-pressure nitrogen by opening valve 1 and gradually increasing the pressure of nitrogen line until the piston reached the bottom of the cylinder. At that point the pressure of CO_2 in the system was approximately 65 bar, which was subcritical. Thus, by opening valve 3 nitrogen was vented from the accumulator and it was refilled with CO_2 to 50 bar. The check valve prevented the compressed CO_2 in the cylinder from being depressurized. The same process was repeated 2-3 times until the pressure inside the cylinder reached approximately 100 bar. As a result of the compression, the CO_2 temperature rose from near room temperature to near the critical temperature of CO_2. Further adjustments in the initial temperature of CO_2 were accomplished with an electric tape heater and ice-filled cold packs as needed. Flow measurements were performed by allowing the CO_2 to expand and exhaust to the ambient air by opening the needle valve installed downstream of the test section. This needle valve was also used for controlling the mass flow rate.

One of the difficulties associated with these experiments was that the fluid conditions (P, T, ρ) were not easily controlled. This was due the fact that $(\partial\rho/\partial P)_T$ and $(\partial\rho/\partial T)_P$ become very large near the critical point (shown in Fig. 1.1.A), and pressure was controlled by applying pressure upon a moving piston. Thus, as pressure and volume (density) were affected simultaneously, precise control of the initial pressure and temperature of the fluid was not easily attainable.

2.2 Porous micro-model experiments

In the porous micro-model experiments, porous two-dimensional micro-models were fabricated from silicon. The micro-model was then used to study multi-phase flow of water and liquid/supercritical CO_2. The details of the design and experimental procedure are described in the following sections.

2.2.1 Porous micro-model design and etching

The design of the porous micro-models along with the relevant geometrical parameters is shown in Fig. 2.2. The design parameters are shown in Table 2.1. The porous micro-models were manufactured based on a previously reported micro-fabrication technique [81]. The micro-fabrication process was carried out in the Micro-Nano-Mechanical Systems (MNMS) cleanroom in the Department of Mechanical Science and Engineering in the University of Illinois. The silicon wafers used were single-sided polished, 100 mm in diameter, 500 μm thick with <100> crystal. The wafers were spin-coated with Microposit™ SPR™ 220-4.5 photoresist (PR) material with a thickness of approximately 5 μm which acted as a mask for the etching of the wafer. The wafer was then soft-baked on a hotplate at 60°C for 2 minutes and at 110°C for another 2 minutes. Next, a chrome mask with the channel design was placed on top of the wafer and the PR was exposed to UV light at 14.5 mW/cm^2 for 16 seconds. The exposed PR was then removed from the wafer surface by placing the wafer in a 1:5-per-volume solution of AZ-400K developer in deionized

water for approximately 1 minute. The photoresist was then hard-baked for two minutes on a hotplate at 110°C. The unmasked area of the wafer was etched to a depth of approximately 30 μm in an inductively coupled plasma (ICP) deep reactive ion etching (DRIE) Plasma-Therm machine at a rate of approximately 2 μm/min. After etching, the photoresist was removed by placing the wafer in a bath of Microposit Remover 1165 at 80°C for approximately 10 minutes and rinsed with deionized water. After this step, the backside of the wafer was spin-coated with AZ-4620 photoresist with a thickness of ~10 μm, and soft-baked at 110°C for 2 minutes on a hotplate. Next, a chrome mask with the fluid-delivery ports design was placed on the wafer and exposed to UV light in a flood expose at 14.5 mW/cm^2 for 60 seconds. After exposure, the wafer was placed in 1:3 AZ-400K/deionized water solution to develop and remove the exposed photoresist. The wafer was next hard-baked for 15 minutes on a hotplate at 110°C. The ports were through-etched in the ICP-DRIE Plasma-Therm machine. The remaining photoresist was removed using a Microposit Remover 1165 bath at 80°C for 10 minutes.

2.2.2 Micro-model assembly

The etched silicon wafer was bonded to a glass wafer by a field-assisted thermal bonding (a.k.a. anodic bonding) process. For this purpose, a double-sided polished Schott Borofloat 33 glass wafer, 500 μm thick and 100 mm in diameter was used. The etched silicon wafer and the glass wafer were first cleaned using the RCA Standard Clean 1 (SC-1) cleaning process [82] in preparation for bonding. The process involved submerging the wafers in a basic 5:1:1 per volume solution of deionized water : ammonium hydroxide : hydrogen peroxide at 80°C for 10 minutes. This process removed the organic insoluble contaminants from the wafer surface. The wafers were then rinsed with deionized water, blown dry with nitrogen, and dehydrated on a hotplate at 110°C for 10 minutes. The glass wafer was then placed on top of the etched silicon wafer and put in an insulated box furnace between two finely-polished graphite plates that acted as electrodes. The bottom plate was a 4"× 4" square and 0.5" thick. The top

plate had the same thickness but was cut to a diameter of 3.5″ in order to prevent short-circuiting between the two electrodes. A 3-mm thick glass plate was placed under the lower graphite plate for insulation. For the same reason, glass slides were placed on top of the upper graphite plate. A stainless steel block (~4 kg) was used to provide pressure that ensured complete contact and no air pockets between the two wafers. The top and bottom electrodes were wired to the negative and positive ports of a high-voltage DC power supply, respectively. The oven was heated to 425°C and once the temperature remained steady, a 900 V potential was applied to the electrodes for 30 minutes. The power supply and the oven were then turned off and the oven door was left slightly open to allow it to cool down to room temperature.

2.2.3 Microscopic particle image velocimetry

Particle image velocimetry (PIV) is a non-invasive flow measurement technique based upon imaging wherein the fluid is rendered visible by seeding it with tracer particles [83]. In the standard, macro-scale implementation of PIV, particles are illuminated with a thin sheet of laser light and their distribution within the illuminated plane of the fluid is recorded at precise times. In order to track the fluid motion, in the classic PIV approach, two consecutive images are taken at t_0 and $t_0 + \Delta t$. The average displacement of the particles within small regions of the image, called interrogation windows, can be determined by cross-correlation analysis. The displacement vector in the illuminated plane, $\overrightarrow{\Delta x}$, divided by Δt gives the velocity vector $\vec{u}$. The PIV technique is a well-established flow measurement technique in both micro- and macro-scale fluid systems. Although it was originally developed for macro-scale systems, the same basic principles can be employed to devise a system for velocity field measurements in the micro-scale systems where certain technical challenges must be overcome. Santiago et al. [84] and Meinhart et al. [85] pioneered the development and application of PIV to microscopic channel devices, commonly referred to as micro-PIV. In this implementation, a microscope is employed in order to obtain

appropriate magnification of the fluid region being investigated. The fundamental difference between micro-PIV and standard PIV is the technique used for illuminating the tracer particles. In two-dimensional measurements for macro-scale applications (2D-PIV), a laser sheet is generated which thus defines a measurement plane within which the velocity field is resolved. In micro-scale applications, due to geometrical constraints, generating a laser sheet with the appropriate thickness (i.e. few microns) is impractical. Therefore, the entire depth of the test section is illuminated instead. In this configuration, it is the focal plane of the microscope objective that defines the imaging plane rather than the plane illuminated by the laser sheet in standard PIV. Thus, the main challenges with such an approach are due to noise generated by particles outside the focal plane of the microscope and reflections from the background. Particles within the focal plane, or very close to it, can be imaged and appear sharp, while those outside of the focal plane are dim. For this reason, in microscopic PIV applications, it is critical to accurately control a quantity called depth of measurement which defines the thickness within which particles provide enough signal to significantly contribute to the cross-correlation function. According to Meinhart et al. [86], the depth of measurement can be estimated as:

$$\delta z_m = \frac{3n\lambda_0}{NA^2} + \frac{2.16 d_p}{\tan\theta} + d_p \qquad 2.1$$

In this equation, δz_m is the depth of measurement, n is the refractive index of the fluid between the microfluidic device and the objective lens, λ_0 is the illumination wavelength, NA is the numerical aperture, d_p is particle diameter, and θ is the light collection half-angle of the objective lens. In the experimental setup used here, n = 1, λ_0 = 532 nm, NA = 0.25, d_p = 1 μm, and tan θ = 0.258, the depth of measurement from Eq. 2.1 is 35 μm, which is slightly larger than the depth of the micro-models (~30 μm). As a result, once the focal plane is roughly positioned at the center of the micro-model depth, all tracer particles within the depth of the micro-model will contribute to the cross-correlation function.

As already mentioned, volume illumination introduces challenges associated with illumination light scattered off of flow surfaces that can obscure the light scattered or fluoresced from the tracer

particles. A macroscopic PIV system is set up such that scattering and reflection off of various objects (e.g. channel walls, optical access windows, etc.) is minimized. However, in a microscopic PIV system stray scattered light is unavoidable. To alleviate this issue, the classic fluorescent microscopy technique is applied wherein the fluid is seeded with particles that are tagged with a fluorescent dye. Thus, while in standard PIV Mie-scattered light from particles is recorded, in micro-PIV fluorescent emission from the fluorescently-tagged particles is recorded. The fluorescent emission occurs at a longer wavelength than the incident light, meaning that an optical filter (low-pass or band-pass) upstream of the imaging medium can be used to suppress illumination light scattered from the background and allow only the light fluoresced from the tracer particles to be imaged. The downside of this approach is that the fluorescent signal is often much weaker than Mie-scattered light and the limited efficiency of most filters may further decrease the fluorescent signal that reaches the image sensor.

A crucial matter in all PIV measurements is the ability of the tracer particles to faithfully follow the motion of the fluid. In this regard, the main particle characteristics that can be controlled are their density and size. For the particular experiments under consideration in this thesis, it is very reasonable to assume that flow conditions fall within the Stokes flow regime, so the characteristic response time of a tracer particle, τ_p, is given by:

$$\tau_p = \frac{d_p^2 \rho_p}{18\mu} \qquad 2.2$$

In this equation, d_p is particle diameter, ρ_p is particle density, and μ is the fluid viscosity. With d_p = 1 μm, ρ_p = 1050 kg/m^3, and μ = 0.001 Pa.s, the response time for the seed particles used for water is $\tau_p \approx 0.06$ μs. The choice of these particles is justified in the immediately following section. The characteristic flow time-scale range expected for our experiments can be estimated from dividing the smallest dimension in the micromodels (~50 μm) by the bulk velocity (0.5–5 mm/s) which yields a range of 10–100 ms. Thus the Stokes number, defined as the ratio of characteristic stoppage time of particle to characteristic time of

flow, is within the 6×10^{-4} – 6×10^{-3} range. This indicates that these particles can easily respond to all flow and thus will accurately follow the motion of the fluid [83].

In these experiments, the flow field was such that the maximum velocity in the field could vary by 2 orders of magnitude during the course of the flow. Due to the occurrence of this high dynamic range, in some cases cross-correlation analysis was performed twice in order to be able to resolve both small and large displacements from the same dataset. This was accomplished by considering image pairs with two different time delays. More specifically, the high velocity displacements were resolved relying on the classical PIV straddle acquisition method that allowed the capture of two frames within a short time interval (Δt_1 = 1–10 ms) and thus observe fast occurring phenomena. This first short Δt was obtained by firing the two heads of a dual-pulsed laser. In the second case, we instead correlated the first frames (frame A) of consecutive image pairs, in order to resolve the low velocity phenomena. In this case, image pairs with a time delay of Δt_2 = 100 ms, set by the 10 Hz frequency of the laser, were used to observe the dynamics of more slowly evolving phenomena.

The uncertainty of the displacement vector from cross-correlation analysis of images is 5% of the particle-image diameter, which is approximately 0.1 pixels and corresponds to 0.07 μm. Considering the time-delay of 6 ms and 100 ms (used for data presented in section 4.1), the resulting uncertainty is 0.01 mm/s and 0.001 mm/s, respectively [87]. Also considering that average particle-image diameter is approximately 2 pixels, the peak-locking errors are expected to be negligible [88].

2.2.4 Fluorescent particles and dye

Extensive research was performed in order to find ideal seeding particles for water and CO_2. Fluorescent particles for micro-PIV applications are typically polymers or glass spheres. However, the ideal particles for this unique application must meet several criteria simultaneously, including size, density, physical/chemical compatibility and spectral characteristics. However, it occurred that all of

these criteria could not be met simultaneously and a compromise was made. To seed the aqueous phase, commercially available FluoSpheres® 1.0 μm Microspheres with Nile Red fluorescent dye from Life Technologies were selected. The criteria used in the selection process are explained in detail below.

i. Size

Considering the application of flow in a micro-scale porous network, the particles must be small enough to minimize the risk of obstructing the 40–50 μm throats. From a measurement resolution stand point, the particles need to be small enough to provide sufficient particle number density in the fluid such that each PIV interrogation window contained a sufficient number of particles to obtain a reliable velocity measurement. At the same time, the particles must be large enough to provide enough light signal to be captured by the imaging system and to avoid issues of peak-locking associated with under-resolved particle images [88]. In this latter regard, the recommended particle-image size to avoid such issues is 2–3 pixels in diameter. Taking the magnification of the optical system (~0.65 μm/pixel) into account, 1-μm-sized particles were deemed suitable in all regards.

ii. Density

The next aspect is the density of the particles, which is desired to be as close as possible to fluid density in order to minimize buoyancy/gravity effects. Concerns of particles settling/rising were mostly associated with the vertical cylinder of the syringe pumps, particularly because of the long residence time (at least 2 hours) of the fluids in the syringe pump. Furthermore, a density difference would result in particles gathering near the top or bottom surface of the micro-model. For water, the only particles that satisfied both the density and the size criteria were polystyrene (PS) particles with specific gravity of 1.05. Identifying suitable particles for CO_2 is more challenging because the CO_2 density varies considerably over the range of pressures and temperatures studied in this thesis. For instance, at 80 bar its density changes from approximately 300 kg/m^3 to 800 kg/m^3 when temperature varies from 40°C to 22°C. After

significant research, it was established that no particles were available that could simultaneously meet the density and size criteria for seeding CO_2. Thus, it was decided to seed water with particles and simply dye the CO_2 phase with a fluorescent dye instead. It should be noted that the particles chosen for seeding the water phase met the Stokes number criterion outlined above (Eq. 2.2).

iii. Physical and chemical compatibility

Another aspect of experiments that posed challenges for particle selection was the fact that some polymers are not chemically compatible with liquid/supercritical CO_2 as they may become unstable (e.g. can swell or dissolve in CO_2). This issue not only limits the options for seed particles for the CO_2 phase, but also for the water phase as well because the water seed particles will eventually interact with the CO_2 at the water-CO_2 interface. For example, among the polymers commonly used for manufacturing fluorescent particles, polystyrene is soluble in CO_2 when its molecular weight is less than 1000. On the other hand, polyethylene (PE) and poly(methyl methacrylate) (PMMA) are not soluble in CO_2 [89]. However, PE and PMMA particles do not meet the density criterion and thus their use as seed particles in either water or CO_2 is not a viable option. Based on density, PS is the only suitable candidate for use in water. It is worth mentioning that these fluorescent particles, also referred to as molecular probes, are almost exclusively used in biological applications. Thus, compatibility with supercritical CO_2 has never been investigated and the manufacturers have not published any relevant data on this issue. In conclusion, due to the limited number of seeding options available, the 1-μm polystyrene particles were used to seed water, and they demonstrated to be well suited for our application and did not introduce any major issues.

As an alternative, particles made from cross-linked poly(styrene/divinylbenzene) (P[S/DVB]) were also tested. This cross-linked polymer offers superior heat and solvent resistance to the particles, but due to their special manufacturing process their smallest available size is 2.2 μm. The advantage in using

these particles over regular 1-μm PS particles appeared to be minimal, and with their cost per particle count being 20 times higher than the cost of regular PS particles, it was decided to use the 1-μm PS particles.

iv. Absorption (excitation) and emission spectra

Fluorescent particles of a given size and material can be tagged with specific fluorescent dyes to obtain desired excitation and emission spectra for effective separation of the fluorescent emission and illumination wavelengths prior to imaging. The dye encapsulated within the particles was selected based on the specifications of the available excitation source. Pulsed lasers are the most commonly used illumination source in micro-PIV experiments. In this work, a pulsed, dual-cavity, frequency-doubled Nd:YAG laser (532 nm) was used. Thus, based on the 532 nm wavelength of the excitation source, fluorescent particles were selected with Nile Red dye encapsulated within. According to the product specifications, the dye has relatively wide absorption and emission bands with peaks at 535 nm and 575 nm, respectively.

Fluorescent dye for CO_2

Once it was realized that seed particles for CO_2 with suitable size and density could not be found, it was decided to instead tag CO_2 with a fluorescent dye so that its regions of occupation could be clearly identified within the porous micro-models. As a result, the velocity field in the CO_2 phase could not be measured, though the CO_2 phase was visualized and distinguished from the aqueous phase. The main criterion for this dye is that it be soluble in CO_2 but not soluble in water. A candidate that satisfies this criterion is Coumarin 153 (C153). Zhang et al. [65] and Wang et al. [66] have successfully used this dye in previous flow visualization experiments. Another characteristic that is desirable but not strictly required is that the fluorescent dye and the water seed particles be excited at the same illumination wavelength. For C153, the absorption band ranges from approximately 350–500 nm with the peak at 425 nm. Thus, a

separate illumination source was required for exciting C153, because the 532 nm laser fell outside the absorption band of C153. A LED with 410 mW power output, emission peak at 405 nm and 20 nm full width at half maximum (FWHM) was used as the excitation source for this purpose.

2.2.5 Apparatus

A schematic diagram of the experimental setup for the micro-PIV experiments is shown in Fig. 2.3. In this setup, two high-pressure syringe pumps (Teledyne Isco 100-DM) were used for CO_2 and water. These pumps were utilized because of their ability to provide flow at the high pressures required to achieve liquid/supercritical CO_2 conditions as well as for their ability to maintain highly accurate flow rates (0.5% of set point accuracy) at these pressures. Further complicating the experimental arrangement was the need to ensure the structural integrity of the micro-models at these high pressures. Typical microfluidic devices constructed in the manner utilized herein can withstand only a few psi of pressure, beyond which the bond between the silicon model and the cover glass is compromised. Thus, to achieve the 80-90 bar pressures required herein to achieve liquid/supercritical CO2, the micro-models were placed in a pressure cell with optical access through a 0.25″ thick sapphire window at the bottom with 1.5″ viewable diameter. The pressure cell was filled with glycerol and was pressurized with a piston accumulator using nitrogen. The pressure inside the pressure cell (outside the micro-model) was always maintained at approximately 5 bar higher than the pressure inside the micro-model to ensure uncompromised bonding between the silicon and glass of the micro-model. A temperature-controlled water bath was used to maintain the temperature of the fluids inside the syringe pumps constant. In addition, a temperature-controlled chamber was mounted on the microscope to ensure constant and uniform temperature.

CO_2 was initially left undyed and thus appeared as dark regions in the images. This condition made image processing challenging since the cylindrical posts in the micro-model also appeared as dark

regions and distinguishing between them in a robust manner was not easily achievable. In subsequent experiments, the CO_2 was dyed with C153 following the procedure reported by Zhang et al. [65]. A 10 mm stock solution of C153 in methanol was prepared. 1 ml of the solution was added to pump 1 prior to the experiment, and the methanol was vaporized by purging the cylinder with CO_2 for at least 12 hours. Upon filling the syringe pump with CO_2 and pressurization, the dye would dissolve in CO_2.

Optical setup

Visualization was performed using fluorescent microscopy with spectral image separation. An Olympus IX-73 inverted microscope with a 10X, 0.25 numerical aperture (NA) objective, coupled to two Andor Neo sCMOS 5.5 megapixel 16-bit cameras was used to capture images. The cameras have a peak quantum efficiency (QE) of 60%, with maximum burst and continuous capture rate of 49 and 30 frames per second, respectively.

A dual-cavity, Nd:YAG laser with a maximum energy of 160 mJ per pulse at a wavelength of 532 nm was used as the excitation source for fluorescent particles. A LED with 410 mW power output, emission peak at 405 nm and 20 nm full width at half maximum (FWHM) was used as the excitation source for C153. A dichroic long-pass beamsplitter with edge wavelength of 506 nm was used to combine light from the two sources before entering the microscope. The configuration of the optical filters employed to block light from illumination sources and spectrally separate the emitted light from fluorescent particles (water) and C153 (CO_2), and the light path in the microscope is shown schematically in Fig. 2.4. Tables 2.2 and 2.3 show the transmission and reflection bands of the various filters.

Camera 1 and camera 2 were coupled to the right port and left port of the microscope, respectively. Camera 1 recorded emitted light from CO_2 only, and camera 2 recorded the image of both water and CO_2, due to the overlap between the emission spectrum of the fluorescent particles and C153. Figure 2.5 shows sample images from each of the two cameras. The image recorded by camera 1 was used

to identify the presence of CO_2 and thus accurately define the water-CO_2 boundaries. This spatial information, available for each realization, was then used to both investigate the dynamics of the menisci and to mask out CO_2 from the image recorded by camera 2. The images recorded from camera 1 were interrogated to resolve the flow field in the aqueous phase.

2.3 Figures and tables

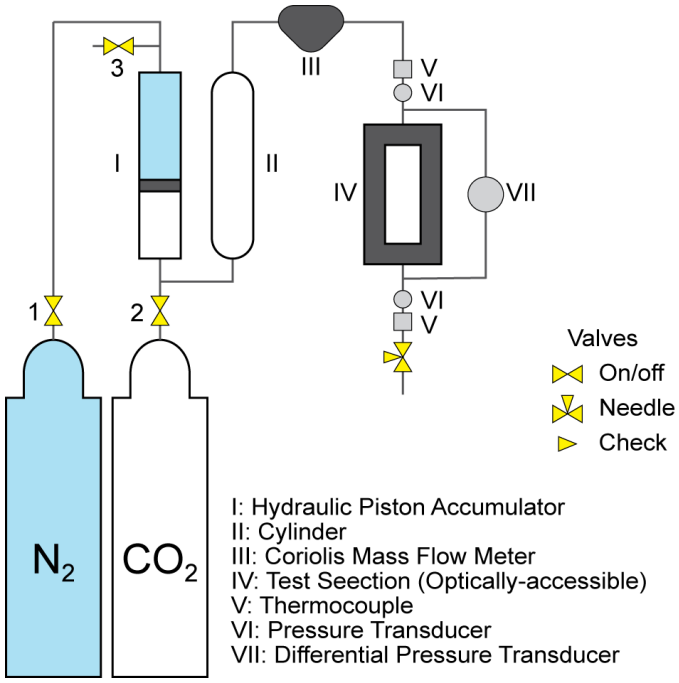

Figure 2.1 – Schematic diagram of the experimental apparatus for pipe-flow experiment

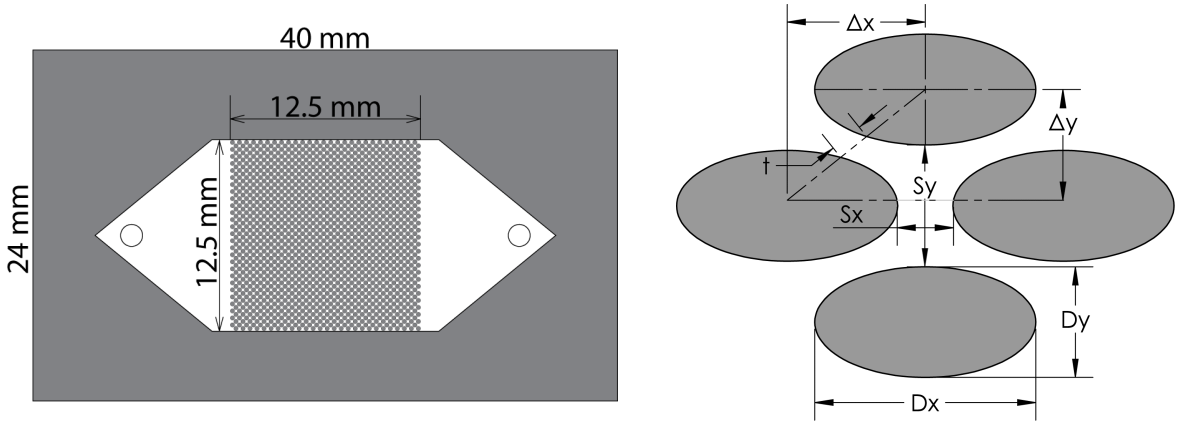

Figure 2.2 – Porous micro-model geometry

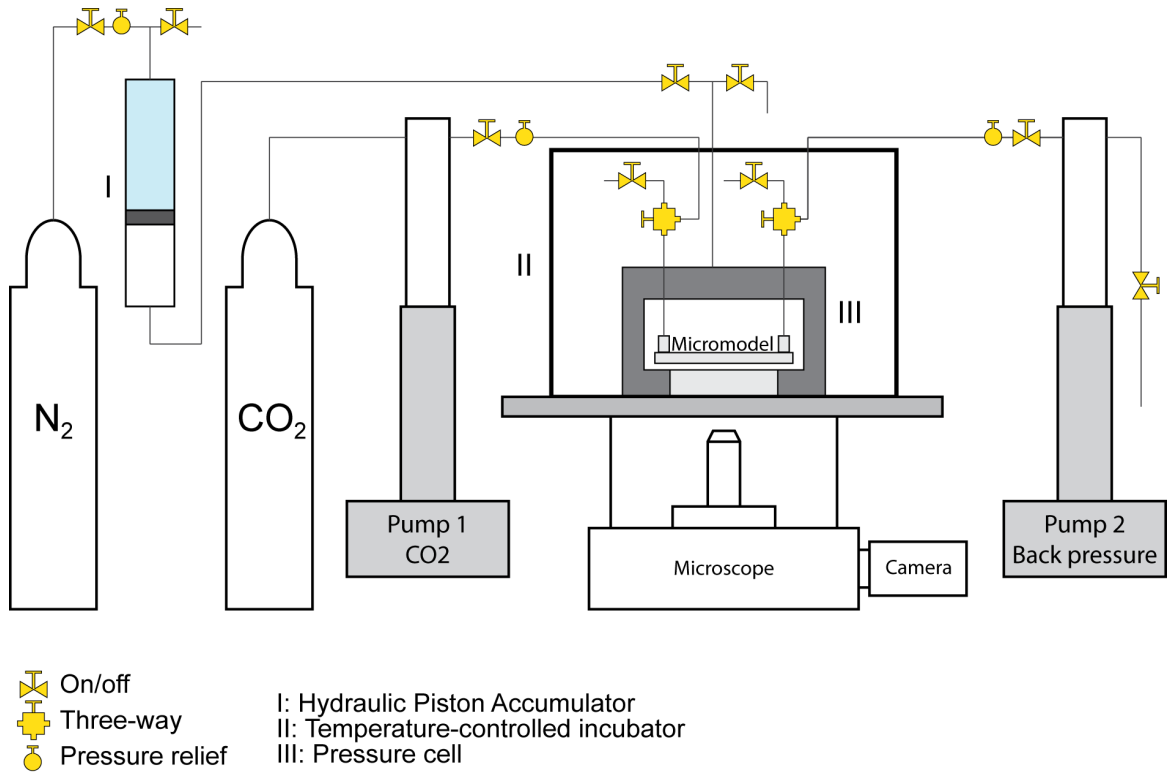

Figure 2.3 – Experimental setup for porous micro-model experiments

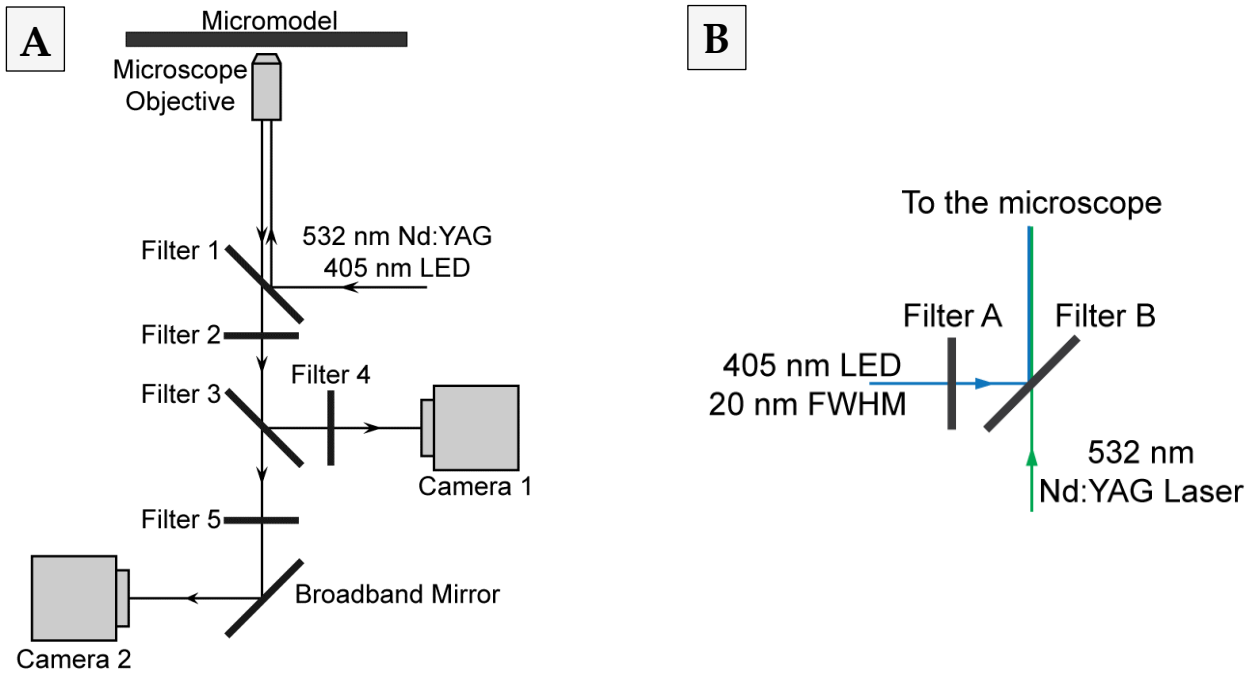

Figure 2.4 – Optical setup

A. *Microscope and the cameras* **B.** *Sources of illumination*

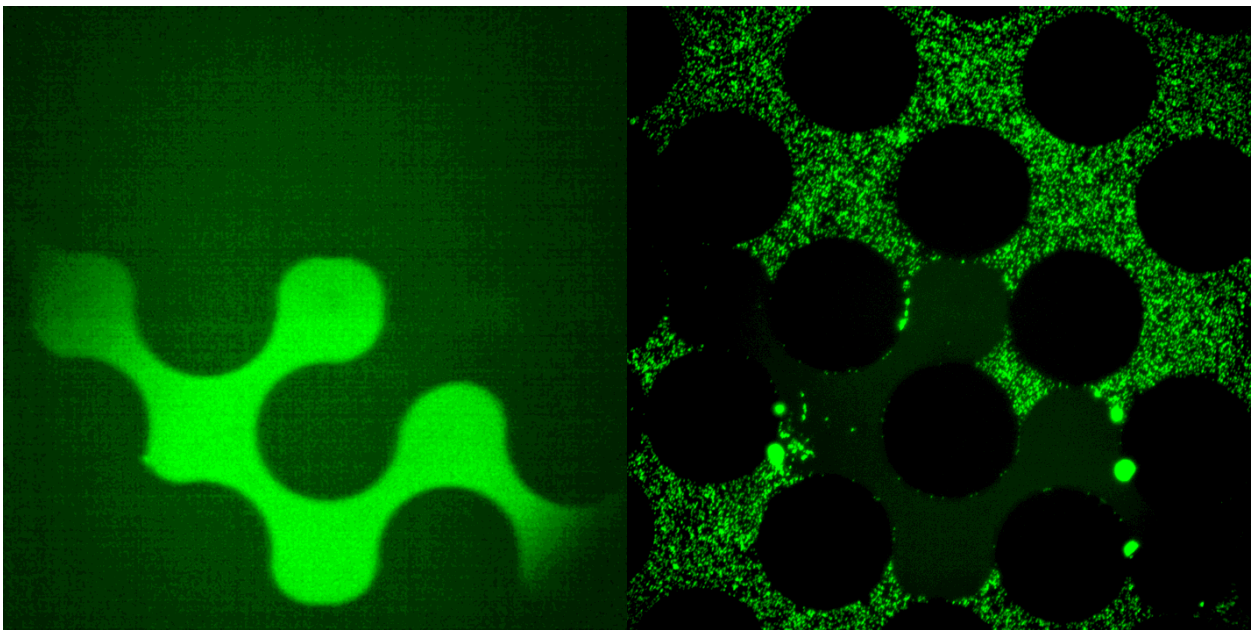

Figure 2.5 – Sample images from experiments
Left: *Dyed CO2 image from camera 1* **Right:** *Tracer particles image from camera 2*

Table 2.1 – Channel design parameters

Code	**I**	**II**	**III**	**IV**
D_x **[μm]**	300	300	400	200
D_y **[μm]**	300	300	200	400
S_x **[μm]**	180	236	100	100
S_y **[μm]**	180	236	300	300
t **[μm]**	39.4	79.0	101.8	101.8
Δx **[μm]**	240	268	250	250
Δy **[μm]**	240	268	250	250
Porosity [%]	39.6	51.6	50.5	50.5
Depth [μm]	~30	~30	~30	~30

Table 2.2 – Optical filters configuration (Fig. 2.4-A)

Filter	Transmission	Reflection
1	429.5 – 462 nm 502.5 – 518.5 nm 550 – 613 nm 663 – 800 nm	370 – 410 nm 473 – 491 nm 530.5 – 533.5 nm 632.8 – 647.1 nm
2	470 – 900 nm	None
3	523 – 690 nm	400 – 512 nm
4	464.5 – 499.5 nm	None
4	546.9 – 900 nm	None
5	562.5 – 587.5 nm	None

Table 2.3 – Optical filters configuration (Fig. 2.4-B)

Filter	Transmission	Reflection
A	362 – 396 nm	None
B	513 – 950 nm	350 – 500 nm

3. Pipe flow and throttling experiments

In this chapter the results of the measurements and visualizations performed on CO_2 pipe flow and throttling process in the vicinity of its thermodynamic critical point are presented. In the first section, pressure drop and mass flow rate data at constant inlet pressure and temperature are presented. In the second section, flow visualization results using the shadowgraph technique are presented. The third section deals with the throttling process and the Joule-Thomson coefficient of CO_2 near its critical point.

3.1 Pipe flow measurements

Pressure drop across the pipe test section was recorded for a range of inlet pressures and temperatures near the critical point for different mass flow rates. Figure 3.1 illustrates the location of the inlet conditions for the data of Figs. 3.2–3.7 on a ρ–T diagram with respect to the isobars, the saturation line, and the critical point.

Figures 3.2 and 3.3 show pressure drop per unit pipe length vs. mass flow rate at constant inlet temperature. The numbers next to each data point indicate the inlet temperature, and in the case of triplets of numbers, the three numbers represent mass flow rate, $\Delta P/L$, and inlet temperature, respectively. For example in Fig. 3.2 at 76 bar a mass flow rate of 5.6 g/s results in 59.4 kPa.m^{-1} pressure drop with inlet temperature of 35.8°C. In this graph, results are presented for an inlet temperature of 35.7±0.5°C, and inlet pressures of 80, 78 and 76 bar. A change in inlet pressure from 80 bar to 78 bar does not result in any significant alteration of pressure drop for a given flow rate. However, as pressure is

further lowered to 76 bar, ΔP drops by approximately 20% for $\dot{m} \simeq 3.7$ g/s. Also, ΔP remains unchanged for a 14% increase in mass flow rate from 4.9 g/s to 5.6 g/s as pressure is lowered from 78 bar to 76 bar.

Figure 3.3 presents data for an inlet temperature of 34.2±0.5°C at 76 bar and 74 bar inlet pressure. Compared to Fig. 3.2, there is significant scatter present in the data. Both pressure and temperature in Fig. 3.3 are closer to the critical point in comparison to Fig. 3.2, thus the increased scatter may be attributed to the increased sensitivity of thermophysical properties to pressure and temperature near the critical point that was shown in Fig. 1.1. Also, as in the case for 80 bar and 78 bar in Fig. 3.2, there is no notable difference between the results at 76 bar and 74 bar. Nevertheless, it seems that for higher mass flow rates ($\gtrsim$4.5 g/s), $\Delta P/L$ for a given mass flow rate increases as pressure is decreased from 76 bar to 74 bar, which is in contrast to the trend observed in Fig. 3.2.

The effect of inlet temperature on pressure drop is shown in Figs. 3.4–3.7 that present $\Delta P/L$ as a function of mass flow rate for various inlet pressures, ranging from 74 bar to 80 bar. As shown in Fig. 3.4, at 80 bar, in the mass flow rate range of approximately 3–5 g/s, $\Delta P/L$ varies very slightly as the temperature changes from 37.5°C to 35.7°C and 29.5°C. This indicates that with this specific set of conditions (P_{in}, T_{in}, $\dot{m}$), $\Delta P/L$ is insensitive to changes to inlet pressure and temperature. If the temperature is lowered to the subcritical temperature of 29.5°C, the effect of lowering the inlet temperature on pressure drop depends on the mass flow rate. At 4.4 g/s, this decrease in inlet temperature, does not result in any changes in ΔP, as $\Delta P/L$ is the same as it was for 37.5°C and 35.7°C. On the other hand, at 6.5 g/s, the very same change in inlet temperature (from 37.5°C to 29.5°C) results in a 42% reduction in ΔP, from 106 kPa/m to 61.9 kPa/m. This behavior demonstrates the existence of distinct flow regimes for the pipe flow based on the flow parameters (P_{in}, T_{in}, $\dot{m}$). These distinct flow regimes can have significantly different pressure drops. Another data point at 23.6°C and 5 g/s has approximately 35% lower pressure drop than what would be expected at 35.7°C–37.5°C temperature range. This behavior also suggests that

lowest ΔP at a given inlet pressure and for fixed mass flow rate can be achieved at subcritical temperatures.

In Fig. 3.5, for the mass flow rate range of 2–5 g/s, it appears that temperature change has minimal effect on pressure drop for the temperature range of 32.7–37.0°C. Similar to Fig. 3.4, this shows that at supercritical pressure and temperature, and for $\dot{m} < 5$ g/s, ΔP is not sensitive to changes in T_{in}. Considering the increased sensitivity of physical properties to changes in pressure and temperature near the critical point, it is expected that ΔP varies significantly with changes in pressure and temperature, however, the results point to the opposite for certain inlet flow conditions. Similar to the cases presented in Figs. 3.2–3.4, reducing the inlet temperature to the subcritical temperature of 29.2ºC results in a substantial reduction in ΔP relative to the case with supercritical temperature. In this instance there is a 46% reduction in ΔP at 6.2 g/s.

In Fig. 3.6, one important feature is the increased scatter as the critical temperature is approached. Similar to what was observed in Fig. 3.3 and Fig. 3.4, for $\dot{m} < 5$ g/s ΔP is barely affected by changing inlet temperature in the 34.0–36.0°C range. For mass flow rates higher than ~5 g/s the difference in ΔP for different inlet temperatures becomes evident. While at 3.8 g/s same $\Delta P/L$ has been measured for 34.0°C and 36.0°C, at 5.5 g/s, pressure drop is 40% less at 34.0°C compared to 36.0°C. Furthermore, at 5.9 g/s with same flow rates, ΔP at 29.1°C is 50% smaller than ΔP at 36.0°C. This is analogous to what has been shown in Fig. 3.4 and Fig. 3.5 for subcritical inlet temperature.

In Fig. 3.7, pressure drop vs. mass flow rate data are presented very close to the critical pressure. As in Fig. 3.6, it is observed that the scatter in data increases as the critical temperature is approached. Moreover, similar to what was shown in Figs. 3.4–3.6 for $\dot{m} \lesssim 5$ g/s there is no clear distinction between pressure drop for inlet temperature range of 33.0°C–35.1°C. However for $\dot{m} \gtrsim 5$ g/s, ΔP decreases as T_{in} is decreased. At 5.7 g/s, ΔP decreases by 24% as T_{in} is lowered from 35.1°C to 34.1°C. Also, for a change in T_{in} from 35.1°C to 33.0°C, 15% smaller ΔP is observed for 8% higher mass flow rate (6.9 g/s vs. 6.4 g/s).

Once more, it is observed that lowering the inlet temperature to subcritical results in sharp decrease in ΔP. At 3 g/s, reducing inlet temperature to 27.5°C results in 50% and 58% reduction in ΔP with respect to ΔP at 33.0°C and 34.1°C, respectively. Similarly, at 5.7 g/s, reducing inlet temperature to 28.8°C results in 44% and 58% reduction in ΔP (for 5% less mass flow rate) with respect to ΔP at 34.1°C and 35.1°C, respectively. These results indicate that despite the sensitivity of fluid properties to pressure and temperature in the near-critical region, ΔP is not necessarily influenced by changes in P, T. In fact, our data suggests that depending on mass flow rate and inlet conditions, ΔP can be insensitive to relatively large changes in inlet temperature.

As much as observations in terms of raw mass flow rates and pressure drops are revealing with respect to phenomenology, the hydraulics must also be studied in terms of relevant non-dimensional quantities. In order to compare the results with constant-density pipe flow, the friction factor f, was calculated as:

$$f = \frac{D}{L}\frac{\Delta P_f}{\rho_{in} U_{in}^2/2}$$

$$f = \frac{\pi^2 D^5}{8}\frac{\rho_{in}\left(\Delta P_f/L\right)}{\dot{m}^2} \tag{3.1}$$

In this equation, ΔP_f is the head loss caused by friction as opposed to ΔP that is the pressure difference across the tube. For a flow of varying density but very low Mach number, as the ones under consideration here, these two quantities can be related as:

$$\Delta P_f = \Delta P - \frac{1}{2}(\rho_{out} U_{out}^2 - \rho_{in} U_{in}^2)$$

$$\Delta P_f = \Delta P - \frac{1}{2}\left(\frac{\dot{m}}{A}\right)^2 (\rho_{out}^{-1} - \rho_{in}^{-1}) \tag{3.2}$$

The quantities ΔP and ΔP_f are not necessarily equal; however, it was found that the change in kinetic energy was negligible. Even in the case of most extreme change in density, ΔP_f differed from ΔP by less than 2%. Thus it is safe to consider $\Delta P_f = \Delta P$.

In Eq. 3.1, the reason for choosing ρ_{in} rather than average density or density at average pressure and temperature was that in some instances a sensible (~1–2°C) decrease in temperature occurred across the test section. It was in fact discovered that the temperature drop was mainly due to the configuration of the experiment. Specifically it was caused by the turns and curves in the flow path upstream of the test section. After modifying the flow path this temperature change dropped to roughly ±0.2°C which is within the uncertainty range of the employed thermocouples. Depending on inlet conditions, this change in temperature occasionally resulted in large changes in density between the inlet and the outlet. Thus, in order to prevent *f* from being affected by this density change, inlet conditions were used for reference.

The Reynolds number was calculated as:

$$Re = \frac{\rho_{in} U_{in} D}{\mu_{in}} = \frac{4}{\pi D} \frac{\dot{m}}{\mu_{in}} \tag{3.3}$$

Based on viscosity at the inlet, the results fall into the Reynolds number range of 2×10^4 – 2×10^5 and are presented in Fig. 3.8. The measurements are compared to the friction coefficient values calculated from Colebrook correlation

$$\frac{1}{\sqrt{f}} = -2.0 \log\left(\frac{\varepsilon}{3.7D} + \frac{2.51}{Re\sqrt{f}}\right) \tag{3.4}$$

The roughness suggested in the literature for seamless stainless steel pipes is ε = 0.042 mm. For comparison, *f* values corresponding to 0.020 mm and 0.070 mm roughness are presented as well.

In these equations, density and viscosity values were acquired from the data of Fig. 1.1. Uncertainty values for *f* were calculated based on accuracy of the measurement devices for $\dot{m}$ and ΔP (0.1% and 0.15%, respectively). At each point, the measurements (P, T, ΔP, $\dot{m}$) were averaged over an approximately-0.5-second window (approximately 50 samples) resulting in 0.02% sampling error for ΔP and $\dot{m}$ measurements. The sampling errors for pressure (P_{in}) and temperature measurements were approximately 0.1% and 0.1°C respectively. The uncertainty of density was then approximated from the sensitivity of density to pressure and temperature ($(\partial\rho/\partial P)_T$ and $(\partial\rho/\partial T)_P$) combined with accuracy of

pressure and temperature measurements (±0.5 bar and ±0.5°C). The resulting uncertainty in f ranges from 1% to 23% with average and median both being equal to 7%. As shown in Fig. 3.8, there is some scatter in the data, however 78% of measured friction coefficient values are within ±20% of the predicted values from Colebrook equation for ε = 0.042 mm. Also, based on Reynolds number and the measured friction coefficient, the flow regime for most cases is in transition and very close to the fully turbulent regime. There are however four data points that deviate substantially from the Colebrook correlation values. They are at 80 bar and 78 bar, and have friction factor ranging from 0.08 to 0.10, compared to the ~0.05 value from the Colebrook correlation. There is no clear explanation for this behavior. One common feature between all three data points is that they have relatively large densities, ranging from 586 kg/m^3 to 709 kg/m^3. They may have resulted from an overestimation of ρ_{in} caused by erroneous pressure and temperature readings. It must be clarified that the error cannot be solely attributed to the large density value, as other data points with similar density values do not present this behavior.

In my view, this is a remarkable conclusion. Practically, it shows that despite the complicated nature of the near-critical flow, which is further investigated with visualization experiments below, the Moody diagram can be used with acceptable accuracy for the purpose of hydraulic design of near-critical CO_2 flows, provided that friction factor and Reynolds number are defined as per equations 3.13.3 and 3.3, respectively. The raw data in terms of pressure loss per unit length as a function of flow rate can indeed be very sensitive to the temperature of the near-critical fluid. This is because of the high sensitivity of density and viscosity on temperature (under constant pressure) that is shown in Fig. 1.1. However, when the results are presented in terms of appropriate non-dimensional quantities, these sensitivities cancel each other to a very significant extent and the Moody chart can be used as an instrumental design tool. It is very interesting that a similar behavior has been reported for heat transfer in supercritical CO_2 by Kurganov et al. [58]. They concluded that despite the significant changes in thermophysical properties in the fluid, heat transfer from the pipe flow was similar to the classical case of a flow with constant fluid

properties, when the appropriate non-dimensional quantities were considered. As a result, simple models were applicable to heat transfer rate calculations.

3.2 Pipe flow shadowgraph visualizations

Figure 3.9 shows shadowgraphs of the flow structure at six different stations during the flow across the optically accessible pipe starting from a state at supercritical pressure and subcritical temperature to a two-phase subcritical state.

The evolution of inlet pressure and temperature are presented on a P–T diagram along with the saturation curve in Fig. 3.10. It is reminded that shadowgraph provides the integral of the two-dimensional Laplacian of the refractive index in planes perpendicular to the line of sight along this line of sight [90]. Figure 3.11 shows refractive index of CO_2 at a constant temperature of 25°C along with saturated liquid and saturated vapor as a function of pressure. It is noted that once the two phases separate (i.e. slightly below the critical point) they have substantially different refractive indices, which is expected to yield refraction phenomena at the interface between the two phases.

During the tube flow, CO_2 initially is at supercritical pressure and subcritical temperature. In panel 1, where CO_2 is at a supercritical state, the shadowgraph lacks any clear structure and the small contrast can be attributed to small variations of the refractive index along the line of sight. The same is also true about the shadowgraph in panel 2. As shown in Fig. 3.10, as the fluid expands and flows through the test section, pressure decreases along with temperature until it dips below the critical pressure, then the temperature rises rapidly at approximately constant pressure until it reaches the saturation temperature. As fluid reaches the saturation curve, in panel 3 two distinct phases appear and create cell-like structures in the flow. Due to the different refractive index (which is a reflection of differences in density) between the two phases, the interface between them appears as bright lines in the

shadowgraphs. Consequently, the density mismatch of the two phases leads to a buoyancy-driven separation of them in panel 4. The fluids above and below the interface have distinct structures. At the bottom, the denser liquid phase has features similar to the shadowgraph in panel 3. At the top, the structure of the lighter vapor phase resembles that of the fluid in panels 1 and 2. This interface travels in the direction of the flow from top to bottom until it moves out of the field of view in panel 6. At this point, the fluid structure resembles that of the supercritical phase (#1 and #2). It indicates that the density is relatively uniform within this vapor phase.

This structure that comprises either one single phase-flow or two single-phase flows that are separated by a clear interface likely justifies the fact that pressure drop can be predicted from the Moody chart with reasonable accuracy. If buoyancy can generate phase separation (as it is reasonable to expect for pipes used for underground CO_2 storage), the flow behaves like the single-phase flow for which the Moody chart has been constructed.

In addition, it should be noted that for the two-phase flow of panels 3–6, the values of P and T are expected to follow the saturation line of Fig. 3.10. However the locus of P and T after crossing the saturation line is actually parallel to this line with a slight offset of approximately 0.5°C. This deviation can be attributed to the combined mild effect of impurities in the CO_2 stream from nitrogen and traces of lubricating oil from the accumulator, as well as to non-equilibrium phenomena in the expanding flow. We consider the 0.5°C offset acceptable error that does not alter the substance of our conclusions.

3.3 Throttling experiments

The significance of Joule-Thomson cooling in CCS processes has been highlighted in [91] and it lies in that CO_2 can expand after injection into depleted oil and gas fields thus causing a temperature drop and subsequently residual water freezing and/or hydrate formation in the rock. These in turn can

reduce the permeability of the geological formations (and therefore their capability to store CO_2) and cause fracture because of thermal stresses.

In order to study the effect of throttling from near-critical conditions, we measured pressure and temperature before and after an orifice and approximated the Joule-Thomson coefficient as:

$$\mu_{JT} \equiv \left(\frac{\partial T}{\partial P}\right)_h \approx \frac{T_{in} - T_{out}}{P_{in} - P_{out}} \tag{3.5}$$

Figure 3.12 shows the inlet and outlet data points on a pressure-enthalpy (*P*–*h*) diagram. Outlet data points are plotted assuming negligible change in kinetic energy across the orifice and thus:

$$h_{in} = h_{out} \tag{3.6}$$

The assumption of negligible kinetic energy can be supported by arguments similar to the ones that support the approximation of equations *3.1* and 3.2. In particular, since the flow speeds under consideration are on the order of a few m/s, the change in flow speed will generate changes in kinetic energy on the order of maximum 100 J/kg or 0.1 kJ/kg. It can be seen from the *P*–*h* diagram of Fig. 3.12 that such small enthalpy differences do not substantially affect the properties of the mixture, so the Joule-Thompson coefficient could be accurately formulated neglecting the kinetic energy terms.

As shown in Fig. 3.12, the fluid at the orifice exit expectedly fell under the bell-shaped *P*–*h* saturation curve, i.e. in the two-phase regime. Despite this, the measured pressure and temperature at the orifice exit do not coincide with the *P*–*T* saturation line, as shown in Fig. 3.13. This discrepancy can be attributed to the same factors mentioned in the previous section: presence of impurities and non-equilibrium effects. The only difference is that due to the flow configuration and its rapid expansion in the orifice, the non-equilibrium effect is probably stronger in this case.

In Fig. 3.14, Joule-Thomson coefficient measurements have been compared with values reported in NIST database [14]. The measurements follow the same trend as the NIST values, however there are some noticeable differences, especially in the lower enthalpy region. If presented as a function of inlet enthalpy, the relative error of these measurements with respect to NIST data, demonstrates an almost

bimodal behavior (see Fig. 3.15). For certain inlet conditions, the error is less than ~25% while for different conditions it reaches 200%. One possible controlling factor appears to be the inlet enthalpy, h_{in}. As shown in Fig. 3.15, the relative error starts rising for enthalpy values smaller than 335 kJ/kg, which is very closely the enthalpy of CO_2 at its critical point (h_{crit} = 332.25 kJ/kg). For data points with $h_{in} > h_{crit}$, the error magnitude is less than 25% for almost all cases, while for data points with $h_{in} < h_{crit}$ the error is significantly larger.

There are several factors that can contribute to this discrepancy. First, the Joule-Thomson coefficient data in the NIST database is obtained using an equation of state developed by Span and Wagner [18] specifically for CO_2. In the process of developing that equation, experimental Joule-Thomson coefficient data from [92] were only used in a manner that played a minor role in the curve-fitting process that established this empirical equation of state. As a result, as stated by Span and Wagner in [18], experimental Joule-Thompson throttling data had a "fairly small" impact on the optimization of the parameters of their model and thus, the model is not expected to provide accurate Joule-Thompson coefficient predictions. Furthermore, the experimental data of Bender et al. [92] spanned inlet temperatures 233-473 K and inlet pressures 0.1-1.5 MPa, i.e. conditions very far from the critical point. As a result, the model that underlies the NIST data is not reliable in the near-critical region. Table 3.1 presents a comparison with the only previous measurements that were in the vicinity of the critical point (the very early ones by Burnett [93]) that supports this assertion. Table 3.2 compares measurements from current work with NIST values and the early results of Burnett [93]. The comparison of the two sets of experimental data is performed at the closest conditions but not at exactly the same pressure and temperature. In first three cases, Joule-Thomson coefficient values from the three sources are in good agreement, the NIST data are much closer to the measurements of Burnett. This is attributed to the fact that those previous experiments [92]–[95] were performed using a porous plug as the throttling element as opposed to an orifice which is used in this study. Due to different evolution of the flow in the porous

plug compared to the orifice, the non-equilibrium effects were almost non-existent in those measurements. On the other hand, the greater pressure drop across the orifice (current orifice) compared to the porous plug (previous studies) enhanced the non-equilibrium effects. For instance, the pressure drop (ΔP) in previous studies was approximately 5-20 bar, in our study it ranged 13-70 bar. This generated a substantial deviation from the *differential* pressure drops required by the definition of Eq. 3.5. The definition of the Joule-Thompson coefficient involves differential cooling for differential pressure drop. Our measurements report finite temperature drops for the substantial pressure differences that will be involved in CCS. Nevertheless, it has to be pointed out that despite this difference and the non-equilibrium effects involved, the measured values of the Joule-Thomson coefficient agree with the results of NIST modeling both in terms of value of the coefficient (on the order of 0.5ºC/bar) and in terms of dependence of this value on inlet enthalpy.

3.4 Figures and tables

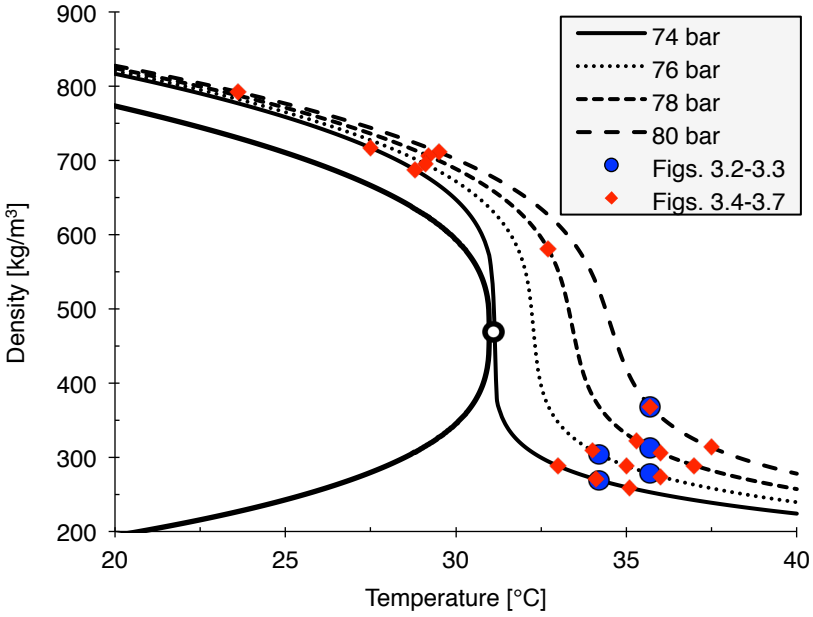

Figure 3.1 – Inlet conditions on the Density–Temperature diagram

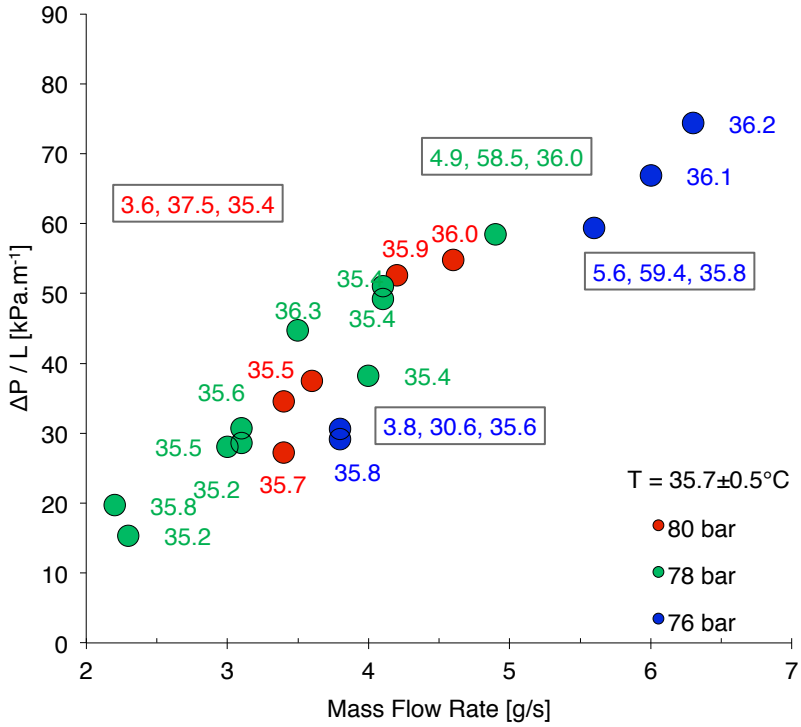

Figure 3.2 – Pressure drop per unit pipe length vs. mass flow rate at 35.7°C

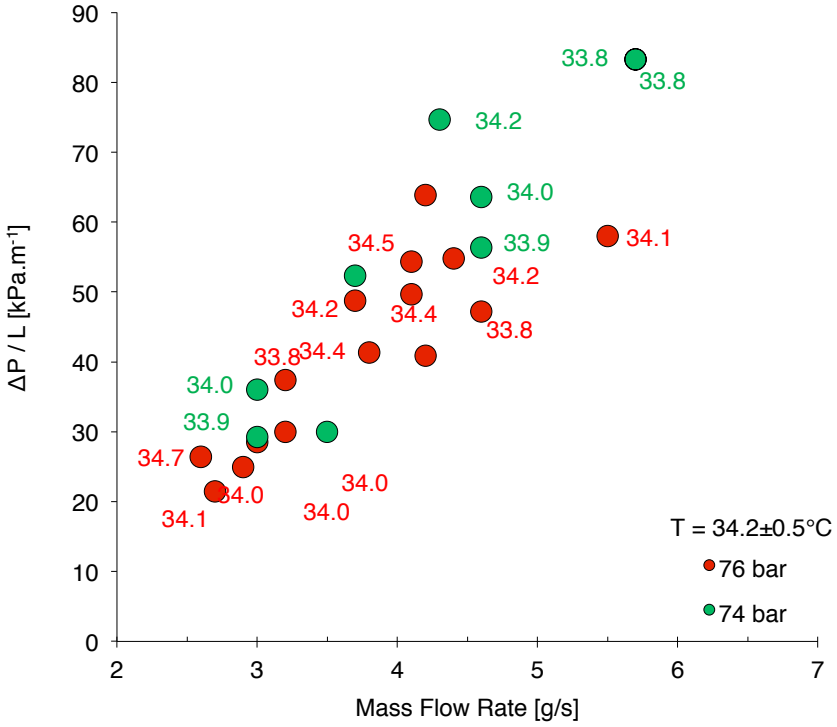

Figure 3.3 – Pressure drop per unit pipe length vs. mass flow rate at 34.2°C

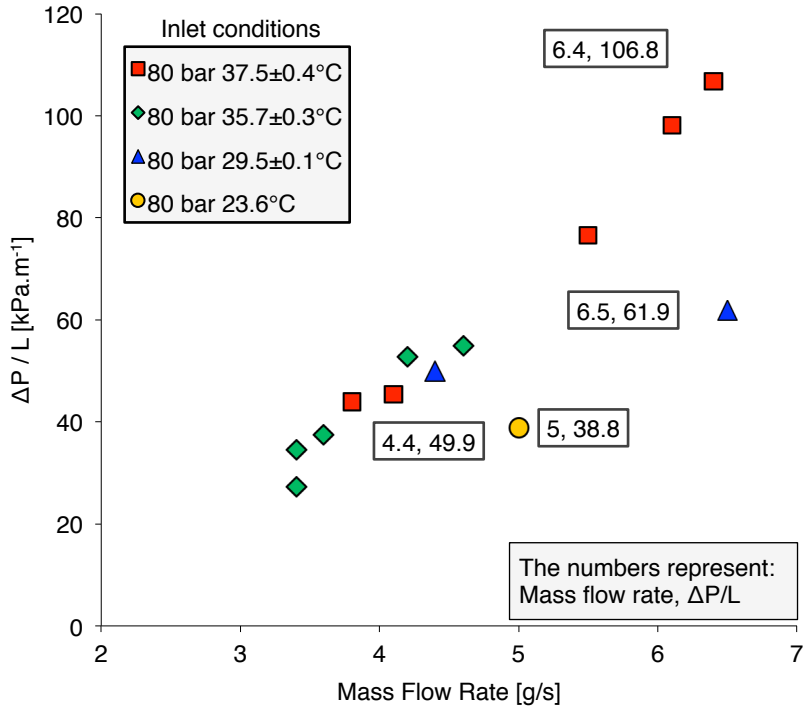

Figure 3.4 – Pressure drop per unit pipe length vs. mass flow rate at 80 bar

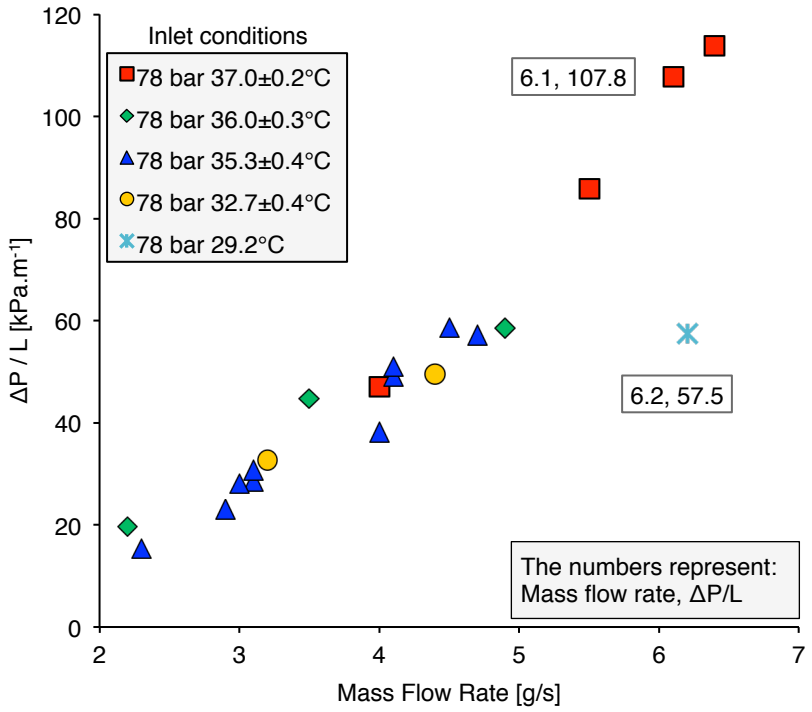

Figure 3.5 –Pressure drop per unit pipe length vs. mass flow rate at 78 bar

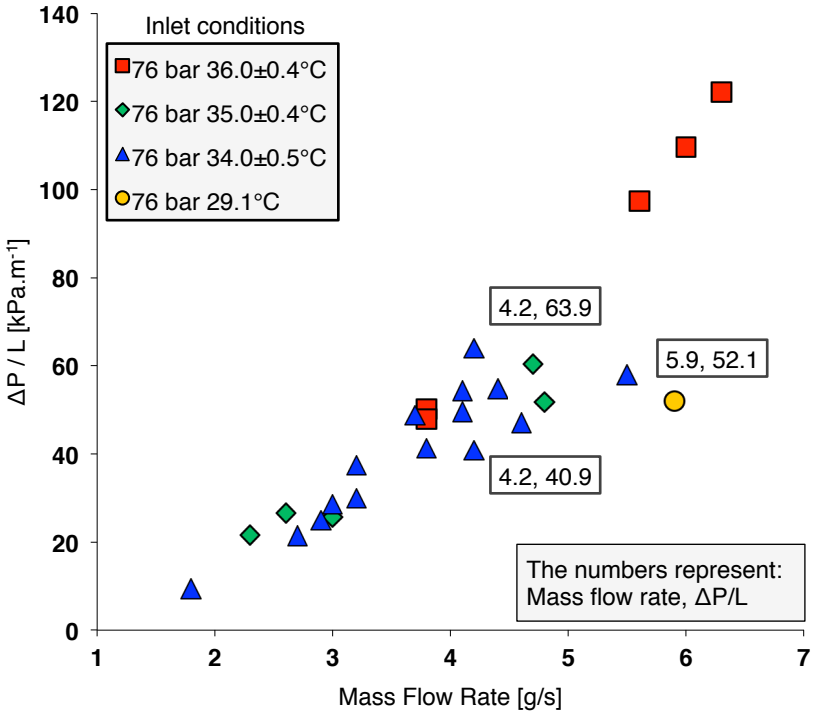

Figure 3.6 – Pressure drop per unit pipe length vs. mass flow rate at 76 bar

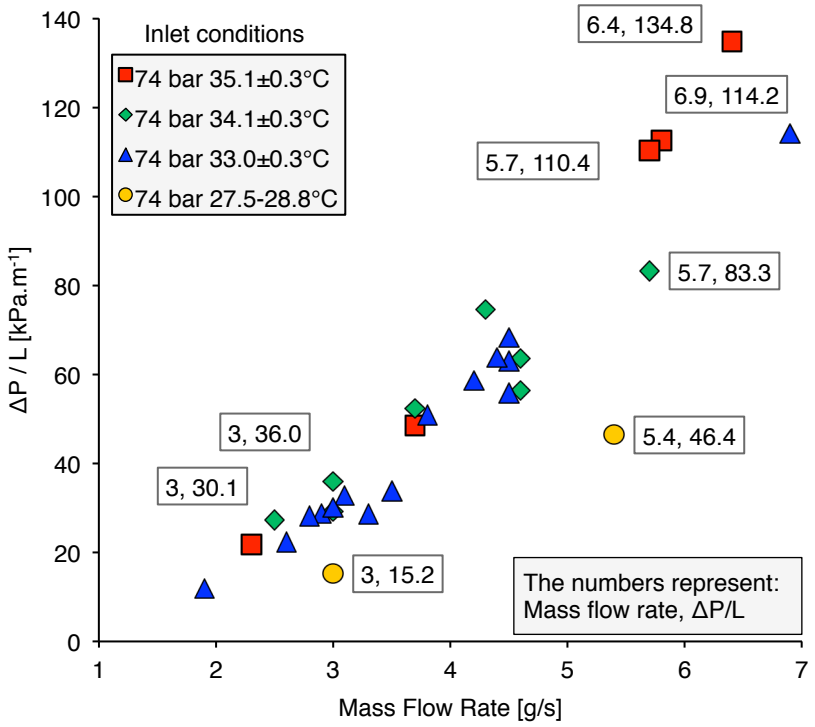

Figure 3.7 –Pressure drop per unit pipe length vs. mass flow rate at 74 bar

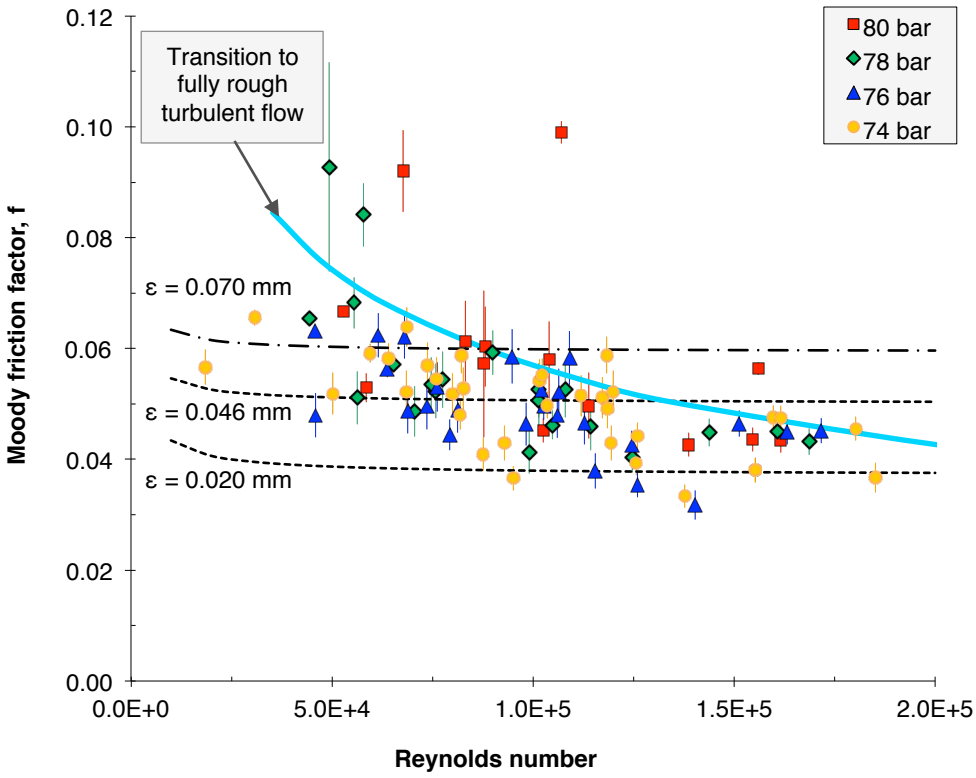

Figure 3.8 – Moody friction factor

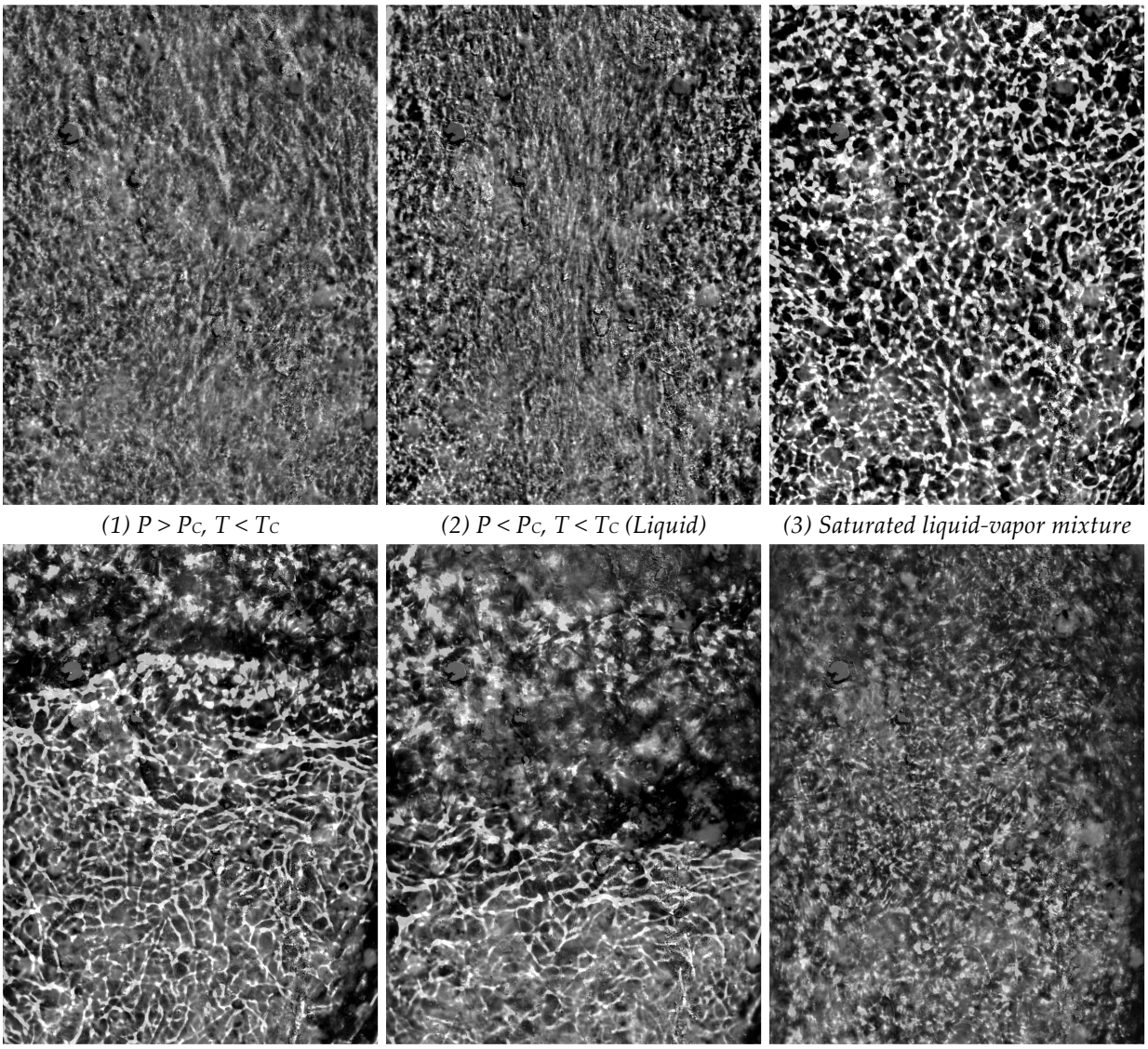

(1) $P > P_C$, $T < T_C$ *(2) $P < P_C$, $T < T_C$ (Liquid)* *(3) Saturated liquid-vapor mixture*

(4) Saturated liquid-vapor mixture *(5) Saturated liquid-vapor mixture* *(6) Liquid*

Figure 3.9 – Shadowgraphs of near-critical CO_2 flow, Flow direction from top to bottom

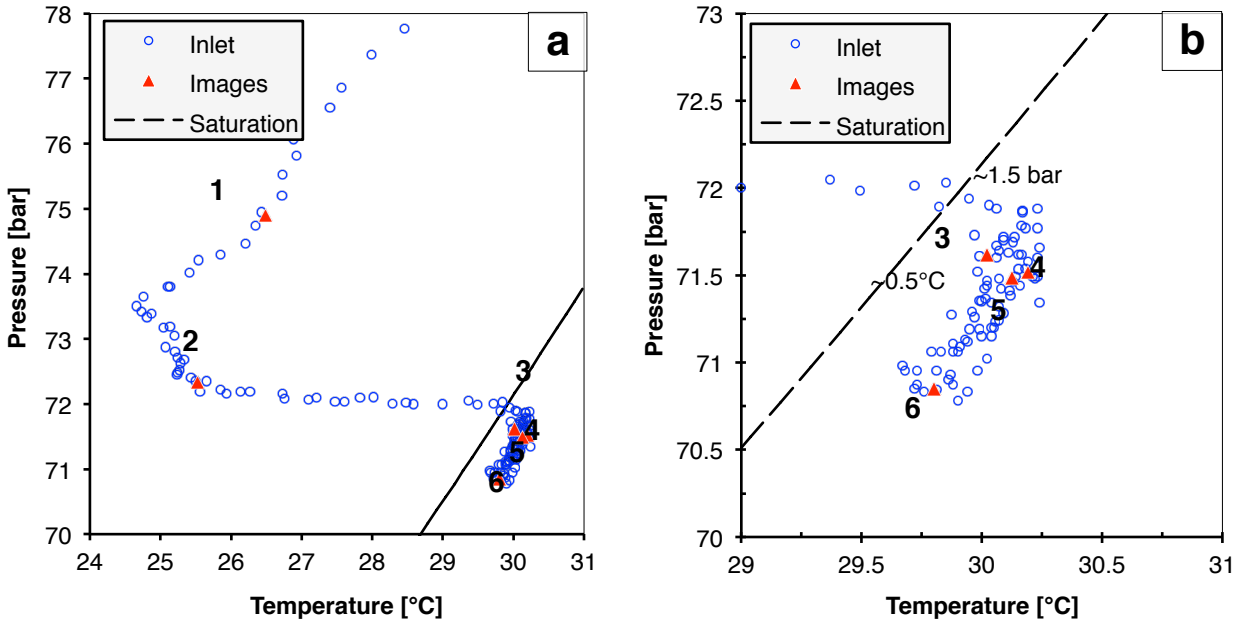

Figure 3.10 – P–T diagram for inlet conditions in shadowgraph experiment (a) Entire process (b) Zoomed-in view

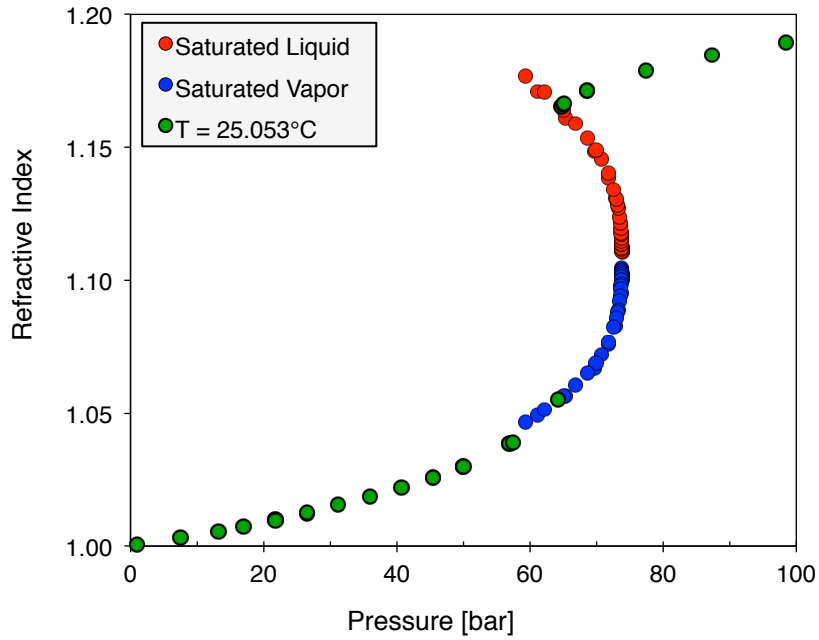

Figure 3.11 – Refractive index of Saturated Liquid & Saturated Vapor CO_2 as a function of temperature [96], [97]

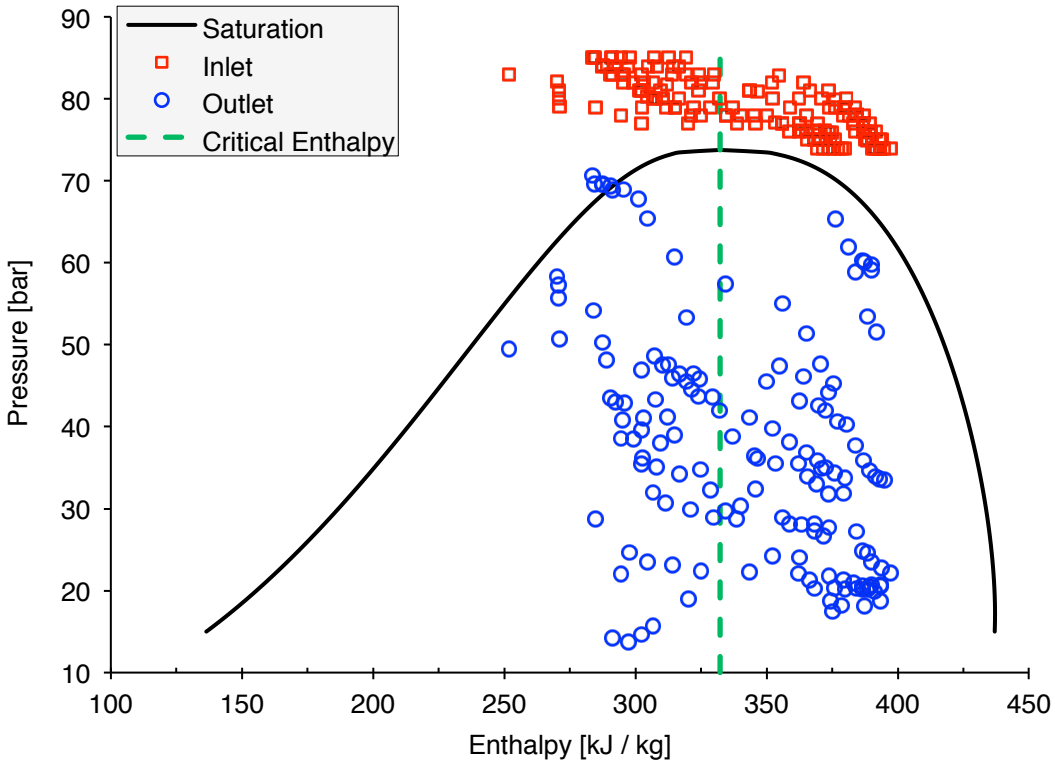

Figure 3.12 – Joule-Thomson experiment inlet and outlet conditions on a P-h diagram

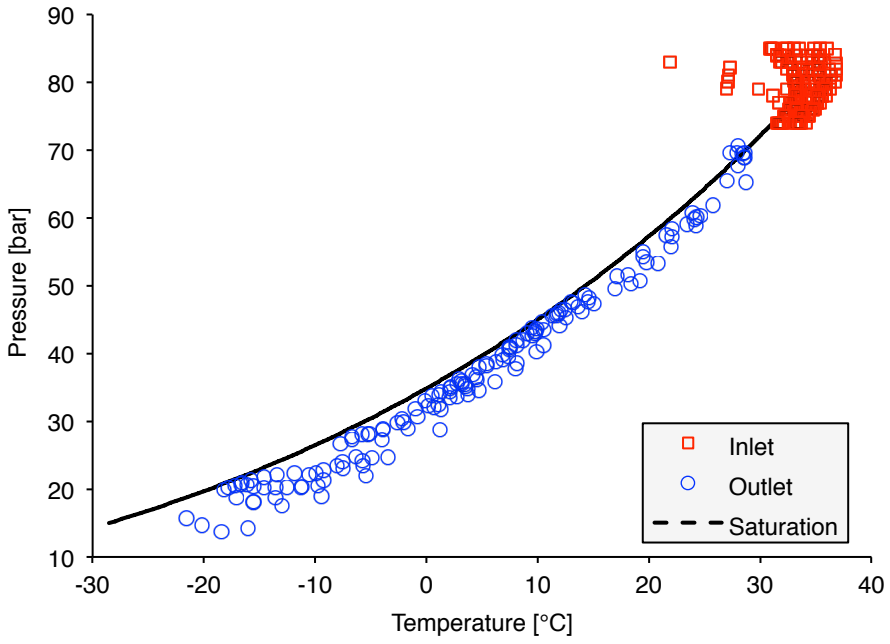

Figure 3.13 – Joule-Thomson throttling experiment P-T inlet and outlet data

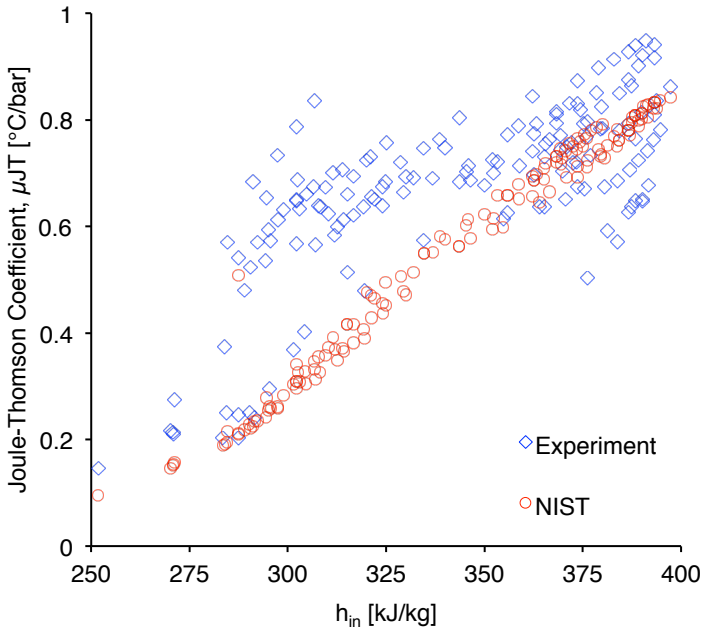

Figure 3.14 – Joule-Thomson coefficient measurements compared with NIST database values

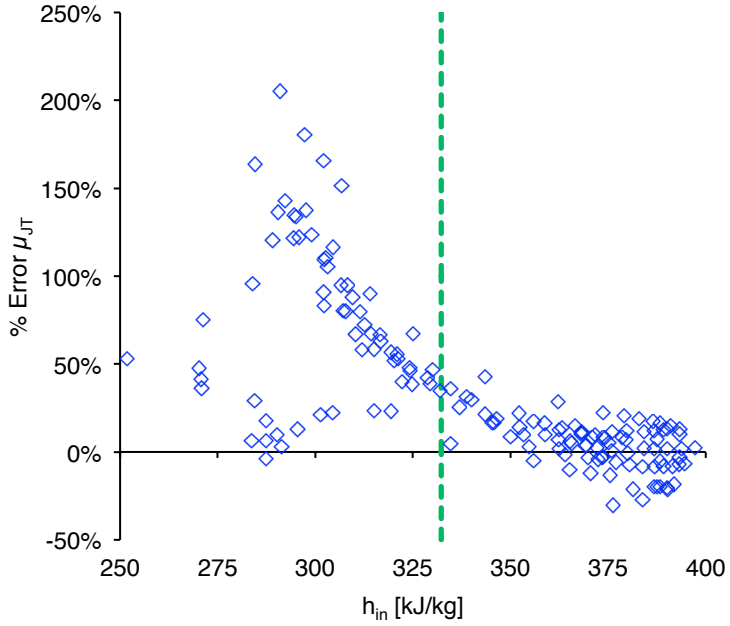

Figure 3.15 – Relative error in Joule-Thomson coefficient measurements with respect to the NIST database values

Table 3.1 – Comparison of the Joule-Thomson coefficient from NIST database with previous experimental data in the near-critical region

Pressure [bar]	**Temperature [°C]**	**Joule-Thomson Coefficient [°C/bar]**		**Relative error [%]**
		Burnett 1923 [93]	**NIST** [14]	
81.06	41.82	0.6415	0.7795	-17.7%
81.06	39.33	0.6358	0.7585	-16.2%
81.06	37.21	0.6098	0.7076	-13.8%
81.06	35.94	0.5649	0.6339	-10.9%
81.06	34.65	0.4412	0.4586	3.8%
81.06	32.77	0.3001	0.2944	1.9%
81.06	30.66	0.2299	0.2161	6.4%
81.06	28.26	0.1822	0.1661	9.7%
		Average		-5.6%
		Standard Deviation		9.9%

Table 3.2 – Comparison of the Joule-Thomson coefficient measurements with NIST database and previous experimental data in the near-critical region

Pressure [bar]	**Temperature [°C]**	**Joule-Thomson coefficient [°C/bar]**			**Temperature for Burnett data [°C]**
		Current study	**NIST** [14]	**Burnett** [93]	
74	34.1	0.862	0.842	0.8310	34.4
74	31.5	0.771	0.746	0.7169	31.4
74	32.1	0.784	0.792	0.7461	32.4
81	34.6	0.675	0.456	0.4412	34.7
81	32.9	0.368	0.304	0.3001	32.8

4. Multi-phase flow of CO_2 and water in porous micro-models

In this chapter the results from experiments in the two-dimensional porous micro-models that were described in section 2.2 are presented. These experiments involved visualizing the two phases using fluorescent microscopy and obtaining the velocity field by applying the micro-PIV technique. As stated in chapter 2, these are micro-fabricated structures that are meant to mimic (albeit to a simple, first-order approximation) geological formations. The chapter consists of several sections that address the physical phenomena observed in drainage experiments where liquid/supercritical CO_2 displaces water.

4.1 Displacement of water by CO_2 during drainage

Figure 4.1 presents a schematic of the field of view from a drainage experiment wherein a water-saturated micro-model is infiltrated with CO_2, which thus displaces the resident water. In order to maintain steady flow boundary conditions, two pumps were operated simultaneously, as shown in the experimental apparatus of Fig. 2.3. The CO_2 pump was connected to the inlet of the micro-model and was used to push the fluid while the water pump was connected to the outlet and was used to withdraw fluid. Experiments were conducted maintaining a flow rate of 0.005 ml/min at supercritical pressure and temperature of 80 bar and 40°C. Bulk velocity is defined as:

$$V_{bulk} = \frac{Q}{A\varphi} \tag{4.1}$$

In this equation, Q is the volumetric flow rate, A is the frontal area of the micro-model, and φ is the porosity. This flow condition corresponds to a bulk velocity of 0.4 mm/s, capillary number, Ca, of approximately 3.4×10^{-7} and viscosity ratio, M, of 0.03. As described in chapter 1, $Ca = \mu_2 V_2/\gamma \cos\theta$, and $M = \mu_2/\mu_1$ where μ is the dynamic viscosity, V is the bulk velocity, γ is the interfacial tension between the two fluids, and θ is the contact angle between the two fluids and the surface. The indices 1 and 2 refer to the resident phase (water) and the advancing phase (CO_2). The Reynolds number in water and CO_2 based on the bulk velocity and pore diameter is approximately 0.1 and 1.0, respectively. Based on the values of the capillary number and viscosity ratio in this experiment, and the log Ca – log M diagram of Zhang et al. [47] (Fig. 1.6), the flow regime is most likely capillary fingering. However, it should be noted that although the log Ca – log M diagrams for different porous media are qualitatively similar, the exact domains for each flow regime depends on the specific porous medium in consideration. Furthermore, since the field of view in the current experiments covers a limited area of the porous section, the fingering regime cannot be reliably determined from the pore-scale visualizations.

The recorded images cover three different stages of the flow: i) the steady flow of water before CO_2 enters the micro-model, ii) the passage of the CO_2 front and iii) the post-front-passage evolution. The region that was analyzed was located near the beginning of the porous section of the micro-model, next to the top sidewall as shown in Fig. 4.1, and bulk flow is from left to right. In the initial stage, when CO_2 has not yet reached the micro-model, the water velocity field in the micro-model appears to be steady, periodic, symmetric around the posts, and has minimal irregularities. Figure 4.2 shows the ensemble-averaged flow field (left) obtained from approximately 350 realizations and a sample instantaneous velocity field (right). The vector grid spacing is 32 × 32 pixels that translates to 21 μm vector spacing. All velocity fields shown in this chapter are under-sampled by a factor of 2 in x- and y-direction, unless otherwise stated. The maximum water velocity in the field expectedly occurs at the pore throats and has a magnitude of 1.6 mm/s (4 times the bulk velocity). The small differences noted between the instantaneous

velocity field and the ensemble-averaged field under these steady flow conditions, however, are larger than what would be expected from the velocity measurement uncertainty (~0.1-0.2 pixels corresponding to 0.01-0.02 mm/s) and the unsteadiness in the syringe pumps (the syringe pumps have a precision of 0.5% of the set flow rate). The RMS of the velocity fluctuations is approximately 15% of the ensemble-average velocity. We hypothesize that the fluctuations in velocity are caused by the instability of the travelling CO_2-water front, even before it has reached the micro-model. It must be reminded here that the constant flow rate and constant pressure conditions in the experiment were maintained by pumping both syringe pumps at equal flow rates, but in opposite directions; i.e. pump 1 (CO_2) pushing and pump 2 (water) receding (refer to Fig. 2.3). Thus, as the flow began, the interface between CO_2 and water traveled in the connecting tubes until it reached the micro-model and eventually appeared in the field of view. Considering the lower viscosity of CO_2 compared to water, the travelling CO_2 front will be unstable, and the instability may lead to flow perturbations being manifested as velocity fluctuations. Thus, the velocity fluctuations can be attributed to the specific configuration of the experimental apparatus and the inherent instability of travelling CO_2-water interface.

As CO_2 enters the micro-model and approaches the porous section, the water flow within the field of view accelerates, the velocity field becomes unsteady and the regularity in the flow field is disrupted. This sequence of events is illustrated in Fig. 4.3 by selecting representative frames from each stage of the entire sequence. In Fig. 4.3.A (frame 1), the velocity field in the water phase is uniform with a maximum velocity of approximately 1.8 mm/s. As time advances, the water velocity fluctuations (now larger in magnitude compared to the uncertainty in the velocity measurement apparent in Fig. 4.2) are strikingly apparent and, as Fig. 4.3.B (frame 18- there is a time interval of 100 ms between frames) depicts, the flow within the water phase accelerates to a peak velocity of approximately 4.3 mm/s in the pore throats and the flow field begins to lose its spatial regularity and periodicity. Shortly after onset of irregularity (0.7 s), CO_2 reaches the porous section and enters the field of view (Fig. 4.3.C -frame 25). At

this point, the maximum water velocity in the field has reached 5.0 mm/s occurring at the pore throats near the top of the micro-model as indicated by the red arrows.

The increased water velocity fluctuations and flow acceleration occurring prior to appearance of CO_2 in the field of view is attributed to flow instabilities associated with CO_2 entering the porous section at a location outside of the field of view. This behavior was observed in previous work [98] and was explained as the effect of local pressure perturbations induced by impulsive events (burst) at the fluid-fluid front. It is worth noting that the initial invasion of CO_2 was more likely to occur close to the top/bottom sidewalls of the micro-model rather than near the centerline. This was established from our experience in running numerous experiments.

The image sequence presented in Fig. 4.4 captures the CO_2 front traveling through the micro-model within the field of view (Fig. 4.1) of the porous section (consecutive images were acquired 0.1 s apart). This sequence consists of 15 consecutive particle image fields captured beginning from the moment CO_2 entered the field of view (Fig. 4.3.C – frame 25). Regions with fluorescent emission represent water, the solid elliptic pillars of the porous micro-model are demarcated in red and the infiltrating CO_2 is captured in the dark regions advecting left to right from frames 25 to 39. Selected velocity fields corresponding to images from this sequence are presented in Fig. 4.5. The most significant feature in this sequence is the overall deceleration of the water flow in time, occurring almost immediately after the appearance of CO_2. While the maximum water velocity in frame 25 (Fig. 4.3.C) is 5.0 mm/s, it decreases to 3.3 mm/s in frame 26 (Fig. 4.5.A) and 2.6 mm/s in frames 27 and 28 (not shown). Through the remainder of the sequence, the maximum remains at approximately 2.0 mm/s (Fig. 4.5.B–E), nearly comparable to the maximum water velocity of 1.6 mm/s noted under steady flow conditions (Fig. 4.2). This flow deceleration in the water phase and the relatively slow progress of the CO_2 front, comes as a surprise given the strong flow acceleration identified prior to arrival of the front (Fig. 4.3). At the end of this sequence (frame 39; 3.8 s relative to frame 1), CO_2 has reached the second column of the

elliptic pillars. Subsequently, the flow decelerates even further, the CO_2 front ceases moving, and the spatial distribution of the two fluids remains fixed in frames 40–64 (3.9-6.3 s relative to frame 1). During this period of relative stagnancy, the velocity is relatively small with the maximum velocity on the order of the bulk velocity (approximately $1/4^{th}$ the maximum velocity in the steady single-phase flow) as highlighted in Fig. 4.6, which presents the average water velocity field over this frame sequence. This stage highlights the onset of preferential flow paths being followed by the resident water as it is displaced by the continued infiltration of CO_2.

Following this period of relatively quiescent water velocity with no discernable change in the spatial distribution of the two fluids, the water flow field suddenly changes in magnitude accompanied by an abrupt change in the spatial distribution of the two fluids. During frames 65 to 68, CO_2 suddenly breaks through and establishes a preferential path through the water in the form of a finger. This event is depicted in Fig. 4.7 as a time sequence of PIV image pairs. Note that while the time interval between the PIV images pairs (i.e. images in the same row) is 6 ms, the interval between subsequent image pairs (i.e. along the column) is 100 ms, respectively. The water velocity fields corresponding to these images, derived from cross-correlation analysis of the time-delayed images in each row, are presented in Fig. 4.8. In frame 65 (Fig. 4.8.A), the maximum water velocity is only half that of the steady flow period (Fig. 4.2) and the velocity field is symmetric around the elliptic pillars again similar to the steady single-phase flow at the beginning of the sequence. In frame 66 (Fig. 4.8.B), CO_2 penetrates water in two separate branches (fingers), at the top one is marked with a red circle in Fig. 4.7. In frame 67 (Fig. 4.8.C), the penetration and growth of fingers continues with each finger branching into several more fingers. In frames 67A-B the growth of one of the fingers within the 6 ms time interval is captured (see Fig. 4.7, finger evolution is highlighted by red circles). This is one of the very few instances of such events being captured in the same PIV image pair. Capturing such an event was very elusive because in order for this to happen the time interval separating the two images of the PIV pair has to be much shorter than the characteristic time

scale for the advancement of the front between the two liquids in the pores. The water flow direction near the growing finger is marked with arrows in frame 67A of Fig. 4.7. Finally, the wetting nature of water in this flow through the presumably hydrophilic silicon micro-model is readily apparent from the thin water films noted along the circumferences of the elliptic pillars at the left of the images in Fig. 4.7. While CO_2 has clearly infiltrated this region of the micro-model, its non-wetting nature relative to silicon maintains these thin films of water along the elliptic pillars. These water films are discussed in greater detail in section 4.2.2.

Two conclusions can be drawn from the results of Fig. 4.7. First, the water velocity near the advancing meniscus is 8–10 mm/s, which is 20–25 times the bulk velocity and 5–6 times the maximum velocity for the steady single-phase flow. This local velocity thus corresponds to local Reynolds numbers of 2.5–3 in the water phase. Perhaps even more interesting is that the same high velocity magnitude is observed in the pore throat below the finger but in the opposite direction (i.e. reverse flow) as illustrated in Fig. 4.8.C. Immediately following this short time-scale, "bursting" event (< 0.3 s in duration), in frame 68 (Fig. 4.8.D), the velocity in almost the entire field of view drops to ~1 mm/s. The only region in the field with high velocity is near the bottom left corner of the image.

The velocity fields in Fig. 4.8 revealed, for the first time, the unsteady motions associated with the migration of CO_2 front occurring during displacement of water by supercritical CO_2 in a porous medium. The entire process from the initial appearance of CO_2 until the "burst", when CO_2 established a path through the porous medium, took less than 4.5 seconds. After this point and for the entire data acquisition period (approximately 1800 image pairs, equivalently 180 s), the spatial distribution of the two fluids within the field of view does not change appreciably in time. Nevertheless, the water phase is not entirely motionless. Figure 4.9 shows an example of the instantaneous velocity and vorticity fields in the water during this period of stagnant spatial fluid distribution following the passage of the CO_2 front. In addition to continued water flow through fixed regions of the porous micro-model (likely due to open

flow paths connected to regions outside the present field of view), the high values of vorticity allowed us to identify regions of shear-induced circulation near the fluid-fluid interface. Within these circulating flow regions, the velocity was very low (< 0.1 mm/s) and presented a fluctuating nature. The reason for this fluctuating motion remains unclear but we speculate that such fluctuations are caused by unsteady flow events occurring outside of the field of view. The shear-induced flow and the circulation zones will be revisited and discussed in greater depth in section 4.2.2.

4.1.1 Statistical analysis

This water velocity data can also be studied from a statistical point of view, by calculating the probability density function of velocity components over the entire domain. To that end, the same data ensemble discussed herein is reconsidered, but subdivided in three time periods that are based upon three observed flow regimes: steady single-phase, transient multi-phase, and steady multi-phase. Steady single-phase refers to the stage in which the water flow was steady and regular, as depicted in Fig. 4.2 (350 frames; not included in the numbering). The transient multi-phase stage corresponds to the short period of unsteady water flow prior to the appearance of CO_2 in the field of view, as well as during the period over which CO_2 fingers invade through the porous section (Figs. 4.3–4.8; frames 1–88). Finally, steady multi-phase refers to the period where the CO_2 front has moved out of the field of view and the spatial distribution of the two phases remains unchanged (Fig. 4.9; frames 100–1800). The ensemble size of these three groups is approximately 350, 90, and 1700, respectively.

The four panels in Fig. 4.10 show the probability density functions for the water velocity component in the bulk flow direction, u, the water velocity component normal to the bulk flow direction, v, the water velocity magnitude, $|V|$, and the water velocity vector angle with respect to the bulk flow direction, θ. For better illustration, zoomed-in views of PDF(u) and PDF(v) from Fig. 4.10 are presented in Fig. 4.11.

In the steady single-phase flow, the probability density function of u is expectedly asymmetric and for values of PDF greater than 10^{-2}, u ranges between 0.2 and 1.5 mm/s, with most probable value being very close to the bulk velocity at approximately 0.5 mm/s (PDF(u) value ~0.03). On the other hand, the PDF(v) is symmetric around $v = 0$ which stems from the symmetric geometry of the micro-model. The most probable value of v is zero with a probability density value of ~0.05. The symmetry of PDF(v) exists for both steady single-phase and steady multi-phase flow. However, for the single-phase flow the probability distribution of v is significantly broader compared to that of steady multi-phase flow.

In the steady multi-phase flow, u and v have nearly identical probability distributions. They are both symmetric around zero with a maximum probability greater than 0.9 at zero, indicating that the aqueous phase has very limited motion and is essentially stagnant. The maximum and minimum for both u and v is approximately equal to the bulk velocity.

The behavior for the transient multi-phase flow is entirely different if compared to the steady single- and multi-phase flows. The most noticeable characteristic is the wider range of values of u and v. Both velocity components have a range of approximately -10 mm/s to 10 mm/s, indicating an acceleration of water flow in the field of view. Also, both distributions for multi-phase flow have a most probable value of zero with a probability density value of 0.25 for u and 0.4 for v. Although both PDFs have a peak at zero, they are not symmetric about zero. For $|u| \lesssim 4$ mm/s, positive values of u are more probable than negative ones with an approximately one order of magnitude greater probability density value, mainly due to the bulk flow direction being in the positive x-direction. However, for $|u| \gtrsim 4$ mm/s, the negative and positive values of u become almost equally probable, with negative values even slightly more prevalent for 6 mm/s < $|u|$ < 8 mm/s. This behavior, particularly water flow *against* that of the bulk flow, suggests that flow events associated with large velocity magnitude may be driven by local pressure gradients rather than the large-scale pressure gradient sustaining the bulk flow. This may produce local upstream flow events that are more intense than downstream flow events. In a similar manner, v also has

a wide probability distribution in the transient multi-phase flow regime. For $|v| \lesssim 5$ mm/s, the negative values are slightly more probable than positive values, and for $|v| \gtrsim 5$ mm/s positive and negative have similar probability densities. The most probable cause for the lack of symmetry in v values is that the field of view is bound by the upper sidewall of the micro-model, thus negative v values are more likely to happen than positive values due to solid boundary effects. The interesting and, to some extent, unexpected point here is that, there is no preferential direction for large water velocity events, i.e. $|u|, |v| \gtrsim 5$ mm/s. This observation is consistent with the notion of Haines jumps [48], [50], [51] that invasion of the non-wetting phase to the pore spaces occurs through a series of velocity jumps rather than smooth continuous motion of the front. These velocity jumps have been associated with pressure bursts that generate pressure waves, which in turn result in sudden motion of both fluids in all directions. These results provide strong evidence for the significance of inertial effects in drainage dynamics as the maximum local *Re* in water goes to 3 compared to 0.5 in the steady single-phase flow. Moreover, assuming constant mass flux across the moving meniscus, the maximum local *Re* for CO_2, would reach 89 which is well beyond the limit of *Re* = 10 for the validity of Darcy's law.

The velocity magnitude PDF in Fig. 4.10C also signifies the wide dynamic range of the water velocity magnitude occurring in this flow system. The larger dynamic range is found in the transient multi-phase regime, suggesting that this stage is associated with significant flow instabilities. This wide range of velocities makes the measurements much more complicated and challenging to accomplish. In Fig. 4.10.D, the PDF of the velocity vector angle with respect to the bulk flow direction is presented. In the steady single-phase flow, the PDF is symmetric around $\theta = 0$, and the most probable values are $|\theta| \lesssim 30°$. These PDF characteristics are direct results of the specific geometry of the micro-model, with $\theta \approx \pm 30°$ corresponding to the flow between spanwise staggered spaces between the pillars. Also PDF($|\theta| > 90°$) < 10^{-5} indicates that there is no water flow opposing that of the bulk flow. On the other hand, for the steady multi-phase flow, the PDF is nearly flat for all θ values, indicating that velocity vectors do not have a

preferential direction. This is consistent with the shear-induced circulation zones observed near fluid-fluid interfaces, mentioned earlier in this section (Fig. 4.9) and will be discussed later in section 4.2.2. Nevertheless, the PDF has local maxima near 0° and ±180°, which is reflective of the geometry of the micro-model (specifically the elongated shape of the pillars in the horizontal direction) and the spatial distribution of the two fluids under this flow regime of steady multi-phase flow. In the transient multi-phase flow regime, PDF(θ) has a shape very similar to that of steady single-phase flow for $|\theta| \lesssim 45°$; however the transient flow has a much higher probability density for $45° < |\theta| < 180°$ compared to the steady single-phase flow. This stark difference for large angles reflects the clear propensity for the water to flow in a direction counter to that of the bulk flow. Another interesting fact is that PDF(θ = +90°) > PDF(θ = -90°) for transient multi-phase flow, which means that water flow in the upward direction is more likely than water flow in the downward direction. This is unexpected given that the field of view is located directly below the upper boundary of the micro-model. However, upon further inspection it is realized that such behavior can be explained from Fig. 4.6, which shows velocity vectors mostly in the upward direction in the pore spaces.

It must be pointed out that the tails of the PDF for velocity vector components in the transient multi-phase flow (Fig. 4.10.A–C) have much smaller probability value compared to other regions. The reason is that the high-velocity events in the flow, which are represented by the tails, have a relatively small sample size. The small sample size is a result of having few Haines jump events in the ensemble, which in turn is a consequence of low temporal resolution. Considering the data ensemble for this flow stage, the sampling error for the PDF is 1.6×10^{-6}. As shown in Fig. 4.12, although this uncertainty becomes more significant near the tails of the PDF, it remains with acceptable limits.

4.2 Underlying physics

4.2.1 Capillary pressure and interfacial curvature

As explained in chapter 1, capillary pressure is a local variable that is a function of interfacial curvature and interfacial tension, as described by the Young-Laplace equation:

$$P_c = 2\gamma K \tag{4.2}$$

In this equation, P_c is the capillary pressure, γ is the interfacial tension, and K is mean curvature. Capillary pressure is an important quantity in multi-phase immiscible flow in porous media because the displacement mechanism is largely dependent on this quantity. For example, the accepted mechanism for pore drainage is that in order for the non-wetting fluid to move to a downstream pore it must overcome a threshold capillary pressure set by the radius of the pore entrance [46], [99]. Combining capillary pressure data with velocity field data can provide a powerful tool for understanding the flow dynamics underlying the interesting observations presented earlier.

In the two-dimensional micro-model, the Young-Laplace equation becomes [50]:

$$P_c = \gamma\left(\frac{1}{R_1} + \frac{2\cos\theta}{d}\right) \tag{4.3}$$

where γ is the interfacial tension (IFT), R_1 is the radius of curvature in the 2D plane of the flow measured from the collected images, θ is the contact angle between water and CO_2 in the silicon micro-model, and d is the micro-model depth.

In Fig. 4.13, a sequence of raw PIV images and their corresponding velocity fields are presented that depict the displacement of water by CO_2. This data is from a different experiment than the one presented in Figs. 4.2–4.11. The reason for choosing this particular data set for capillary pressure analysis is that dyed CO_2 and tracer particles are visible in the image and allows for more accurate identification of the fluid-fluid interface. This data is from a drainage experiment with a flow rate of 0.05 ml/min (bulk

velocity: 4 mm/s) at supercritical pressure of 80 bar and subcritical temperature of 24°C. This corresponds to a capillary number, Ca, of 9.8×10^{-6} and viscosity ratio, M, of 0.08. The direction of bulk flow in these images is from right to left and some of the menisci imaged in Fig. 4.13 are considered and labeled. The radii of curvature, R_1 from Eq. 4.3, of these select menisci are reported in the images. In addition, Table 4.1 presents the corresponding capillary pressure for each meniscus, obtained using Eq. 4.3. The values used in this equation are: $d = 30 \pm 1$ μm, $\gamma = 30$ mN/m ± 3.5%. (obtained from Bachu and Bennion [27]) and $\theta = 15.3 \pm 1.9°$ (obtained from Zhang et al. [65]). Here, R_1 was measured by manually selecting points on individual menisci and fitting a circle to those points using the Taubin algorithm [100]. A conservative estimate for the uncertainty of this technique for determining the radius of curvature is ±10% largely due to the fact that the interfaces are not very sharp and have a width of approximately 5–10 pixels (thus the measured curvature is affected by the user's choice of points). Thus, the uncertainty in capillary pressure obtained from error propagation analysis is approximately 20%.

Studying the evolution of the menisci in the sequence of images and the associated velocity fields reveals several interesting phenomena. A first observation is that in general, the growing branch of CO_2 has the meniscus with the smallest radius of curvature (with meniscus A being a possible exception). This is expected because during drainage, the non-wetting fluid displaces the wetting fluid in the pores. For this displacement to occur, the capillary pressure must exceed a pressure threshold that is determined by the radius of the pore entrance (pore throat), a_t. According to the Young-Laplace equation (Eq. 4.2) this threshold is given as:

$$P_t = \frac{2\gamma \cos\theta}{a_t} \tag{4.4}$$

Using the values given above for γ and θ, and applying $a_t = 51$ μm, Eq. 4.4 yields $P_t = 1136$ Pa.

The smaller the radius of the curvature, the higher the chance of overcoming this threshold. This behavior can be verified by comparing the curvature of the same meniscus in two consecutive images. For example comparing menisci A–F in frames 1 and 2 of Fig. 4.13 indicates that the advancing menisci

(A, C, D, F), have a smaller radius of curvature in frame 2 than in frame 1. On the other hand, the receding meniscus (B) has a larger radius of curvature in frame 2 compared to 1. For meniscus E, the curvature remains unchanged. It is worth noting that during a drainage event, the curvature of a moving meniscus changes which leads to concomitant changes in the capillary pressure. As reported by Armstrong and Berg [50], the capillary pressure decreases after the fluid-fluid interface reaches its maximum velocity. Thus, after the burst event, which is accompanied by the maximum interfacial velocity, the radius of curvature of the meniscus increases. In the data presented herein, due to the relatively large time interval between the images, the variations of curvature with time cannot be fully resolved. Nevertheless, the images do provide supporting evidence of this phenomenon. In Fig. 4.13 frames 5–7, R_1 for meniscus D goes from 48 μm in frame 5, to 97 μm in frame 6, and 43 μm in frame 7. The increase in R_1 occurs despite the fact that meniscus D is moving. This suggests that in frame 6, meniscus D is at the post-burst stage for which the capillary pressure decreases and the radius of curvature increases. The corresponding burst events are the ones that allow menisci H and K to advance.

Another interesting observation is that the growth direction of CO_2 fingers follows the high-momentum pathways defined as high-velocity flow paths of water in the porous medium that appear to form downstream of the fluid-fluid front. In Fig. 4.13, the high-momentum pathways, marked in each frame with arrows, indicate the direction of growth of the finger in the consequent frame. For example, in frame 2, the high momentum path ahead of meniscus D demarcates the direction where the finger will grow in frame 3. In frame 3, the high momentum pathway ahead of meniscus D splits into two branches, and it is very interesting that in frame 4 CO_2 has also split into two branches following along the high momentum pathway of frame 3. Also, comparing frames 4 and 5 shows that meniscus I in frame 4 follows the high momentum pathway and splits into two branches. Another feature that can be identified in these images is that, as reported by Armstrong and Berg [50], the pore drainage dynamics are nonlocal, in the sense that events occurring in nearby pores are connected (This notion is counter to that embodied

in pore-scale models employed in numerical simulations for which correlation of flow events in adjacent pores in a local pore neighborhood is typically neglected [101][ref??]). For example, penetration of the non-wetting phase into a specific pore may be accompanied by a meniscus retraction in another adjacent pore. This is illustrated in Fig. 4.13 where in frames 4-7, as CO_2 displaces water and the fingers grow to the left, meniscus A gradually retreats from its pore space. It is worth noting that the retraction of this particular meniscus occurs in spite of the high-momentum pathway right above it. However, since this meniscus is near the edge of the image, and the events occurring in its surrounding pores are not visible, no conclusion can be made regarding the effect of the high momentum pathway on this particular meniscus retraction.

4.2.2 Shear-induced circulation zones

Figures 4.14 and 4.15 present data from a separate drainage experiment at a flow rate of 0.05 ml/min (bulk velocity: 4.2 mm/s) at supercritical pressure of 80 bar and subcritical temperature of 24°C. The bulk flow direction is from left to right and the micro-model orientation is rotated 90 degrees relative to that presented in the previous discussion and Figs. 4.2–4.13 (major axis of elliptic pillars now normal to the bulk flow direction). This flow condition corresponds to a capillary number, *Ca*, of approximately 9.8×10^{-6} and viscosity ratio, *M*, of 0.08. The Reynolds number in water and CO_2 based on the bulk velocity and pore diameter is approximately 0.9 and 9.6, respectively. As indicated earlier in chapter 1, due to the viscosity ratio of water (wetting phase) and CO_2 (non-wetting phase), displacement of water by CO_2 in a porous medium occurs through penetration and growth of dendritic features called fingers. This results in disconnected patches of water and CO_2 within the domain that can be either mobile or immobile. In Fig. 4.14 a raw PIV image is presented which shows the distribution of the CO_2-rich phase (dark regions) and the aqueous phase (the regions with bright particles) after the CO_2 front has passed.

One of the features noticeable in Fig. 4.14 is the thin water film covering the circumference of the elliptic pillars of the silicon micro-model. This observation confirms that the micro-model is indeed hydrophilic (water-wet). When the raw PIV images are viewed in sequence, the motion of the tracer particles within these water films is easily perceptible. This motion is induced by shear from CO_2 flow, which is also the underlying cause for the circulation zones observed near the fluid-fluid interfaces in trapped water ganglia. This slow circulation is clearly evident when images are viewed in sequence and can be quantified by computing the vorticity maps associated with the velocity fields. Such distributions are illustrated in Fig. 4.15 by the ensemble-averaged (50 realizations) velocity vector field and the overlaid vorticity contours. Positive and negative vorticity denote counterclockwise and clockwise rotation, respectively.

In comparison to Fig. 4.9, the noted shear-induced circulation zones in Fig. 4.15 are stronger which is primarily due to the higher flow rate (In Fig. 4.15, the flow rate is 0.05 ml/min while it is 0.005 ml/min in Fig. 4.9). In addition, since the micro-models for these two cases are geometrically different, the flow patterns will be different as well. Another potentially contributing factor is the viscosity ratio. The temperature in Fig. 4.15 and Fig. 4.9 is 24°C and 40°C, respectively. Temperature increase from 24°C to 40°C results in the viscosity ratio of CO_2 to water changing from 0.08 to 0.03. As a consequence, the shear-induced velocity gradient in water should also change. It is worth noting that, the reason for running experiments at two different temperatures (24°C and 40°C) was to study the difference in flow behavior under subcritical and supercritical CO_2 temperatures. However, the collected data was deemed insufficient for drawing any conclusions about the effects of temperature, and thus this matter is not discussed any further.

Based on the direction of circulation inferred from water vorticity in Fig. 4.15, the direction of the CO_2 velocity adjacent to the menisci can be determined despite not being quantitatively tracked in this experiment. In the regions highlighted with red rectangles in Fig. 4.15, the flow direction near the fluid-

fluid interfaces is marked with blue arrows. In the left rectangle, the vorticity has opposite signs across the CO_2 stream, indicating that CO_2 velocity is consistently from left to right (see the arrows) in the vicinity of these menisci. In the right rectangle, the CO_2 flow direction inferred from the direction of circulation in water suggests that CO_2 velocity has opposite directions across a single flow pathway. This is a remarkable observation, implying that there are two CO_2 streams flowing in *opposite* directions within a single flow pathway defined by the geometry of the elliptic pillars combined with the flow restrictions imposed on CO_2 by trapped (i.e., immobile) water ganglia.

Both the observation of thin flowing water films along the elliptic posts and the occurrence of circulation zones that highlight unique CO_2 flow pathways owing to pore geometry and trapped water ganglia are being reported here for the first time. The observation of these flow features was made possible by the application of the micro-PIV technique that allows one to distinguish between active and passive flow pathways, which refer to moving and stagnant regions in water, respectively. In this case, it was observed that even the trapped water ganglia are not completely stagnant as there are circulation zones near the fluid-fluid interfaces. In addition, although velocity in CO_2 was not measured due to technical obstacles for seeding of this fluid phase, valuable information about CO_2 flow can be inferred from water velocity data.

The existence of the aforementioned circulation zones in water can have strong implications for dissolution and transport in CO_2 sequestration processes. For instance, solubility trapping is thought to be rate-limited by the molecular diffusion of the dissolved CO_2 away from the interface [21]. However, the continuum-scale shear-induced circulation identified in the trapped water, and the concomitant advective transport, will certainly enhance the dissolution beyond molecular effects. As a result, the time scales associated with different trapping mechanisms (section 1.3.2), particularly solubility and mineral trapping, may be substantially altered at the pore scale in a manner that is intimately tied to the pore-scale flow dynamics. Unfortunately, none of the unique pore-scale flow dynamics reported herein are

embodied in state-of-the-art pore-scale modeling methods used in reservoir-scale predictions of CO_2 fate [102]–[104]. This may explain why such reservoir-scale simulations yield extremely poor predictions of CO_2 fate in geologic formations compared to field observations from actual geologic sequestration sites [105], [106].

4.3 Figures and tables

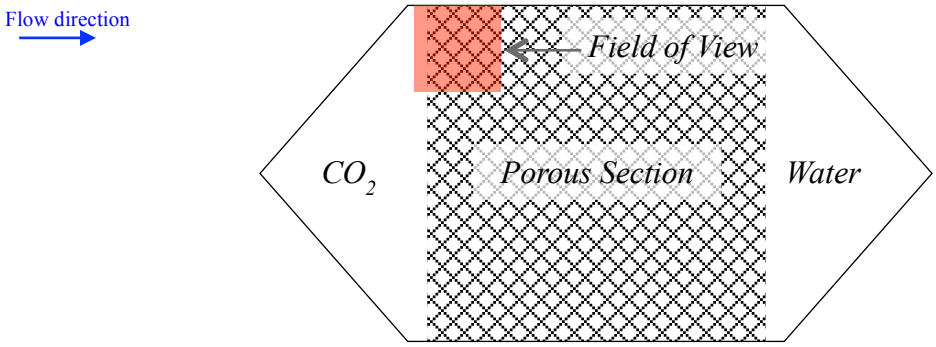

Figure 4.1 – Schematic diagram of the micro-model showing the field of view of the imaging system for data presented in Figs. 4.2–4.13

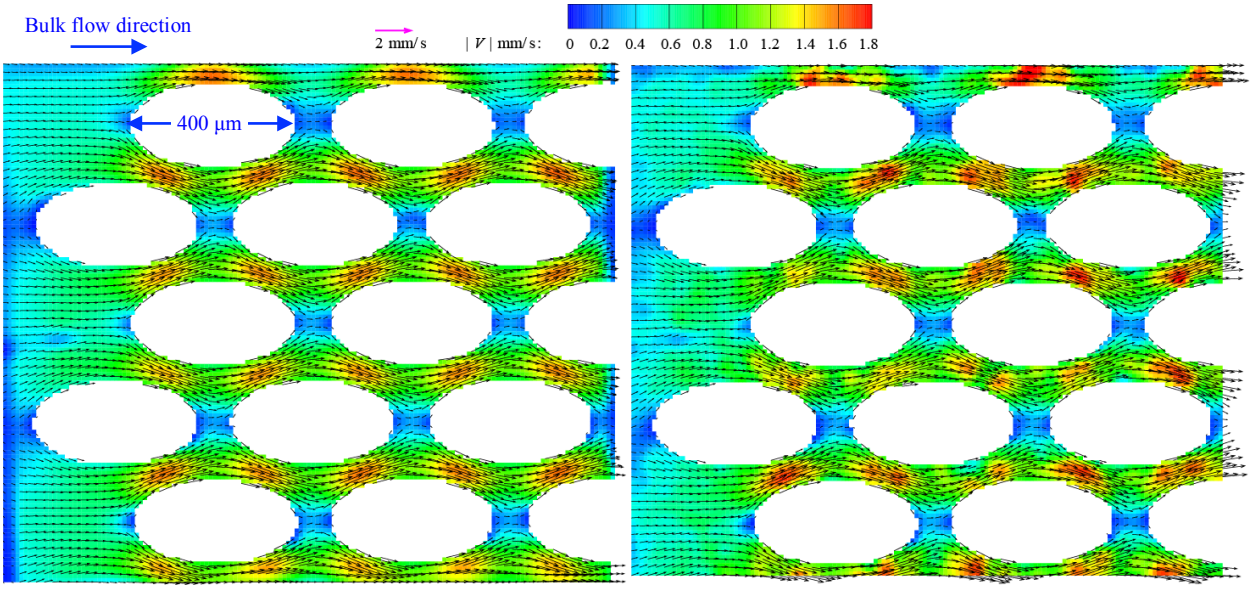

Figure 4.2 – Velocity vector field overlaid with velocity magnitude contours
Left: *Ensemble average* **Right:** *Instantaneous*

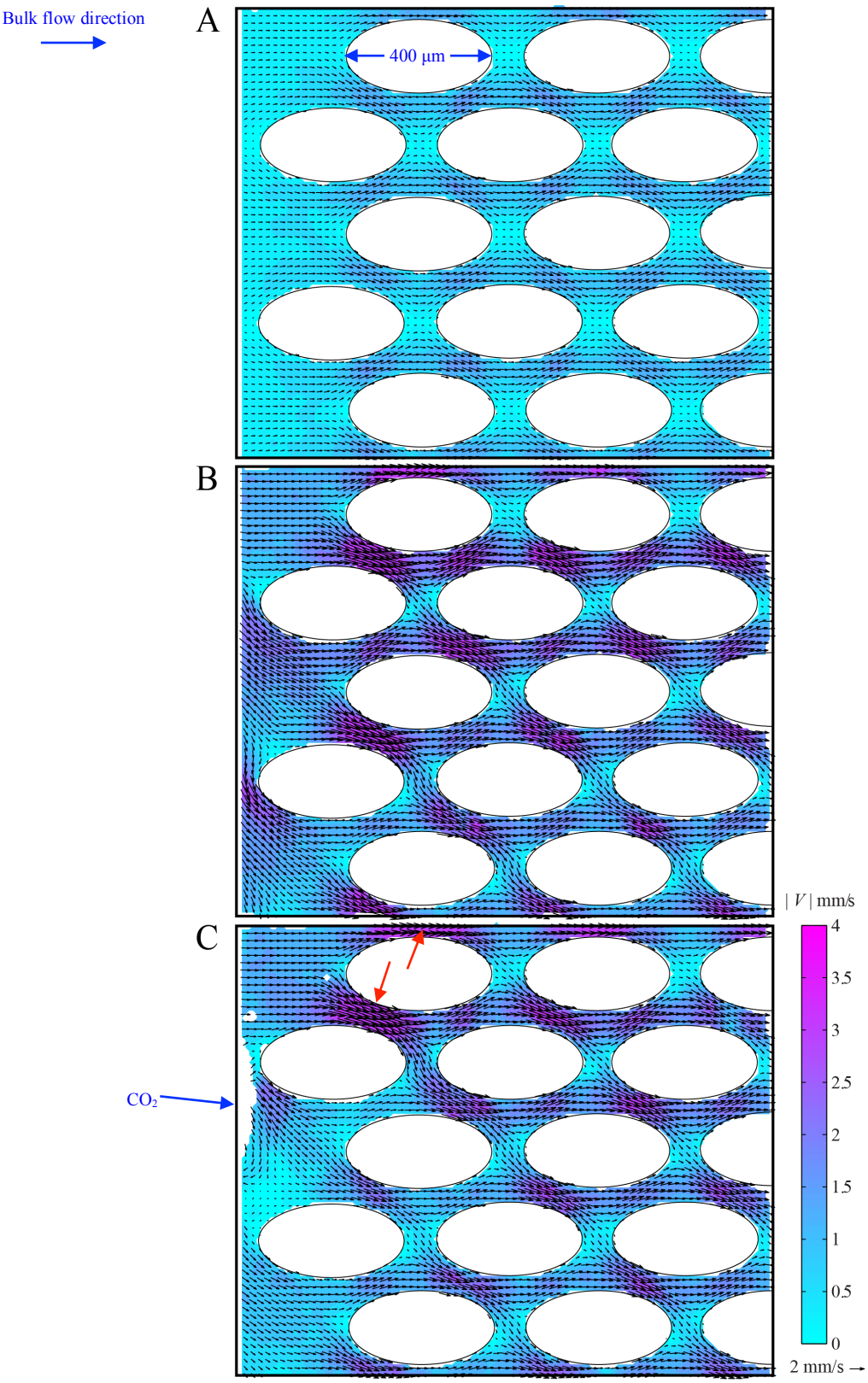

Figure 4.3 – Instantaneous velocity fields showing unsteady flow before the appearance of CO_2. Only the flow field in the water phase is resolved. **A.** *Frame 1 – Steady periodic flow field,* **B.** *Frame 18 – Flow field becomes unsteady,* **C.** *Frame 25 – CO_2 appears. Arrows show location of max. velocity*

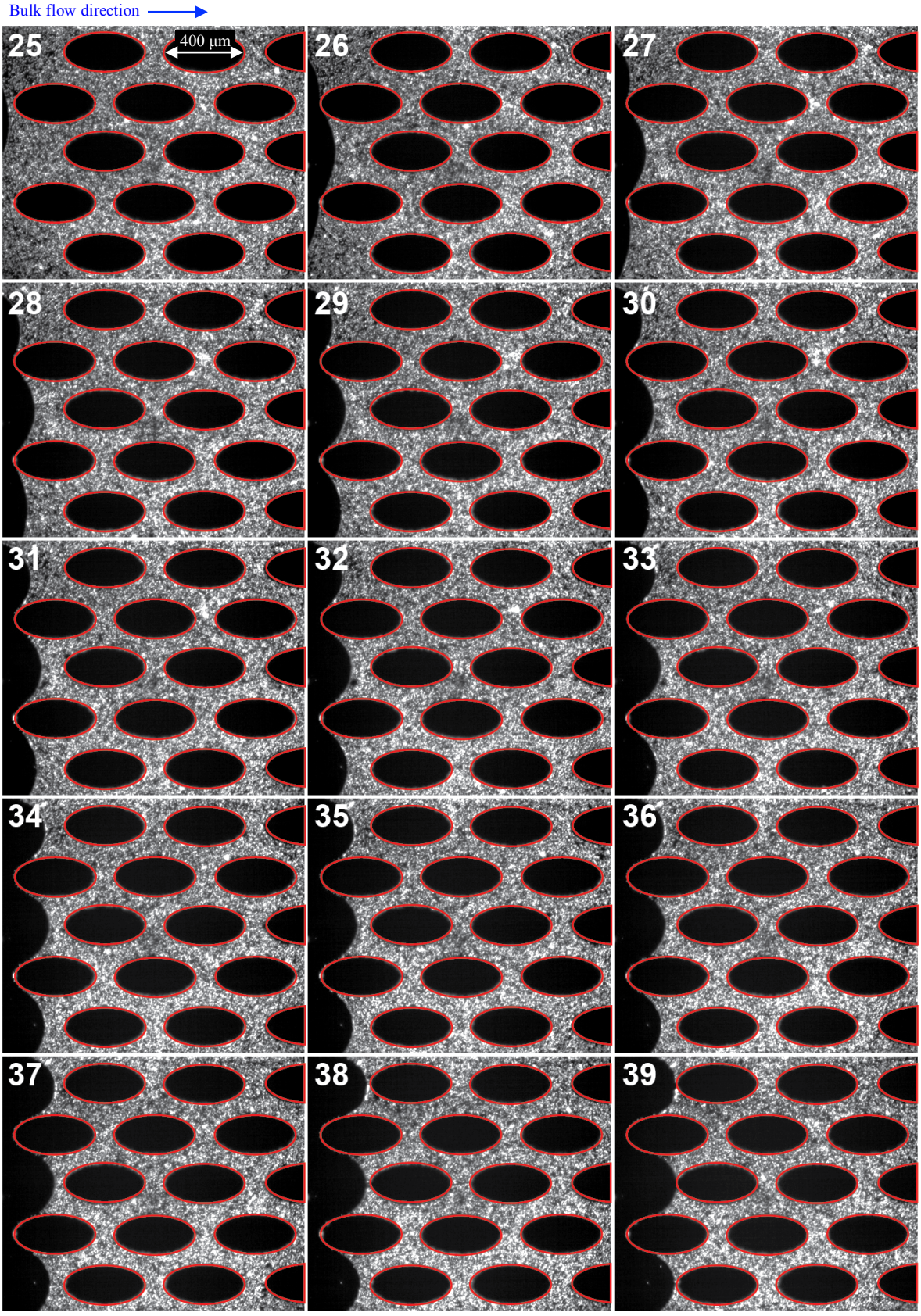

Figure 4.4 – Frames 25A to 39B from the drainage experiment (Δt between frames = 100 ms)

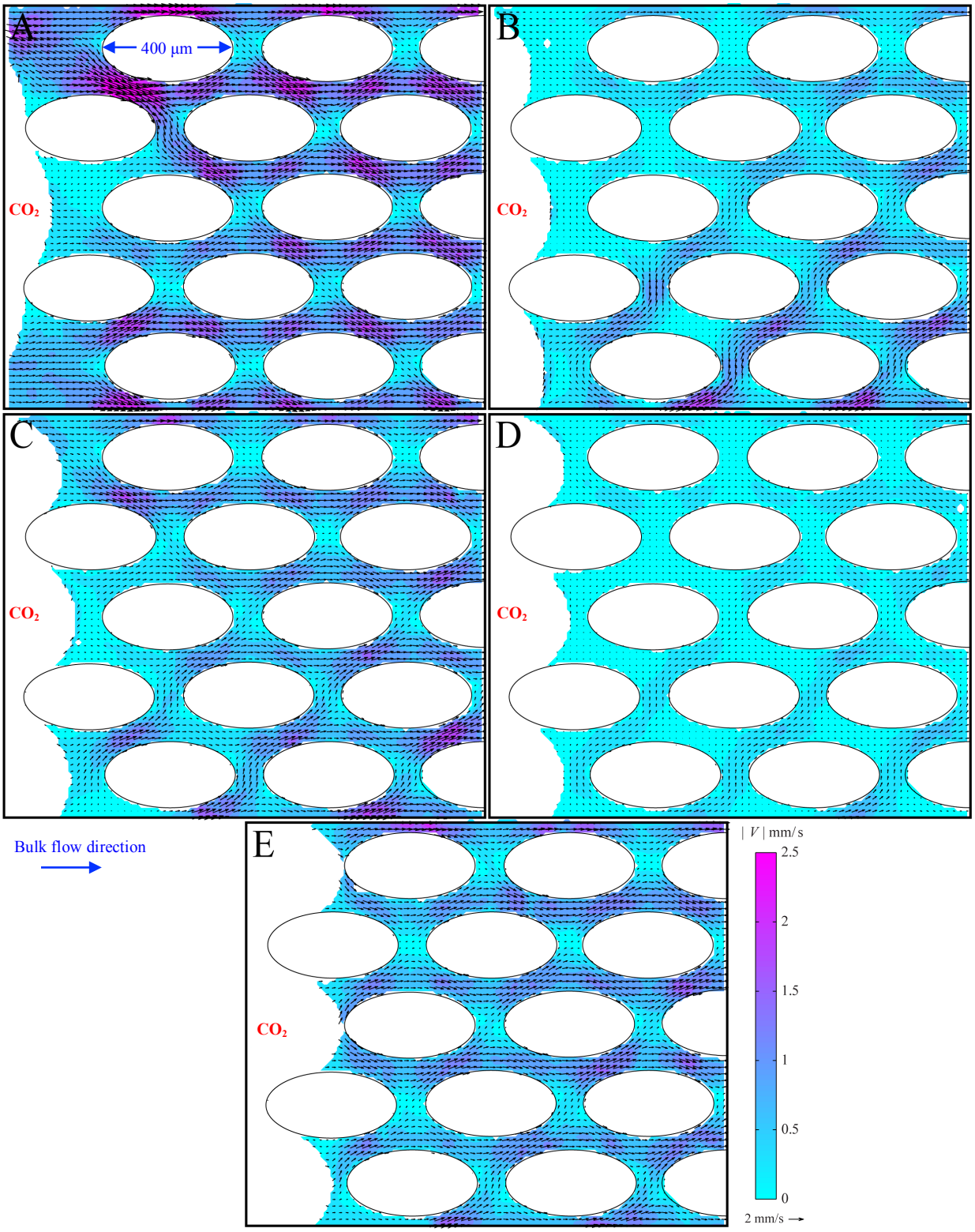

Figure 4.5 – Velocity vector fields showing CO_2 front propagation (Refer to Fig. 4.4)
A. *Frame 26* **B.** *Frame 29* **C.** *Frame 32* **D.** *Frame 35* **E.** *Frame 38*

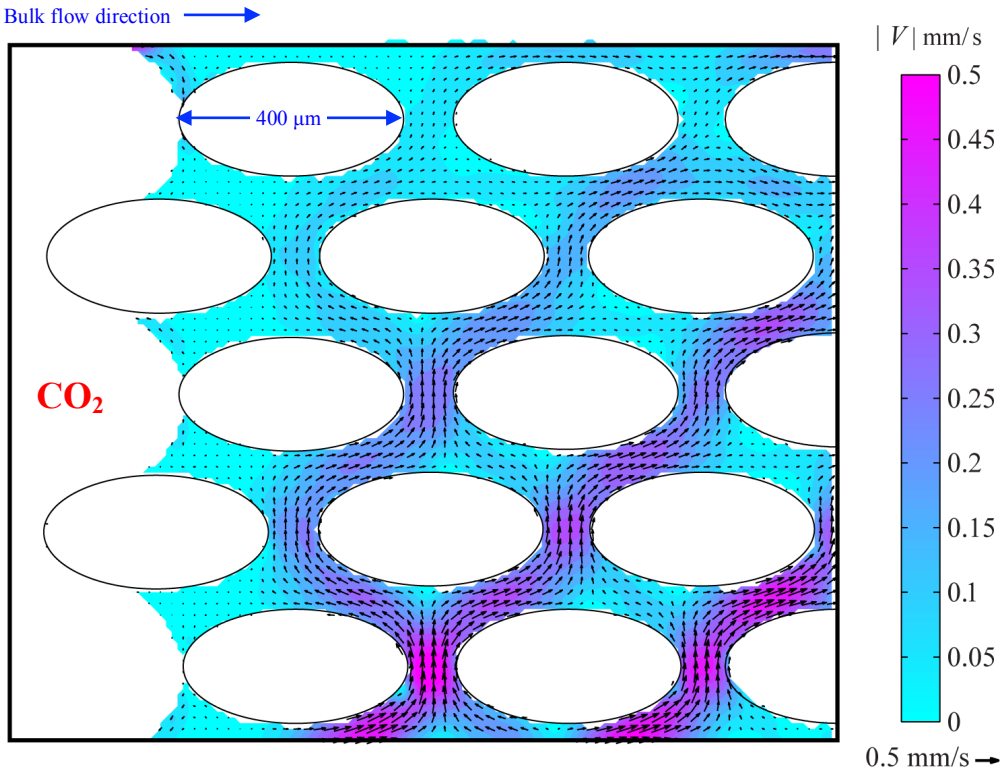

Figure 4.6 – Ensemble average velocity field frames 40-64

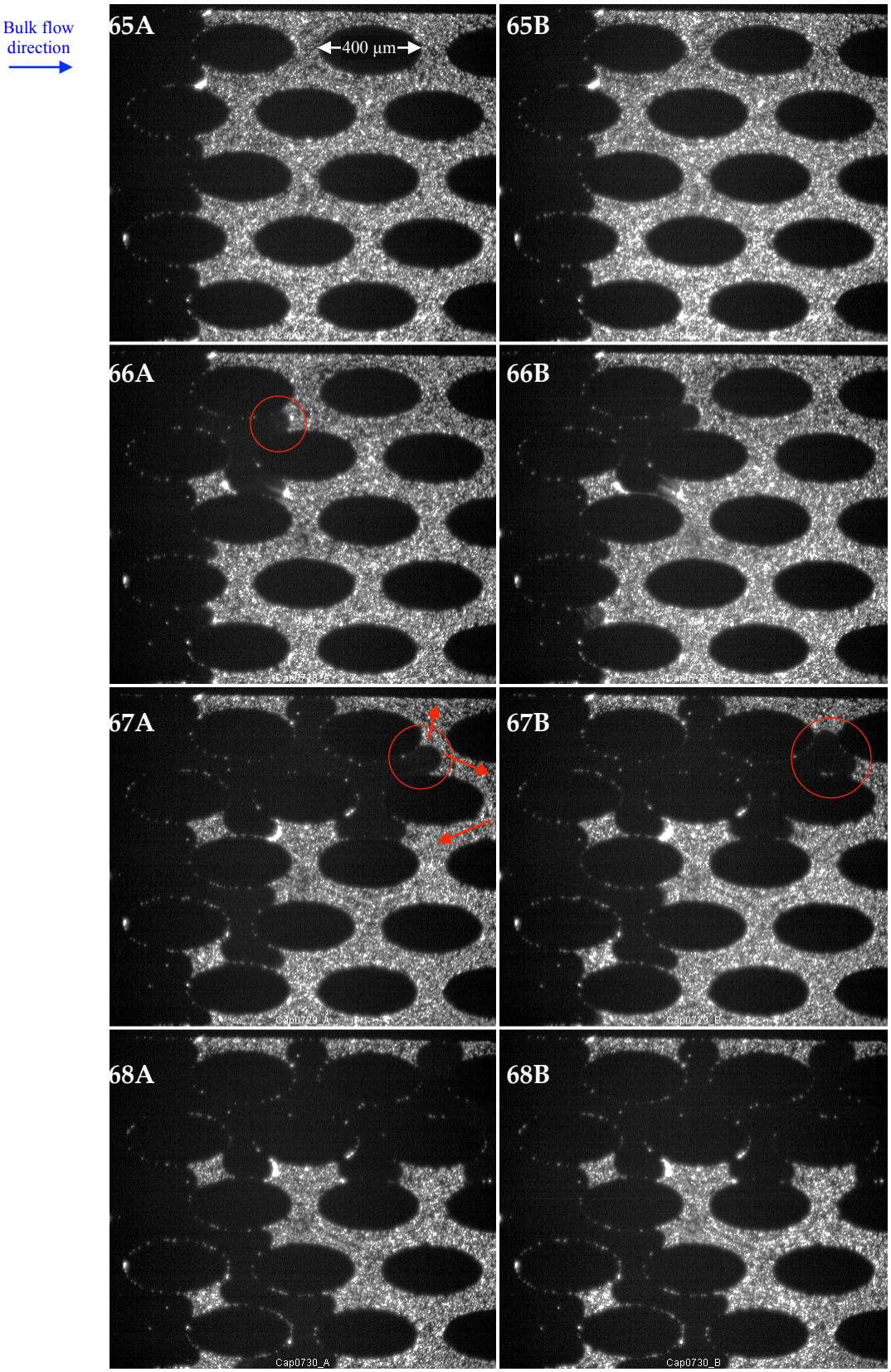

Figure 4.7 – Raw PIV images showing CO_2 fingers invasion (Frames 65-68)
Δt between columns = 6 ms, Δt between rows = 100 ms

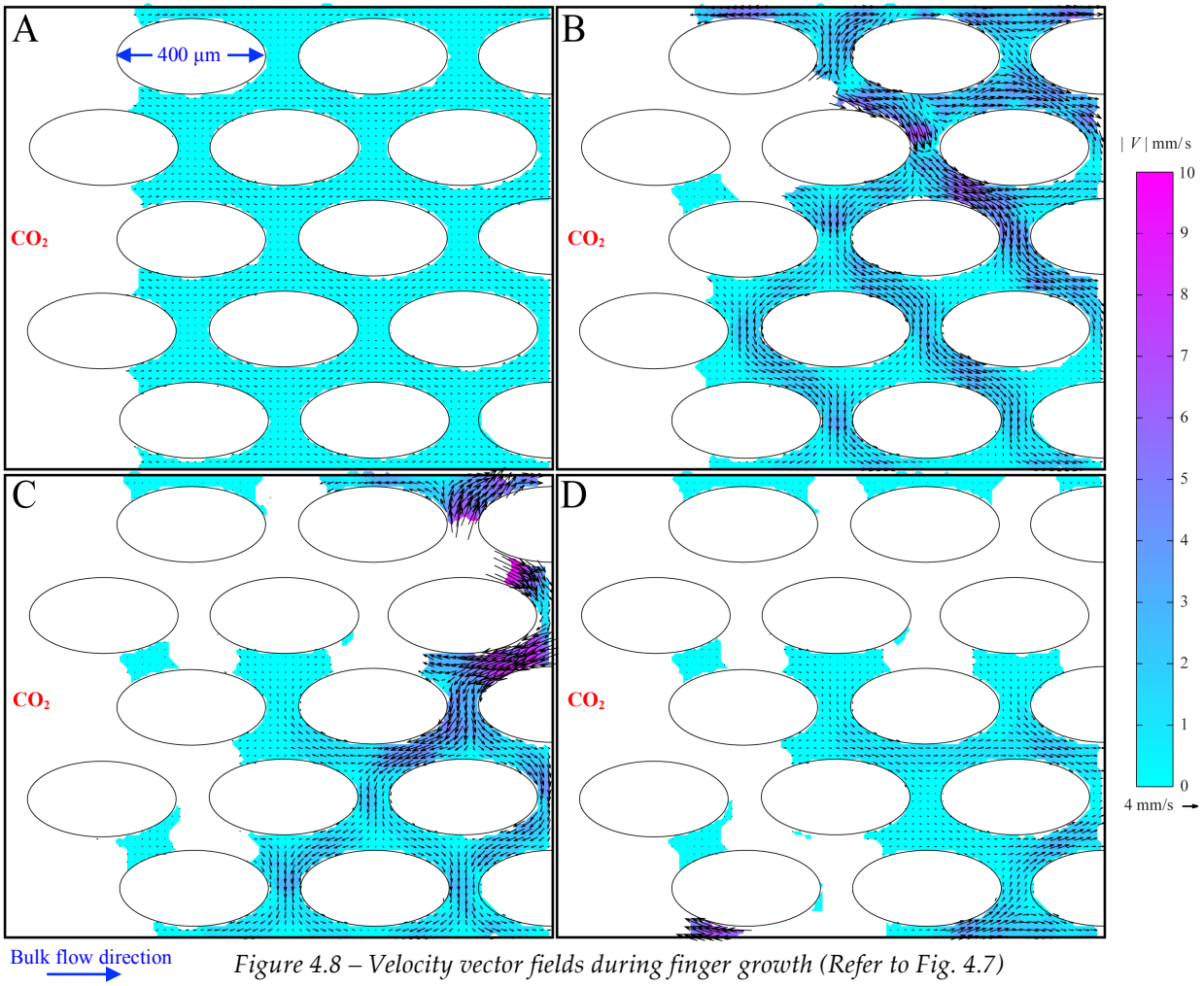

Figure 4.8 – Velocity vector fields during finger growth (Refer to Fig. 4.7)
A. *Frame 65* **B.** *Frame 66* **C.** *Frame 67* **D.** *Frame 68*

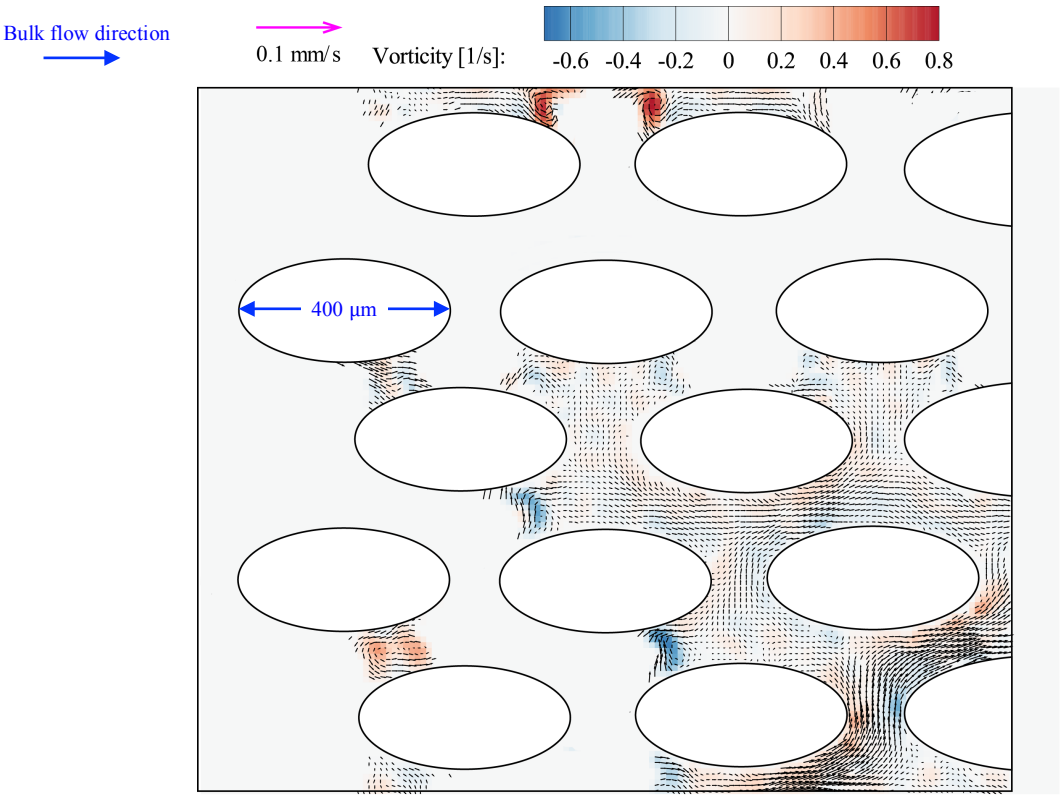

Figure 4.9 – Velocity vector field overlaid with vorticity contours depicting the circulation zones in water near the fluid-fluid interfaces after the CO_2 front has passed (Flow rate: 0.005 ml/min from left to right)

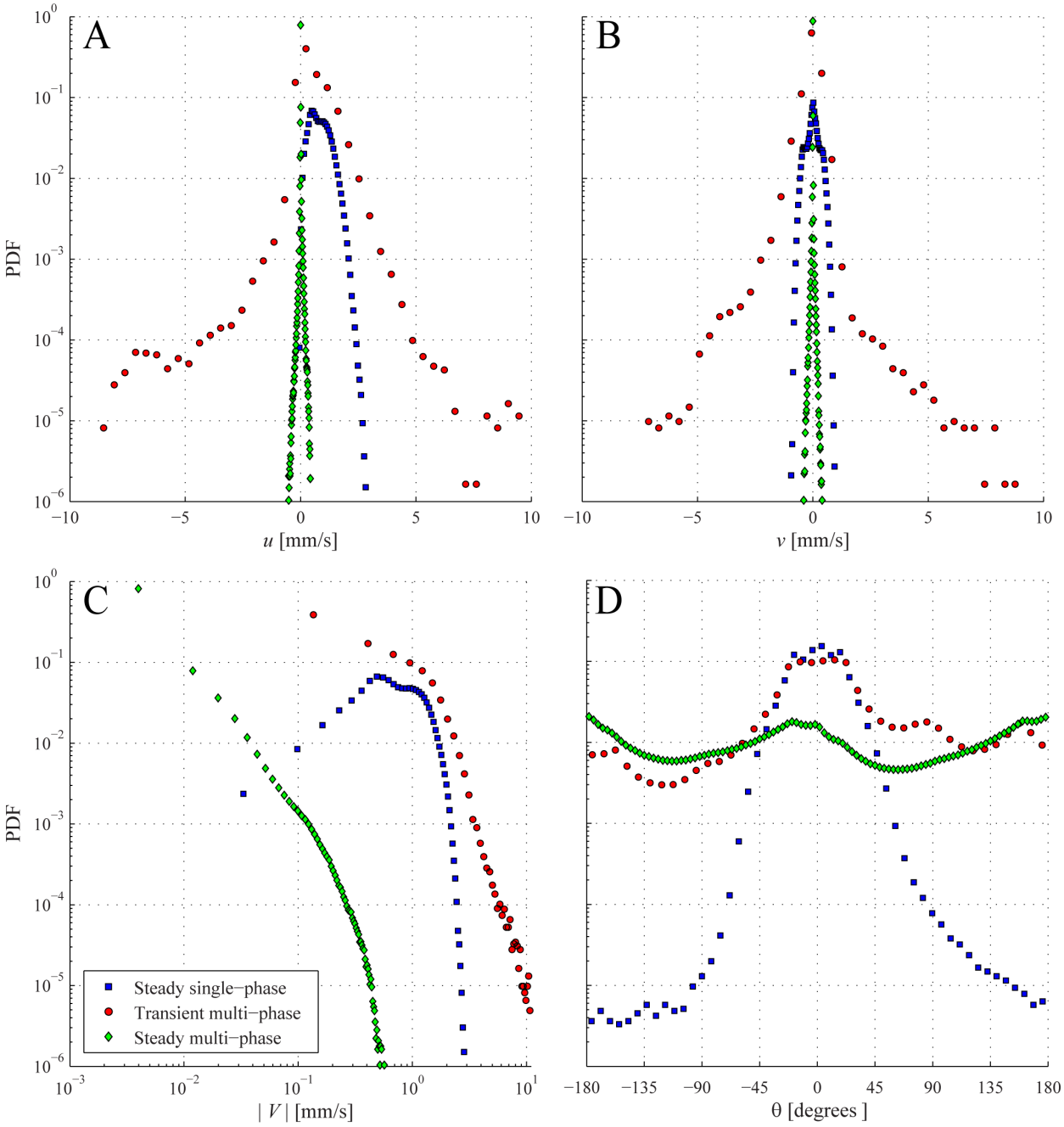

Figure 4.10 – Probability density functions

A) *Velocity component in the bulk flow direction (u)* **B)** *Velocity component normal to the bulk flow direction (v)* **C)** *Velocity magnitude,* $|V|$ **D)** *Velocity vector angle with respect to the bulk flow direction,* θ

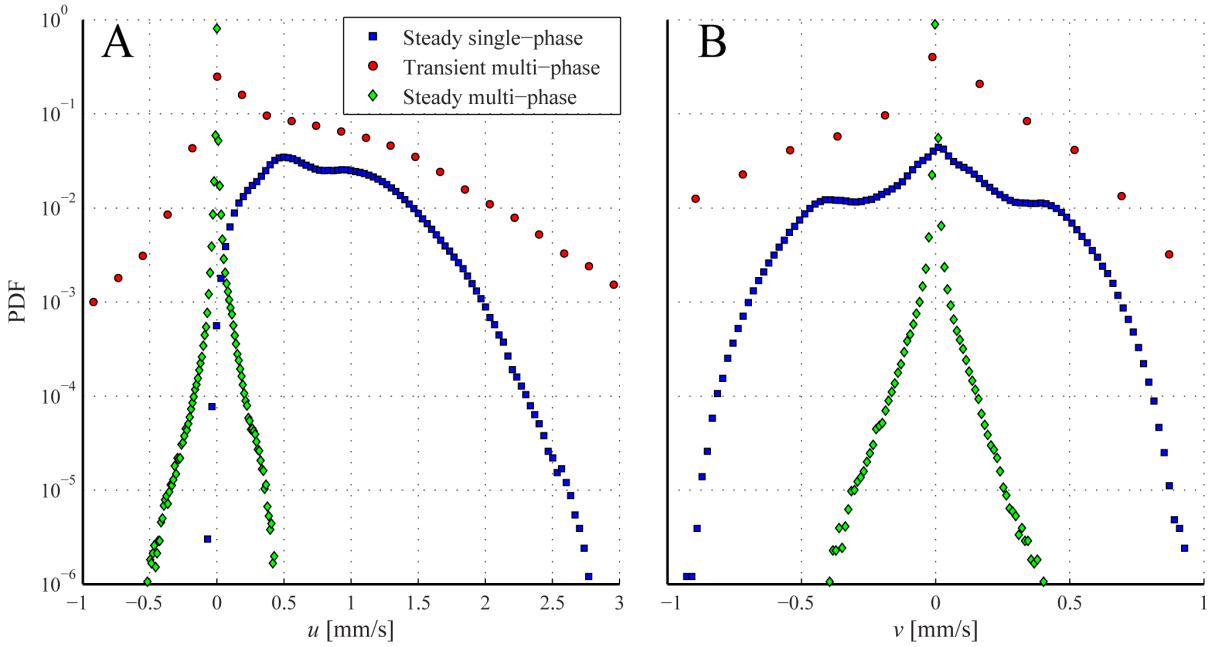

Figure 4.11 – Zoomed-in view of probability density functions from Fig. 4.10A and B

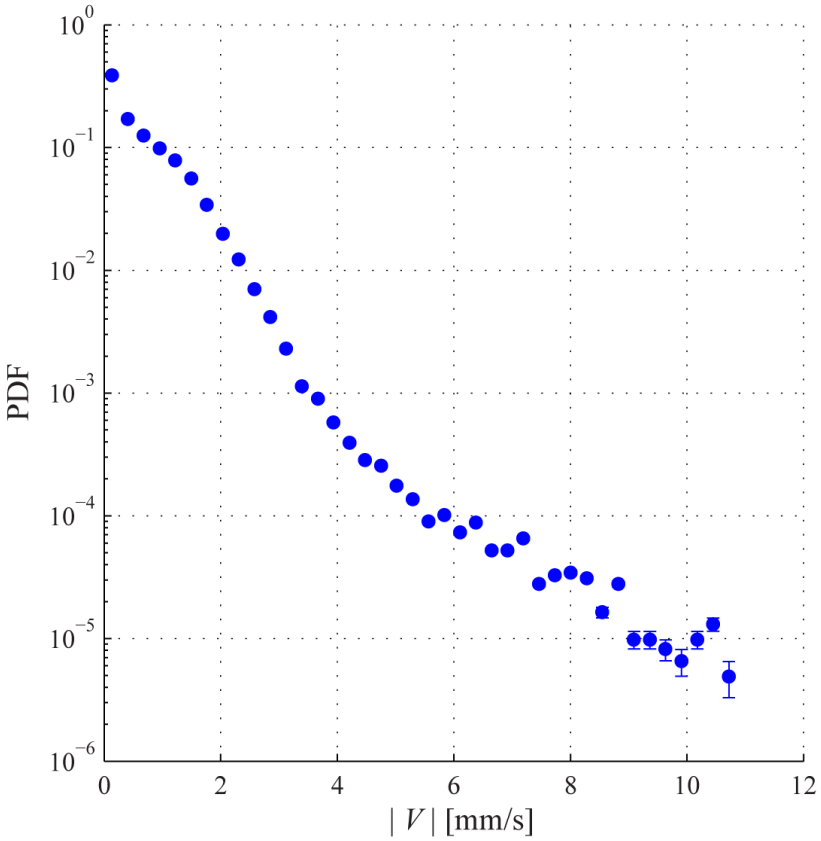

Figure 4.12 – Probability density function with error bars for velocity magnitude in the transient multi-phase flow stage

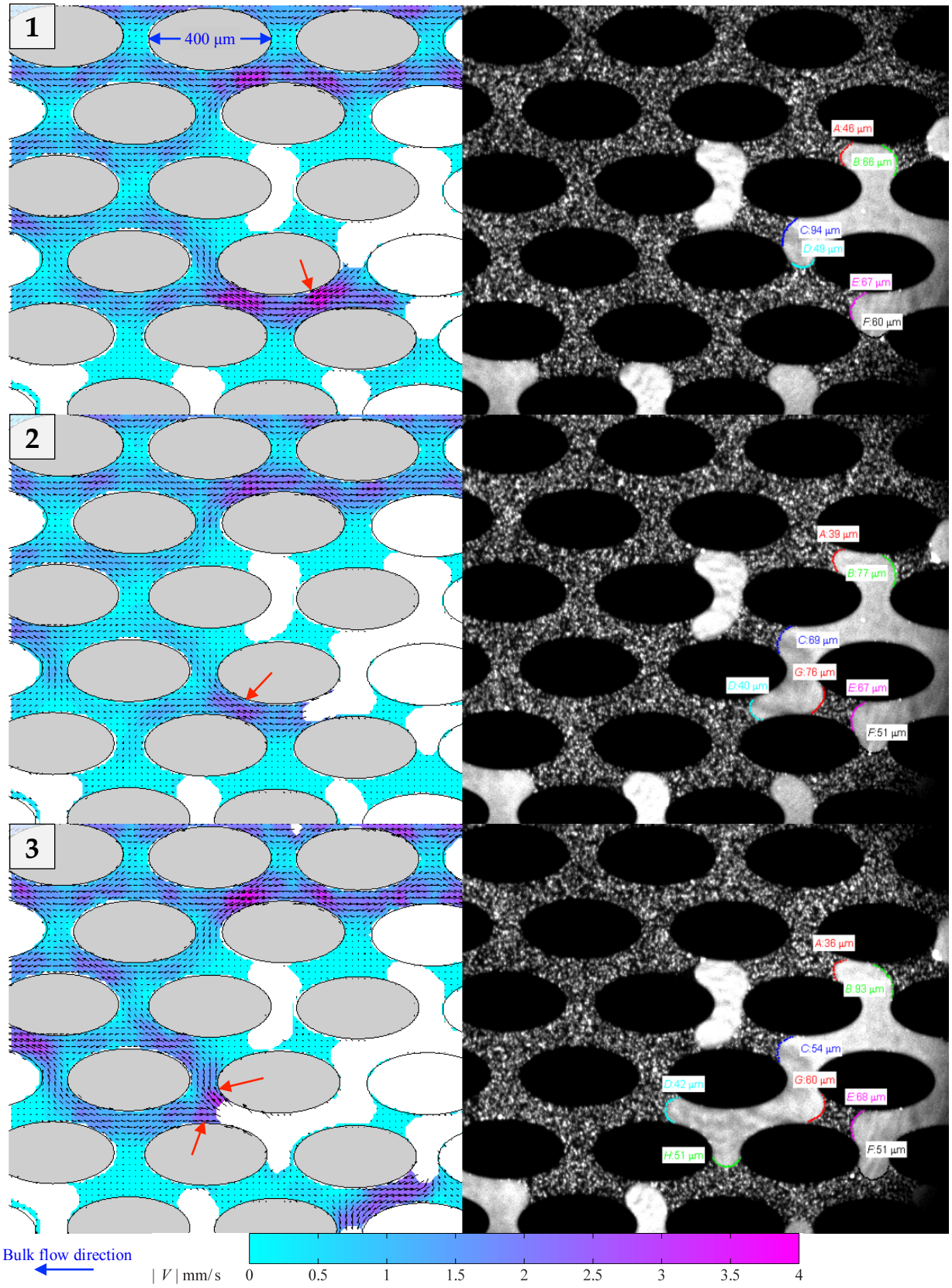

Figure 4.13 – Interfacial curvature and velocity vector field. High momentum pathways marked with arrows. Flow from right to left. The letters correspond to the numbering of the menisci in Table 4.1.

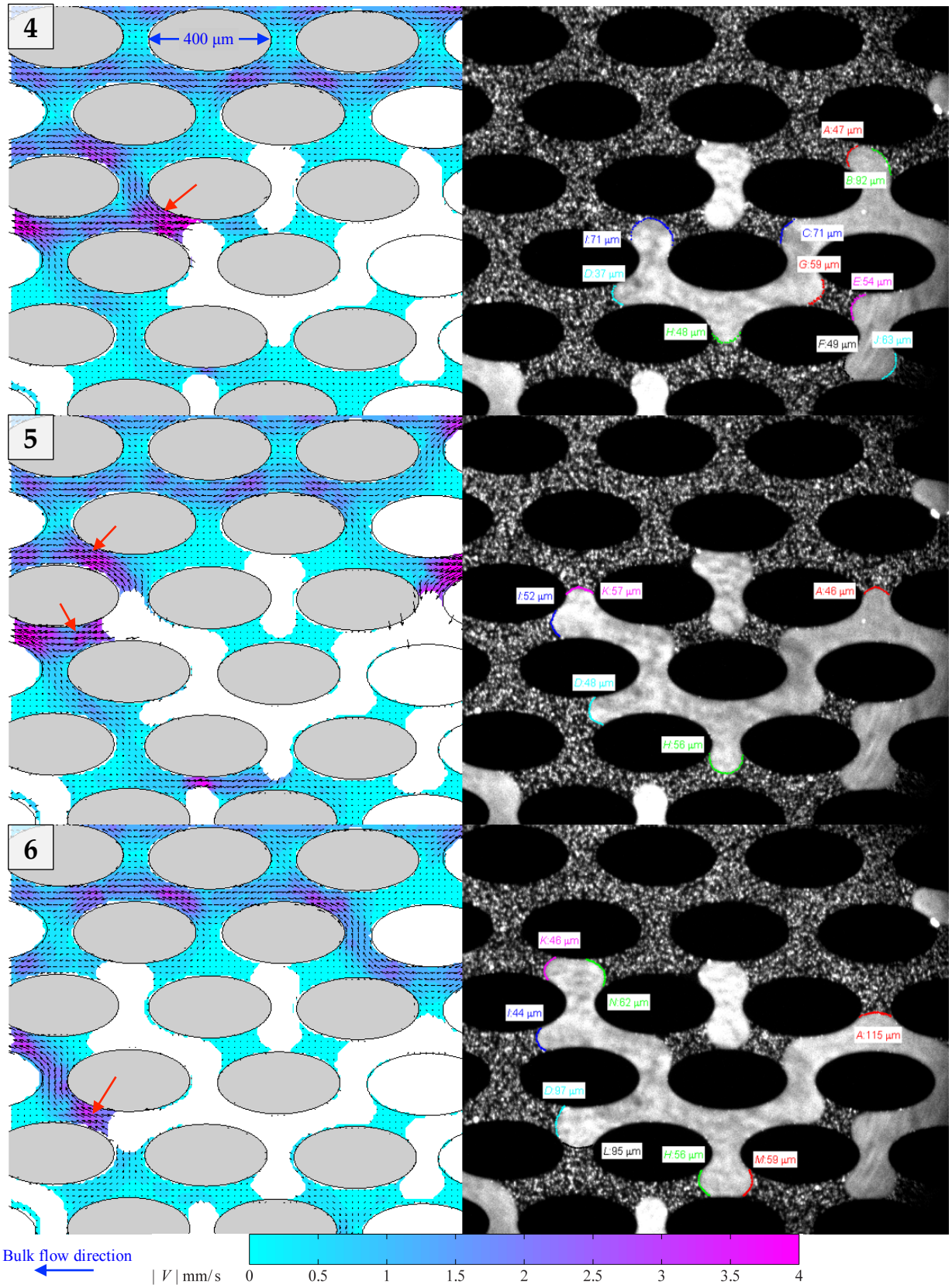

Figure 4.13 (Cont.) – Interfacial curvature and velocity vector field. High momentum pathways marked with arrows. Flow from right to left. . The letters correspond to the numbering of the menisci in Table 4.1.

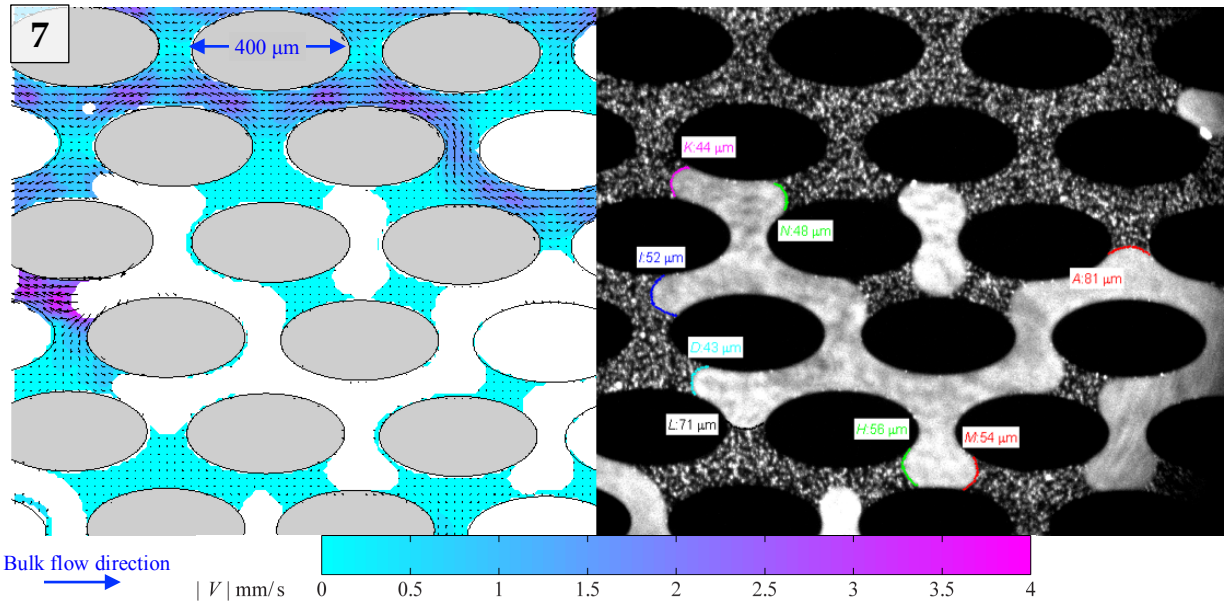

Figure 4.13 (Cont.) – Interfacial curvature and velocity vector field. High momentum pathways marked with arrows. Flow from right to left. The letters correspond to the numbering of the menisci in Table 4.1..

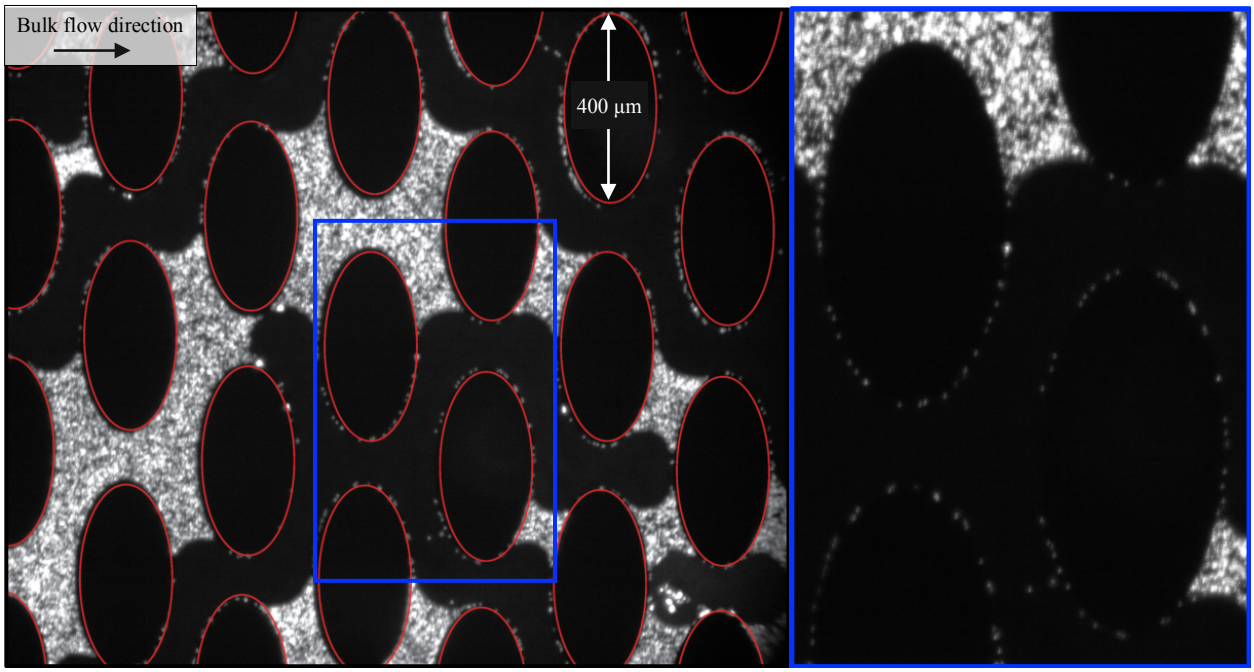

Figure 4.14 – Raw PIV image depicting water as the regions with bright particles and CO_2 as dark regions. **Left:** *Elliptic pillars of the silicon micro-model outlined in red* **Right:** *Zoomed-in view of the image that shows the water films covering the circumference of the pillars*

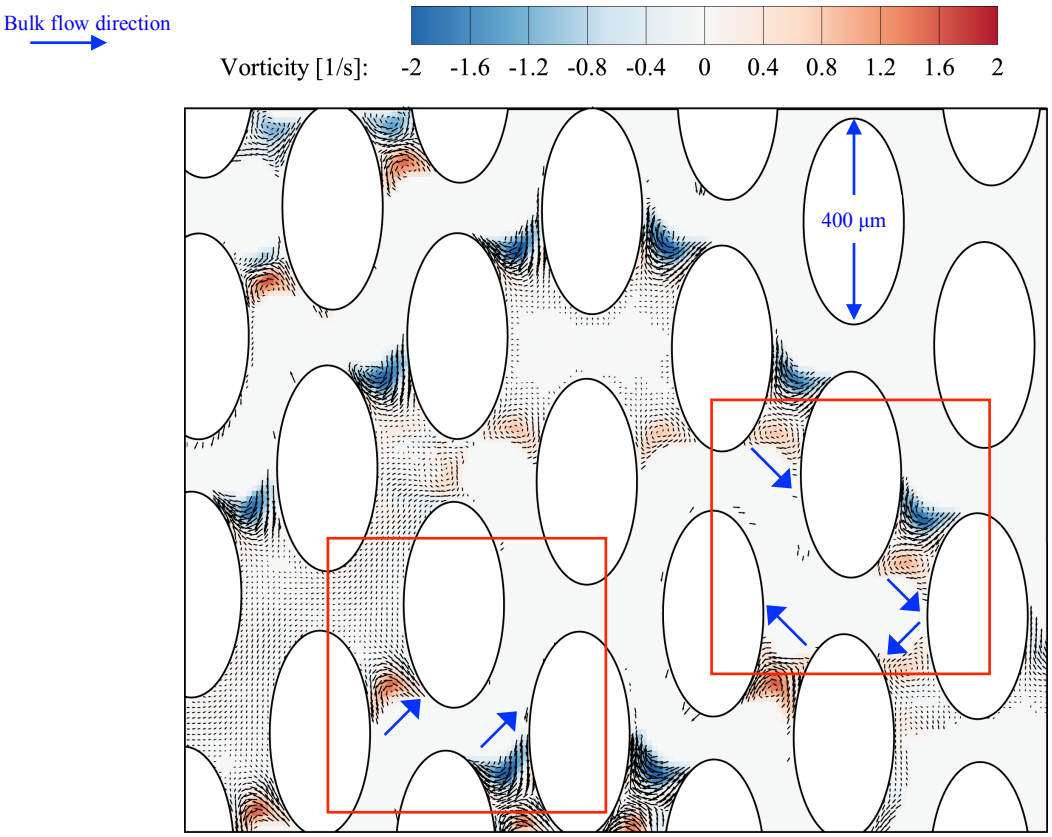

Figure 4.15 – Velocity vector field overlaid with vorticity map depicting the circulation zones in water near the fluid-fluid interfaces (Flow rate: 0.05 ml/min from left to right)

Table 4.1 – Capillary pressure for menisci shown in Fig. 4.13

	Capillary pressure, P_c [Pa]						
Frame / Meniscus	**1**	**2**	**3**	**4**	**5**	**6**	**7**
A	1082	1200	1265	1068	1082	687	797
B	882	817	749	753			
C	746	862	984	850			
D	1042	1181	1145	1242	1055	736	1128
E	876	876	869	984			
F	928	1017	1017	1042			
G		822	928	937			
H			1017	1055	964	964	964
I				850	1006	1112	1006
J				904			
K					955	1082	1112
L						742	850
M						937	984
N						912	1055

5. Summary, conclusions, and recommendations

The flow of CO_2 in configurations relevant to CO_2 sequestration was investigated. The first configuration was CO_2 flow in pipes and orifices at pressures and temperatures close to the critical point of CO_2 (74 bar, 31°C), which is of importance for CO_2 transport in pipelines from sources (fossil fuel power plants, for example) to storage sites (saline aquifers, for example). Also, injection of CO_2 into geological storage sites occurs at conditions near critical point of CO_2. In order to investigate the effects of pressure and temperature on flow near the critical point, pressure drop in pipes was measured for different inlet conditions (pressure, temperature, mass flow rate). Also, the shadowgraph technique was applied in order to visualize the flow structure. In a second configuration, liquid/supercritical CO_2 was injected into two-dimensional porous micro-models saturated with water, which mimics the process of injection and flow into saline aquifers. This flow configuration was studied using fluorescent microscopy and micro-PIV by seeding the water phase with fluorescent tracer particles, and dyeing CO_2 with a fluorescent dye. This allowed for measurement of the velocity field in the water phase, and tracking the CO_2 phase in the porous medium.

5.1 Summary and conclusions

5.1.1 Pipe flow and throttling

Pipe flow of CO_2 at near critical conditions demonstrated a seemingly complicated behavior when viewed in terms of raw values of ΔP and $\dot{m}$. The apparent complication has to do with the occasional sensitivity to inlet temperature and the dependence of pressure drop on flow rate. In

particular, in experiments that were performed in a 60-cm long stainless steel pipe with 6.35 mm (0.25 in) outer diameter and 2.13 mm (0.084 in) inner diameter, it was established that at constant inlet pressure, $\Delta P/L$ was insensitive to changes in inlet temperature when $T_{in} > T_{crit}$, for the mass flow rates less than 5 g/s. At higher mass flow rates, ΔP decreased with decreasing temperature. Furthermore, few data points seem to indicate that the smallest ΔP for a given mass flow rate and inlet pressure was always observed at subcritical inlet temperature. However, it was also established that this seemingly complicated picture in terms of raw quantities was drastically simplified if Reynolds number and friction factor were defined in terms of inlet quantities. Then, the near-critical two-phase flow behaved in a manner very closely predicted by the classical Moody chart for single-phase hydraulics!

This was rationalized using shadowgraph visualizations of the flow transition of CO_2 from a supercritical state to a subcritical two-phase state, which are the first of their kind to the author's knowledge. During this transition, the two phases separate and create cell-like structures with very sharp density gradients at the boundaries. The density difference leads to a buoyancy-driven separation of the phases and results in an interface travelling in the direction of the flow and separating two regions of essentially single-phase flow, which accounts for the agreement with the predictions of the Moody chart.

During Joule-Thompson throttling at the elevated pressures that are relevant for CO_2 sequestration, near-critical CO_2 was shown to undergo a cooling on the order of 0.5ºC/bar of pressure difference across the throttling orifice. The precise value of the Joule-Thompson coefficient increases with increasing inlet enthalpy. There is a substantial difference of the measured coefficient with data currently available from a NIST database, especially when $h_{in} < h_{crit}$ (although the order of magnitude agrees). This was attributed to the way the NIST model was constructed as well as to the fact that the data that support it were not taken at the elevated pressures relevant for CO_2 sequestration.

5.1.2 Flow in porous micro-models

An experimental setup with carefully selected optical filters, light sources, and fluorescent dyes and particles, was developed to make application of the micro-PIV technique possible for this problem. The drainage flow processes (displacement of water by CO_2) was studied in an experiment conducted at 80 bar pressure 40°C temperature where CO_2 was in supercritical state. For a value of the capillary number, *Ca*, equal to 3.4×10^{-7} and viscosity ratio, *M*, equal to 0.03, the complete sequence of events occurring prior to, during, and after CO_2 front invasion was recorded. Based on the velocity vector fields obtained with micro-PIV in the water flow, three distinct flow stages were identified: i) the steady flow before CO_2 enters the micro-model, ii) the passage of the CO_2 front and iii) the post-front-passage evolution. During the passage of the CO_2 front, penetration of CO_2 into the porous section was captured, which occurred through very sudden and rapid growth of dendritic features (fingers). The peak velocity in the field in this stage was 20–25 times greater than the bulk velocity. These velocities occurred even in the opposite direction of the bulk flow. The sudden velocity jumps support the notion of Haines jump during front propagation.

After the passage of the CO_2 front, the distribution of the two fluids remained unchanged. Water appeared stagnant except for the shear-induced circulation zones observed in water near the fluid-fluid interfaces. These circulation zones were further investigated in a separate experiment. The results revealed an interesting flow feature whereby two CO_2 streams flowed in opposite directions within a flow pathway. The existence of such flow features can have strong implications for dissolution and transport in CO_2 sequestration processes, as the diffusion-limited processes may be enhanced significantly due to the advective transport associated with the aforementioned shear-induced motion.

The variations of capillary pressure during CO_2 finger growth was also studied, at supercritical pressure of 80 bar and subcritical temperature of 24°C, corresponding to Ca = of 9.8×10^{-6} and M = 0.08. The

variations in the curvature of the menisci and the velocity field were considered along with each other to understand the flow dynamics. The following conclusions can be drawn from those observations:

i. The growing branch of CO_2 had the meniscus with the smallest radius of curvature.
ii. The growth direction of CO_2 fingers followed the high-momentum pathways, which were defined as high-velocity flow paths of water in the porous medium that appeared to form downstream of the fluid-fluid front.
iii. The drainage event in a pore is nonlocal and cooperative, in the sense that it can result in menisci receding in pores far from the draining pore. This connection was observed in two locations approximately five pores apart.

5.2 Recommendations for future work

The present experimental work provides a foundation for identifying the important steps for future research in this area. In particular, the following directions are recommended for future research:

i. A key next step for future studies is high-speed flow visualization that would enable resolving the high-velocity events in the flow, discussed in section 4.1. Interfacial velocities up to three orders of magnitude greater than the bulk velocity have been reported in the literature [50]. Due to the limited image acquisition rate used for micro-PIV, capturing the Haines jumps proved elusive. Thus, it is crucial to employ a high-speed visualization system to resolve the high velocities associated with these jumps.
ii. An important parameter in multi-phase flow of immiscible fluids is the interfacial velocity. In future work this velocity should be measured and its relationship with fluid velocity studied. It must be noted that the interfacial velocity measurement would be most useful when carried out with high-speed visualizations, because as discussed earlier in chapters 1 and 4, the interface

advances through velocity jumps resulting from sudden pressure bursts.

iii. A limitation in this study was that the field of view covered only a fraction of the porous section of the micro-model. As a result, the events occurring outside this field of view, which may affect the flow within the field of view, were unknown. It is desirable to have a micro-model that is narrow enough such that its entire width would be visible in the field of view. The trade-off, however, is that the sidewall effects may become more significant and not negligible. Nevertheless, the benefits of having the entire width of the micro-model in the field of view will most probably outweigh its drawbacks. For instance, one major challenge in our experiments was to capture the CO_2 front when it first entered the porous section, which can be overcome with this approach. Another possible approach to overcome this limitation is improving the optical system to include a lens with higher numerical aperture (NA) that would yield a larger field of view. However, relatively speaking, objective lenses with high NA usually have shorter working distances, which might be incompatible with the 0.25-inch thickness of the sapphire window of the pressure cell.

iv. Another aspect of the experiments that can be improved is pressure measurement. In this work, pressure was set to a constant value but its variations were not recorded. Accurate measurement and recording of the pressure of each fluid phase, as well as the pressure difference across the micro-model can help better understand the flow physics. Pressure data can be linked to the flow events such as Haines jumps, and may explain the velocity fluctuations reported in section 4.1.

v. Future work should also entail studying flow in heterogeneous micro-models. The geometry of porous media, and in particular its homogeneity, or lack thereof, have significant influences on the flow phenomena. Two-dimensional porous micro-models can be fabricated using the geometry of core samples, such as the micro-model used by Zuo et el. [38].

vi. Seeding CO_2 with suitable tracer particles will allow velocity field measurement in the CO_2 phase

as well as the water phase. The challenges and roadblocks for finding such particles were described in section 2.2.4. If overcome, simultaneous velocity measurement in both phases would give a comprehensive picture of the flow field and the relevant phenomena.

6. References

[1] R. K. Pachauri and A. Reisinger, *Climate Change 2007 Synthesis Report*. IPCC Secretariat, 2007.

[2] H. Friedli, H. Lötscher, H. Oeschger, U. Siegenthaler, and B. Stauffer, "Ice core record of the $^{13}C/^{12}C$ ratio of atmospheric CO_2 in the past two centuries," *Nature*, vol. 324, no. 6094, pp. 237–238, Nov. 1986.

[3] E. Dlugokencky and P. Trans, "Trends in Atmospheric Carbon Dioxide (NOAA/ESRL)." [Online]. Available: www.esrl.noaa.gov/gmd/ccgg/trends/.

[4] S. Pacala and R. Socolow, "Stabilization wedges: solving the climate problem for the next 50 years with current technologies.," *Science*, vol. 305, no. 5686, pp. 968–72, Aug. 2004.

[5] S. Bachu, "Sequestration of CO_2 in geological media: criteria and approach for site selection in response to climate change," *Energy Convers. Manag.*, vol. 41, no. 9, pp. 953–970, 2000.

[6] R. S. Haszeldine, "Carbon capture and storage: how green can black be?," *Science*, vol. 325, no. 5948, pp. 1647–52, Sep. 2009.

[7] C. M. White, B. R. Strazisar, E. J. Granite, J. S. Hoffman, and H. W. Pennline, "Separation and capture of CO_2 from large stationary sources and sequestration in geological formations--coalbeds and deep saline aquifers.," *J. Air Waste Manag. Assoc.*, vol. 53, no. 6, pp. 645–715, Jun. 2003.

[8] B. Hitchon, W. D. Gunter, T. Gentzis, and R. T. Bailey, "Sedimentary basins and greenhouse gases: a serendipitous association," *Energy Convers. Manag.*, vol. 40, no. 8, pp. 825–843, May 1999.

[9] H. Koide, Y. Tazaki, Y. Noguchi, S. Nakayama, M. Iijima, K. Ito, and Y. Shindo, "Subterranean containment and long-term storage of carbon dioxide in unused aquifers and in depleted natural gas reservoirs," *Energy Convers. Manag.*, vol. 33, no. 5–8, pp. 619–626, May 1992.

[10] W. D. Gunter, B. Wiwehar, and E. H. Perkins, "Aquifer disposal of CO_2-rich greenhouse gases: Extension of the time scale of experiment for CO_2-sequestering reactions by geochemical modelling," *Mineral. Petrol.*, vol. 59, no. 1–2, pp. 121–140, 1997.

[11] R. M. Enick and S. M. Klara, "CO_2 solubility in water and brine under reservoir conditions," *Chem. Eng. Commun.*, vol. 90, no. 1, pp. 23–33, Apr. 1990.

[12] F. Kazemifar and D. C. Kyritsis, "Experimental investigation of near-critical CO_2 tube-flow and Joule–Thompson throttling for carbon capture and sequestration," *Exp. Therm. Fluid Sci.*, vol. 53, pp. 161–170, 2014.

[13] F. Kazemifar and D. C. Kyritsis, "Near-Critical CO_2 Flow Measurement and Visualization," *J. Energy Resour. Technol.*, vol. 137, no. 1, p. 012002, Aug. 2014.

[14] P. J. Linstrom and W. G. Mallard, *NIST Chemistry WebBook; NIST Standard Reference Database No. 69*. Gaithersburg MD, 2001.

[15] V. Vesovic, W. A. Wakeham, G. A. Olchowy, J. V. Sengers, J. T. R. Watson, and J. Millat, "The Transport Properties of Carbon Dioxide," *J. Phys. Chem. Ref. Data*, vol. 19, no. 3, p. 763, May 1990.

[16] A. Fenghour, W. A. Wakeham, and V. Vesovic, "The Viscosity of Carbon Dioxide," *J. Phys. Chem. Ref. Data*, vol. 27, no. 1, p. 31, Jan. 1998.

[17] G. A. Olchowy and J. V. Sengers, "A simplified representation for the thermal conductivity of fluids in the critical region," *Int. J. Thermophys.*, vol. 10, no. 2, pp. 417–426, Mar. 1989.

[18] R. Span and W. Wagner, "A New Equation of State for Carbon Dioxide Covering the Fluid Region from the Triple-Point Temperature to 1100 K at Pressures up to 800 MPa," *J. Phys. Chem. Ref. Data*, vol. 25, no. 6, p. 1509, Nov. 1996.

[19] G. M. Homsy, "Viscous Fingering in Porous Media," *Annu. Rev. Fluid Mech.*, vol. 19, no. 1, pp. 271–311, Jan. 1987.

[20] M. B. King, A. Mubarak, J. D. Kim, and T. R. Bott, "The mutual solubilities of water with supercritical and liquid carbon dioxides," *J. Supercrit. Fluids*, vol. 5, no. 4, pp. 296–302, Dec. 1992.

[21] W. D. Gunter, S. Bachu, and S. Benson, "The role of hydrogeological and geochemical trapping in sedimentary basins for secure geological storage of carbon dioxide," *Geol. Soc. London, Spec. Publ.*, vol. 233, no. 1, pp. 129–145, Jan. 2004.

[22] Y. Fujioka, K. Takeuchi, Y. Shindo, and H. Komiyama, "Shrinkage of liquid CO2 droplets in water," *Int. J. Energy Res.*, vol. 18, no. 8, pp. 765–769, Nov. 1994.

[23] Y. Shindo, Y. Fujioka, K. Takeuchi, and H. Komiyama, "Kinetics on the dissolution of CO2 into water from the surface of CO_2 hydrate at high pressure," *Int. J. Chem. Kinet.*, vol. 27, no. 6, pp. 569–575, Jun. 1995.

[24] A. T. Bozzo, C. Hsiao-Sheng, J. R. Kass, and A. J. Barduhn, "The properties of the hydrates of chlorine and carbon dioxide," *Desalination*, vol. 16, no. 3, pp. 303–320, Jun. 1975.

[25] M. J. Mitchell, O. E. Jensen, K. A. Cliffe, and M. M. Maroto-Valer, "A model of carbon dioxide dissolution and mineral carbonation kinetics," *Proc. R. Soc. A Math. Phys. Eng. Sci.*, vol. 466, no. 2117, pp. 1265–1290, Dec. 2009.

[26] C. Chalbaud, M. Robin, J.-M. Lombard, F. Martin, P. Egermann, and H. Bertin, "Interfacial tension measurements and wettability evaluation for geological CO_2 storage," *Adv. Water Resour.*, vol. 32, no. 1, pp. 98–109, Jan. 2009.

[27] S. Bachu and D. B. Bennion, "Interfacial Tension between CO_2 , Freshwater, and Brine in the Range of Pressure from (2 to 27) MPa, Temperature from (20 to 125) °C, and Water Salinity from (0 to 334 000) mg·L −1," *J. Chem. Eng. Data*, vol. 54, no. 3, pp. 765–775, Mar. 2009.

[28] R. T. Armstrong, M. L. Porter, and D. Wildenschild, "Linking pore-scale interfacial curvature to column-scale capillary pressure," *Adv. Water Resour.*, vol. 46, pp. 55–62, Sep. 2012.

[29] D. B. Bennion and S. Bachu, "Dependence on Temperature, Pressure, and Salinity of the IFT and Relative Permeability Displacement Characteristics of CO2 Injected in Deep Saline Aquifers," in *SPE Annual Technical Conference and Exhibition*, 2006.

[30] H. E. Huppert and J. A. Neufeld, "The Fluid Mechanics of Carbon Dioxide Sequestration," *Annu. Rev. Fluid Mech.*, vol. 46, no. 1, pp. 255–272, Jan. 2014.

[31] M. L. Porter, D. Wildenschild, G. Grant, and J. I. Gerhard, "Measurement and prediction of the relationship between capillary pressure, saturation, and interfacial area in a NAPL-water-glass bead system," *Water Resour. Res.*, vol. 46, no. 8, Aug. 2010.

[32] S. M. Hassanizadeh and W. G. Gray, "Thermodynamic basis of capillary pressure in porous media," *Water Resour. Res.*, vol. 29, no. 10, pp. 3389–3405, Oct. 1993.

[33] Y. Liu, D. D. Nolte, and L. J. Pyrak-Nolte, "Hysteresis and interfacial energies in smooth-walled microfluidic channels," *Water Resour. Res.*, vol. 47, no. 1, p. n/a–n/a, Jan. 2011.

[34] S. Bachu, W. D. Gunter, and E. H. Perkins, "Aquifer disposal of CO_2: Hydrodynamic and mineral trapping," *Energy Convers. Manag.*, vol. 35, no. 4, pp. 269–279, Apr. 1994.

[35] B. Metz, O. Davidson, H. C. De Coninck, M. Loos, and L. A. Meyer, "IPCC, 2005: IPCC special report on carbon dioxide capture and storage. Prepared by Working Group III of the Intergovernmental Panel on Climate Change," *Cambridge, United Kingdom New York, NY, USA, 442 pp*, 2005.

[36] S. Bachu, "CO_2 storage in geological media: Role, means, status and barriers to deployment," *Prog. Energy Combust. Sci.*, vol. 34, no. 2, pp. 254–273, Apr. 2008.

[37] R. Juanes, E. J. Spiteri, F. M. Orr, and M. J. Blunt, "Impact of relative permeability hysteresis on geological CO_2 storage," *Water Resour. Res.*, vol. 42, no. W12418, Dec. 2006.

[38] L. Zuo, C. Zhang, R. W. Falta, and S. M. Benson, "Micromodel investigations of CO_2 exsolution from carbonated water in sedimentary rocks," *Adv. Water Resour.*, vol. 53, no. null, pp. 188–197, Mar. 2013.

[39] J.-C. Perrin and S. Benson, "An Experimental Study on the Influence of Sub-Core Scale Heterogeneities on CO_2 Distribution in Reservoir Rocks," *Transp. Porous Media*, vol. 82, no. 1, pp. 93–109, Jun. 2010.

[40] L. Zuo, S. Krevor, R. W. Falta, and S. M. Benson, "An Experimental Study of CO_2 Exsolution and Relative Permeability Measurements During CO_2 Saturated Water Depressurization," *Transp. Porous Media*, vol. 91, no. 2, pp. 459–478, Sep. 2012.

[41] J. E. Garcia, "Density of aqueous solutions of CO_2," *Lawrence Berkeley Natl. Lab.*, Oct. 2001.

[42] H. Koide, M. Takahashi, H. Tsukamoto, and Y. Shindo, "Self-trapping mechanisms of carbon dioxide in the aquifer disposal," *Energy Convers. Manag.*, vol. 36, no. 6–9, pp. 505–508, Jun. 1995.

[43] T. Holt, J.-I. Jensen, and E. Lindeberg, "Underground storage of CO_2 in aquifers and oil reservoirs," *Energy Convers. Manag.*, vol. 36, no. 6–9, pp. 535–538, Jun. 1995.

[44] B. J. O. . McPherson and B. . Cole, "Multiphase CO_2 flow, transport and sequestration in the Powder River Basin, Wyoming, USA," *J. Geochemical Explor.*, vol. 69–70, pp. 65–69, Jun. 2000.

[45] J. Ennis-King, C. M. Gibson-Poole, S. C. Lang, and L. Paterson, "Long term numerical simulation of geological storage of CO_2 in the Petrel sub-basin, North West Australia," in *Greenhouse Gas Control Technologies, Proceedings of the 6th International Conference on Greenhouse Gas Control Technologies*, 2002, pp. 1–4.

[46] R. Lenormand, E. Touboul, and C. Zarcone, "Numerical models and experiments on immiscible displacements in porous media," *J. Fluid Mech.*, vol. 189, no. -1, p. 165, Apr. 1988.

[47] C. Zhang, M. Oostrom, T. W. Wietsma, J. W. Grate, and M. G. Warner, "Influence of Viscous and Capillary Forces on Immiscible Fluid Displacement: Pore-Scale Experimental Study in a Water-

Wet Micromodel Demonstrating Viscous and Capillary Fingering," *Energy & Fuels*, vol. 25, no. 8, pp. 3493–3505, Aug. 2011.

[48] F. Moebius and D. Or, "Interfacial jumps and pressure bursts during fluid displacement in interacting irregular capillaries.," *J. Colloid Interface Sci.*, vol. 377, no. 1, pp. 406–15, Jul. 2012.

[49] J. Bear, *Dynamics of Fluids in Porous Media*. New York, NY: American Elsevier Publishing Company, Inc, 1972.

[50] R. T. Armstrong and S. Berg, "Interfacial velocities and capillary pressure gradients during Haines jumps," *Phys. Rev. E*, vol. 88, no. 4, p. 043010, Oct. 2013.

[51] W. B. Haines, "Studies in the physical properties of soil. V. The hysteresis effect in capillary properties, and the modes of moisture distribution associated therewith," *J. Agric. Sci.*, vol. 20, no. 01, p. 97, Mar. 1930.

[52] G. Lorentzen, "Revival of carbon dioxide as a refrigerant," *Int. J. Refrig.*, vol. 17, no. 5, pp. 292–301, Jan. 1994.

[53] G. Lorentzen and J. Pettersen, "A new, efficient and environmentally benign system for car air-conditioning," *Int. J. Refrig.*, vol. 16, no. 1, pp. 4–12, Jan. 1993.

[54] D. M. Robinson and E. A. Groll, "Efficiencies of transcritical CO_2 cycles with and without an expansion turbine," *Int. J. Refrig.*, vol. 21, no. 7, pp. 577–589, Nov. 1998.

[55] S. M. Liao and T. S. Zhao, "Measurements of heat transfer coefficients from supercritical carbon dioxide flowing in horizontal mini/micro channels," *Trans. Soc. Mech. Eng. J. Heat Transf.*, vol. 124, no. 3, pp. 413–420, 2002.

[56] Y.-Y. Bae, H.-Y. Kim, and D.-J. Kang, "Forced and mixed convection heat transfer to supercritical CO_2 vertically flowing in a uniformly-heated circular tube," *Exp. Therm. Fluid Sci.*, vol. 34, no. 8, pp. 1295–1308, Nov. 2010.

[57] Y.-Y. Bae and H.-Y. Kim, "Convective heat transfer to CO_2 at a supercritical pressure flowing vertically upward in tubes and an annular channel," *Exp. Therm. Fluid Sci.*, vol. 33, no. 2, pp. 329–339, Jan. 2009.

[58] V. A. A. Kurganov and A. G. G. Kaptil'ny, "Velocity and enthalpy fields and eddy diffusivities in a heated supercritical fluid flow," *Exp. Therm. Fluid Sci.*, vol. 5, no. 4, pp. 465–478, Jul. 1992.

[59] B. Zappoli and A. Durand-Daubin, "Heat and mass transport in a near supercritical fluid," *Phys. Fluids*, vol. 6, no. 5, p. 1929, May 1994.

[60] N. Agrawal and S. Bhattacharyya, "Adiabatic capillary tube flow of carbon dioxide in a transcritical heat pump cycle," *Int. J. Energy Res.*, vol. 31, no. 11, pp. 1016–1030, Sep. 2007.

[61] S. Yamamoto, T. Furusawa, and R. Matsuzawa, "Numerical simulation of supercritical carbon dioxide flows across critical point," *Int. J. Heat Mass Transf.*, vol. 54, no. 4, pp. 774–782, Jan. 2011.

[62] J. Bellan, "Supercritical (and subcritical) fluid behavior and modeling: drops, streams, shear and mixing layers, jets and sprays," *Prog. Energy Combust. Sci.*, vol. 26, no. 4–6, pp. 329–366, Aug. 2000.

[63] J. Pettersen, "Two-Phase Flow Patterns in Microchannel Vaporization of CO_2 at Near-Critical Pressure," *Heat Transf. Eng.*, vol. 25, no. 3, pp. 52–60, 2004.

[64] R. Yun and Y. Kim, "Flow regimes for horizontal two-phase flow of CO_2 in a heated narrow rectangular channel," *Int. J. Multiph. Flow*, vol. 30, no. 10, pp. 1259–1270, Oct. 2004.

[65] C. Zhang, M. Oostrom, J. W. Grate, T. W. Wietsma, and M. G. Warner, "Liquid CO_2 displacement of water in a dual-permeability pore network micromodel.," *Environ. Sci. Technol.*, vol. 45, no. 17, pp. 7581–8, Sep. 2011.

[66] Y. Wang, C. Zhang, N. Wei, M. Oostrom, T. W. Wietsma, X. Li, and A. Bonneville, "Experimental study of crossover from capillary to viscous fingering for supercritical CO_2-water displacement in a homogeneous pore network.," *Environ. Sci. Technol.*, vol. 47, no. 1, pp. 212–8, Jan. 2013.

[67] D. Wildenschild, R. T. Armstrong, A. L. Herring, I. M. Young, and J. William Carey, "Exploring capillary trapping efficiency as a function of interfacial tension, viscosity, and flow rate," *Energy Procedia*, vol. 4, pp. 4945–4952, Jan. 2011.

[68] A. L. Herring, E. J. Harper, L. Andersson, A. Sheppard, B. K. Bay, and D. Wildenschild, "Effect of fluid topology on residual nonwetting phase trapping: Implications for geologic CO_2 sequestration," *Adv. Water Resour.*, vol. 62, pp. 47–58, Dec. 2013.

[69] R. Budwig, "Refractive index matching methods for liquid flow investigations," *Exp. Fluids*, vol. 17, no. 5, pp. 350–355, Sep. 1994.

[70] D. Wildenschild and A. P. Sheppard, "X-ray imaging and analysis techniques for quantifying pore-scale structure and processes in subsurface porous medium systems," *Adv. Water Resour.*, vol. 51, pp. 217–246, Jan. 2013.

[71] K. Brown, S. Schlüter, A. Sheppard, and D. Wildenschild, "On the challenges of measuring interfacial characteristics of three-phase fluid flow with x-ray microtomography.," *J. Microsc.*, vol. 253, no. 3, pp. 171–82, Mar. 2014.

[72] G. Ersland, J. Husebø, A. Graue, B. A. Baldwin, J. Howard, and J. Stevens, "Measuring gas hydrate formation and exchange with CO_2 in Bentheim sandstone using MRI tomography," *Chem. Eng. J.*, vol. 158, no. 1, pp. 25–31, Mar. 2010.

[73] Y. Song, N. Zhu, Y. Zhao, Y. Liu, L. Jiang, and T. Wang, "Magnetic resonance imaging study on near miscible supercritical CO_2 flooding in porous media," *Phys. Fluids*, vol. 25, no. 5, p. 053301, May 2013.

[74] S. M. Hassanizadeh, M. A. Celia, and H. K. Dahle, "Dynamic Effect in the Capillary Pressure–Saturation Relationship and its Impacts on Unsaturated Flow," *Vadose Zo. J.*, vol. 1, no. 1, pp. 38–57, Aug. 2002.

[75] S. Manthey, S. M. Hassanizadeh, R. Helmig, and R. Hilfer, "Dimensional analysis of two-phase flow including a rate-dependent capillary pressure–saturation relationship," *Adv. Water Resour.*, vol. 31, no. 9, pp. 1137–1150, Sep. 2008.

[76] D. M. O'Carroll, K. G. Mumford, L. M. Abriola, and J. I. Gerhard, "Influence of wettability variations on dynamic effects in capillary pressure," *Water Resour. Res.*, vol. 46, no. 8, Aug. 2010.

[77] D. M. O'Carroll, T. J. Phelan, and L. M. Abriola, "Exploring dynamic effects in capillary pressure in multistep outflow experiments," *Water Resour. Res.*, vol. 41, no. 11, Nov. 2005.

[78] A. Firoozabadi, B. Ottesen, and M. Mikklesen, "Measurements of Supersaturation and Critical Gas Saturation (includes associated papers 27920 and 28669)," *SPE Form. Eval.*, vol. 7, no. 04, pp. 337–344, Apr. 2013.

[79] X. Li and Y. C. Yortsos, "Theory of multiple bubble growth in porous media by solute diffusion," *Chem. Eng. Sci.*, vol. 50, no. 8, pp. 1247–1271, Apr. 1995.

[80] B. B. Maini, H. K. Sarma, and A. E. George, "Significance of Foamy-oil Behaviour In Primary Production of Heavy Oils," *J. Can. Pet. Technol.*, vol. 32, no. 09, Apr. 2013.

[81] C. Chomsurin, "Analysis of pore-scale nonaqueous phase liquid dissolution in etched silicon pore network," University of Illinois at Urbana-Champaign, 2003.

[82] W. Kern, "Hydrogen peroxide solutions for silicon wafer cleaning," *RCA Eng*, vol. 28, pp. 99–105, 1983.

[83] R. J. Adrian and J. Westerweel, *Particle image velocimetry*, no. 30. Cambridge University Press, 2011.

[84] J. G. Santiago, S. T. Wereley, C. D. Meinhart, D. J. Beebe, and R. J. Adrian, "A particle image velocimetry system for microfluidics," *Exp. Fluids*, vol. 25, no. 4, pp. 316–319, Sep. 1998.

[85] C. D. Meinhart, S. T. Wereley, and J. G. Santiago, "PIV measurements of a microchannel flow," *Exp. Fluids*, vol. 27, no. 5, pp. 414–419, Oct. 1999.

[86] C. D. Meinhart, S. T. Wereley, and M. H. B. Gray, "Volume illumination for two-dimensional particle image velocimetry," *Meas. Sci. Technol.*, vol. 11, no. 6, pp. 809–814, Jun. 2000.

[87] A. K. Prasad, R. J. Adrian, C. C. Landreth, and P. W. Offutt, "Effect of resolution on the speed and accuracy of particle image velocimetry interrogation," *Exp. Fluids*, vol. 13, no. 2–3, pp. 105–116, Jun. 1992.

[88] K. T. Christensen, "The influence of peak-locking errors on turbulence statistics computed from PIV ensembles," *Exp. Fluids*, vol. 36, no. 3, pp. 484–497, Mar. 2004.

[89] F. Rindfleisch, T. P. DiNoia, and M. A. McHugh, "Solubility of Polymers and Copolymers in Supercritical CO_2," *J. Phys. Chem.*, vol. 100, no. 38, pp. 15581–15587, Jan. 1996.

[90] R. J. Goldstein and T. H. Kuehn, "Optical systems for flow measurement: Shadowgraph, schlieren, and interferometric techniques," *Fluid Mech. Meas. Taylor Fr.*, pp. 451–508, 1996.

[91] C. M. Oldenburg, "Joule-Thomson cooling due to CO2 injection into natural gas reservoirs," *Energy Convers. Manag.*, vol. 48, no. 6, pp. 1808–1815, Jun. 2007.

[92] R. Bender, K. Bier, and G. Manrer, "Messung der spezifischen Wärme und des Joule-Thomson-Koeffizienten von Kohlendioxid bei Temperaturen von - 40°C bis 200°C und Drücken bis 15 bar," *Berichte der Bunsengesellschaft für Phys. Chemie*, vol. 85, no. 8, pp. 778–784, Aug. 1981.

[93] E. Burnett, "Experimental Study of the Joule-Thomson Effect in Carbon Dioxide," *Phys. Rev.*, vol. 22, no. 6, pp. 590–616, Dec. 1923.

[94] J. R. Roebuck, T. A. Murrell, and E. E. Miller, "The Joule-Thomson Effect in Carbon Dioxide," *J. Am. Chem. Soc.*, vol. 64, no. 2, pp. 400–411, Feb. 1942.

[95] L. Cuscó, S. E. McBain, and G. Saville, "A flow calorimeter for the measurement of the isothermal Joule-Thomson coefficient of gases at elevated temperatures and pressures. Results for nitrogen at temperatures up to 473 K and pressures up to 10 MPa and for carbon dioxide at temperatures up to 50," *J. Chem. Thermodyn.*, vol. 27, no. 7, pp. 721–733, Jul. 1995.

[96] A. Michels and J. Hamers, "The effect of pressure on the refractive index of CO_2," *Physica*, vol. 4, no. 10, pp. 995–1006, Oct. 1937.

[97] J. M. H. L. Sengers, "Coexistence Curves of CO_2, N_2O, and $CClF_3$ in the Critical Region," *J. Chem. Phys.*, vol. 54, no. 12, p. 5034, Jun. 1971.

[98] G. Blois, J. M. Barros, and K. T. Christensen, "A Microscopic Particle Image Velocimetry Method for Studying the Dynamics of Immiscible Liquid–Liquid Interactions in a Porous Micromodel," *Microfluid. Nanofluidics*, vol. Submitted, 2014.

[99] S. S. Datta, T. S. Ramakrishnan, and D. A. Weitz, "Mobilization of a trapped non-wetting fluid from a three-dimensional porous medium," *Phys. Fluids*, vol. 26, no. 2, p. 022002, Feb. 2014.

[100] G. Taubin, "Estimation of planar curves, surfaces, and nonplanar space curves defined by implicit equations with applications to edge and range image segmentation," *IEEE Trans. Pattern Anal. Mach. Intell.*, vol. 13, no. 11, pp. 1115–1138, 1991.

[101] D. Wilkinson and J. F. Willemsen, "Invasion percolation: a new form of percolation theory," *J. Phys. A. Math. Gen.*, vol. 16, no. 14, pp. 3365–3376, Oct. 1983.

[102] P. Meakin and A. M. Tartakovsky, "Modeling and simulation of pore-scale multiphase fluid flow and reactive transport in fractured and porous media," *Rev. Geophys.*, vol. 47, no. 3, p. RG3002, Jul. 2009.

[103] S. Mukhopadhyay, J. T. Birkholzer, J.-P. Nicot, and S. A. Hosseini, "A model comparison initiative for a CO_2 injection field test: an introduction to Sim-SEQ," *Environ. Earth Sci.*, vol. 67, no. 2, pp. 601–611, Apr. 2012.

[104] S. Mukhopadhyay, C. Doughty, D. Bacon, J. Li, L. Wei, H. Yamamoto, S. Gasda, S. A. Hosseini, J.-P. Nicot, and J. T. Birkholzer, "The Sim-SEQ Project: Comparison of Selected Flow Models for the S-3 Site," *Transp. Porous Media*, Jul. 2014.

[105] S. M. Frailey, T. M. Parris, J. R. Damico, R. T. Okwen, and R. W. McKaskle, "CO_2 Storage and Enhanced Oil Recovery: Sugar Creek Oil Field Test Site, Hopkins County, Kentucky (OFS2012-4)," 2012.

[106] "Enhanced Oil Recovery I: Loudon Single-Well Huff 'n' Puff," 2009.